ANALYSIS OF THE CONCENTRIC PLANETARY MAGNETIC GEAR

A Dissertation

by

NICOLAS WALTER FRANK

Submitted to the Office of Graduate Studies of
Texas A&M University
in partial fulfillment of the requirements for the degree of

DOCTOR OF PHILOSOPHY

May 2011

Major Subject: Electrical Engineering

ANALYSIS OF THE CONCENTRIC PLANETARY MAGNETIC GEAR

A Dissertation

by

NICOLAS WALTER FRANK

Submitted to the Office of Graduate Studies of
Texas A&M University
in partial fulfillment of the requirements for the degree of

DOCTOR OF PHILOSOPHY

Approved by:

Chair of Committee,	Hamid A. Toliyat
Committee Members,	Mehrdad Ehsani
	Jun Zou
	Won-jong Kim
Head of Department,	Costas N. Georghiades

May 2011

Major Subject: Electrical Engineering

ABSTRACT

Analysis of the Concentric Planetary Magnetic Gear. (May 2011)

Nicolas Walter Frank, B.S., Texas A&M University

Chair of Advisory Committee: Dr. Hamid A. Toliyat

In the field of electric machine design, a trend in many applications has been to design machines with increasing torque density. When machines fail to meet torque density requirements or are simply incapable of matching load torque, gears are commonly used. Magnetic gears have been proposed as a means of increasing torque density within electromechanical systems, while avoiding problems associated with traditional mechanical gears. While the idea behind magnetic gears goes back to early patents, their study and use in industry has been very limited to date.

This study looks into variations of the gear which could lead to more industrial use. The effect of pole count upon torque ripple is investigated with finite element analysis (FEA). The analysis is extended to new magnetic layouts which borrow from permanent magnet machine design. One of the most critical components of the gear, the stator pole pieces, are also investigated for variations which aid in construction while maintaining the performance of the gear.

As a means of supplementing analysis of the gear, winding function theory (WFT) is used to analyze the gear. Winding function theory has enjoyed success with induction, synchronous, and even switched reluctance machines in the past. This study is the first

of its kind to apply winding function theory to a device devoid of windings altogether. It is shown that this method is capable of generating the stall torque and steady-state torque ripple waveforms which have been commonly attempted with FEA.

While magnetic gears enjoy distinct advantages over mechanical gears such as inherent overload protection, they are not as torsionally stiff as their mechanical counterparts. As such, the use of damper windings for the purpose of stiffening the gear against transient oscillations is also investigated. Several competing designs are investigated for their performance, and a final design is studied which is capable of arresting transient oscillations in less than a second.

In addition, a prototype has been fabricated and will be used to verify the analysis undertaken. The prototype is used to verify variations of the stator pole pieces as well as the inner rotor magnetic layout. A dynamometer has been assembled to test the performance of the prototype. A new design is also proposed for future work.

DEDICATION

To my parents, whose love and support has allowed me to pursue my education, this dissertation is dedicated to you.

ACKNOWLEDGMENTS

I would like to thank my advisor, Dr. Hamid Toliyat. His enthusiasm for power electronics convinced me to pursue my doctorate, and his guidance over my graduate career has helped me to complete this dissertation and find applications around the world. I would also like to thank Dr. Peter Rasmussen of Aalborg University for introducing me to magnetic gears. His generous invitation to study with him in Aalborg, as well as the help with the prototype was crucial to this study.

I thank the machinists at Aalborg University who cut the laminations and helped me disassemble the initial prototype. I would also like to thank the machinists here in Bryan who helped me fabricate the components for the final prototype and assemble it. I thank Vestas Wind Systems for their support at the beginning of this project, which helped support me in Denmark and fund the final prototype as well as equipment for the dynamometer. I would also like to thank the American Scandinavian Foundation for their generous grant which also helped fund my time in Denmark. Finally, I would like to thank my friend, Dr. Marvin Onabajo, whose help was greatly appreciated in assembling this manuscript.

TABLE OF CONTENTS

Page

ABSTRACT iii

DEDICATION v

ACKNOWLEDGMENTS vi

TABLE OF CONTENTS vii

LIST OF FIGURES x

LIST OF TABLES xvi

I. INTRODUCTION 1

I.1. History of Magnetic Gears 2
I.2. Elements of Comparison from Mechanical Gears 4
I.2.1. Spur gears 4
I.2.2. Planetary gears 5
I.3. Tools of Analysis 7
I.4. Winding Function Theory and Damper Windings for the Magnetic Gear 8
I.5. The Prototype 10

II. MAGNETIC GEARS 11

II.1. Applications 11
II.1.1. Wind turbines 11
II.1.2. Marine propulsion 15
II.1.3. Hybrid electric vehicles 16
II.2. The Concentric Planetary Magnetic Gear 25
II.2.1. Equilibrium and gear ratio 26
II.2.2. Effect of gear ratio upon torque ripple 30
II.2.3. Parameters for design 37
II.3. Conclusion 40

III. ANALYSIS OF THE MAGNETIC GEAR WITH WINDING FUNCTION THEORY 42

III.1. Winding Function Theory and its Modifications 44
III.1.1. Basic winding function theory 44
III.1.2. Winding function theory for machines with salient air gaps 48
III.2. Winding Function Theory Applied to Magnetic Devices 51

Page

III.2.1. Verification of a single phase per rotor 54
III.2.2. Applying modified winding function theory to ideal machines ... 56
III.2.3. Winding function theory applied to the magnetic coupling 60
III.2.4. Winding function theory applied to the concentric planetary magnetic gear 62
III.2.5. Torque calculated from inductance 67
III.3. Conclusion 71

IV. DAMPER WINDINGS FOR THE MAGNETIC GEAR 72

IV.1. The History of Damper Windings 72
IV.2. Design and Placement of the Damper Windings 73
IV.3. Testing the Effectiveness of the Designs 74
IV.3.1. The value of the spring constant 74
IV.3.2. Parameters for the damper windings 77
IV.3.3. Transient performance with respect to number of bars 78
IV.3.4. Transient performance with respect to interrupted and uninterrupted cage 81
IV.3.5. Transient performance with respect to bar radius 81
IV.3.6. Transient performance with respect to end ring resistance 82
IV.3.7. Transient performance with respect to end ring inductance 83
IV.4. A Final Design 84
IV.4.1. Final design parameters 84
IV.4.2. Performance of the final design 86
IV.5. Conclusion 88

V. THE PROTOTYPE 89

V.1. Background and Motivation 89
V.2. Design 90
V.3. Analysis of the New Construction with Modified Winding Function Theory 94
V.3.1. Effect of the IPM geometry upon inductance 95
V.3.2. Effect of the stator bridges upon inductance 100
V.3.3. Torque output using MWFT 103
V.4. Construction 104
V.4.1. Assembly problems for the inner rotor 105
V.4.2. Assembly problems for the stator stack 106
V.5. Results 109
V.6. An Improved Design 111
V.7. Conclusion 113

VI. SUMMARY AND CONCLUSIONS 114

Page

VI.1. The Appeal of Magnetic Gears 114
VI.2. Future Work 114
VI.3. Conclusion 117

REFERENCES 118

APPENDIX A 127

VITA 129

LIST OF FIGURES

Page

Fig. 1. Spur gear with (a) equal radii and (b) with parameter circles. 5

Fig. 2. Planetary gear with parameters. 6

Fig. 3. Maxwell (a) solid model in design editor and (b) solution mesh. 8

Fig. 4. MagNet (a) solid model in design editor and (b) solution mesh. 8

Fig. 5. The transmotor. 17

Fig. 6. HEV drive train with transmotor. 19

Fig. 7. Integrated magnetic gear/PM machine for traction shown (a) inside wheel and (b) in an assembly of fundamental elements. 21

Fig. 8. Series HEV drive train with integrated magnetic gear/PM machine traction units. 22

Fig. 9. HEV drive train with transmotor. 22

Fig. 10. Integrated speed- and torque-coupling drive train with transmotor and integrated magnetic gear/PM machine. 23

Fig. 11. Magnetic gear with 31 outer and 5 inner pole pairs. 25

Fig. 12. The modulation of the radial flux density due to the pole pieces in a gear with 4 inner and 22 outer pole pairs. 26

Fig. 13. Assembly showing (a) outer magnetic ring fixed, (b) stator segments fixed, and (c) inner magnetic ring fixed. 27

Fig. 14. Torque curves revealing equilibrium points for the 22/4 magnetic gear. 29

Fig. 15. Torque transfer showing ripple with change in speed. 32

Fig. 16. Percentage torque ripple for high-speed and low-speed rotors for whole gear ratios. 33

Fig. 17. Percentage torque ripple for high-speed and low-speed rotors for half and third gear ratios. 33

Page

Fig. 18. Percentage torque ripple for high-speed and low-speed rotors for remaining fractional gear ratios. 34

Fig. 19. Torque transfer in 28/4 gear for (a) fixed stator and (b) fixed outer rotor operation. 36

Fig. 20. Flux plot showing leakage flux paths (circled in blue) between adjacent magnets of inner rotor. 37

Fig. 21. 31/4 magnetic gear using (a) saliency for flux barriers and (b) integrated flux barriers. 39

Fig. 22. 31/4 magnetic gear using (a) saliency for flux barriers and (b) integrated flux barriers. 40

Fig. 23. An idealized construction of the concentric planetary magnetic gear used to develop winding function theory for the gear. 43

Fig. 24. An idealized machine with conductors in the air gap. 44

Fig. 25. An idealized machine with multiple coils in the air gap. 47

Fig. 26. An idealized machine with a salient rotor and conductors in the air gap. 49

Fig. 27. Model of a permanent magnet with coils fed by DC current which produces an equivalent magnetization vector. 52

Fig. 28. Permanent magnets with alternating vectors form the basis for a single turns function over the circumference of the rotor. 53

Fig. 29. An 8-pole rotor with infinitesimally narrow coil sides and its resulting turns function. 53

Fig. 30. The turns function modeled with the Fourier Series. 54

Fig. 31. An ideal four pole machine. 54

Fig. 32. Turns and winding functions for stator phases. 55

Fig. 33. Idealized machines built in MagNet showing combinations among 2 and 4 pole stator windings and 2 and 4 pole synchronous rotors, (a) machine 1, (b) machine 2, (c) machine 3, and (d) machine 4. 57

Fig. 34. Inductances calculated with FEA for (a) machine 1, (b) machine 2, (c) machine 3, and (d) machine 4. 58

Page

Fig. 35. Flowchart for calculated inductances using MWFT in Matlab/Simulink....59

Fig. 36. Inverse gap function used for ideal machines in inductance calculations. 59

Fig. 37. Inductances calculated with MWFT for (a) machine 1, (b) machine 2, (c) machine 3, and (d) machine 4....60

Fig. 38. 8-pole radial magnetic coupling with (a) permanent magnets and (b) coils. 61

Fig. 39. Mutual inductance of inner rotor calculated with FEA and MWFT. 62

Fig. 40. Linear sections of magnetizing inductance calculations for (a) inner rotor and (b) outer rotor. 63

Fig. 41. Magnetizing inductances calculated with FEA for (a) inner rotor and (b) outer rotor. 64

Fig. 42. Magnetizing inductances calculated with MWFT for (a) inner rotor and (b) outer rotor. 64

Fig. 43. Difference in flux paths with MWFT and FEA. 65

Fig. 44. Inverse gap function used for mutual inductance calculations. 66

Fig. 45. Mutual inductances calculated by MWFT and FEA for (a) the inner rotor and (b) the outer rotor. 66

Fig. 46. Validity of replacing magnets with coils shown over a pole pair pitch showing torque curves for the (a) outer rotor and (b) inner rotor. 68

Fig. 47. Changing reluctance as magnets move over pole pieces. 68

Fig. 48. Torque of inner rotor of magnetic coupling calculated with FEA and MWFT....70

Fig. 49. Torques calculated with MWFT for (a) inner rotor cogging torque, (b) outer rotor cogging torque, (c) inner rotor stall torque, and (d) outer rotor stall torque. 71

Fig. 50. Base designs with damper windings included for (a) salient pole design, (b) spoke design, (c) IPM design with damper bars in the flux barriers, and (d) IPM design with damper bars behind the magnets. 74

Page

Fig. 51. Value of spring constant K shown linearized about the origin for the salient pole design. 75

Fig. 52. Comparison of settling times between (a) salient pole design and (b) salient pole design with damper windings. 77

Fig. 53. Bar arrangement for 4 bars in one pole of the magnetic gear. 80

Fig. 54. Flux linkage in the salient pole design with 4 bars per pole as it settles to equilibrium. 80

Fig. 55. Effect of damper bar radius on settling time. 82

Fig. 56. Effect of end ring resistance on settling time. 83

Fig. 57. Effect of end ring inductance on settling time. 84

Fig. 58. Final design for the concentric planetary magnetic gear with damper windings. 85

Fig. 59. Stall torque rating of the outer rotor as the inner rotor magnets are shifted towards the shaft. 86

Fig. 60. Transient performance of the final design. 87

Fig. 61. Current in a damper bar at steady state. 87

Fig. 62. New variations of the stator with arrows pointing to bridges connecting the stator pieces on the (a) interior, (b) exterior, and (c) both sides. 91

Fig. 63. Prototype (a) FEA model and (b) FEA-calculated torque angle curve. 92

Fig. 64. Stall torque raring with respect to bridge thickness for (a) inner connection and (b) outer connection. 94

Fig. 65. Torques calculated using coils and permanent magnets with FEA for (a) outer rotor and (b) inner rotor. 95

Fig. 66. Magnetizing inductances calculated with FEA for (a) inner rotor, and (b) outer rotor. 96

Fig. 67. Mutual inductances calculated with FEA for (a) inner rotor and (b) outer rotor. 96

Fig. 68. Additional flux leakage paths shown circled in the calculation of L_{io}. 97

Page

Fig. 69. Turns function for inner rotor. 98

Fig. 70. Magnetizing inductances calculated with MWFT for (a) inner rotor and (b) outer rotor. 99

Fig. 71. Mutual inductances calculated with MWFT for (a) inner rotor and (b) outer rotor....99

Fig. 72. Flux aided by the addition of stator bridges shown circled. 101

Fig. 73. Magnetizing inductances for stator segments connected with bridges calculated with FEA for (a) inner rotor and (b) outer rotor. 102

Fig. 74. Mutual inductances for stator segments connected with bridges calculated with FEA for (a) inner rotor and (b) outer rotor. 102

Fig. 75. Torques calculated with MWFT accounting for IPM geometry for (a) inner rotor cogging torque, (b) outer rotor cogging torque, (c) inner rotor stall torque, and (d) outer rotor stall torque....103

Fig. 76. Steady state torque ripple calculated with FEA for the (a) inner rotor and (b) outer rotor. 104

Fig. 77. New inner rotor and stator redesign with (a) laminations shown and (b) assembled with magnets. 105

Fig. 78. Assembly of stator with (a) sectioned view of mold and (b) stack with aluminum rods to adhere stack to base. 105

Fig. 79. Assembly of the inner rotor (a) before magnets shown in front of outer rotor assembly and (b) during placement of magnet pairs....106

Fig. 80. Second (left) and third (right) iteration of the stator stack....107

Fig. 81. Magnets on the outer rotor with lost coatings due to contact with stator stack. 108

Fig. 82. Verification of stator stack concentricity by using the lathe....108

Fig. 83. Dynamometer for testing the magnetic gear prototype....109

Fig. 84. Steady-state torque ripple of the gearbox under no load. 110

Fig. 85. Torque waveforms of both rotors when inner rotor experiences a stall. ...111

Fig. 86. Replacement of bearings from (a) angular contact to (b) tapered roller. ...112

Page

Fig. 87. New prototype with rotors supported from both sides.....112

Fig. 88. 3D model of the magnetic gear simulated in MagNet's 3D static solver showing solutions for the (a) shaded flux density field and the (b) vector field of flux density. 116

LIST OF TABLES

Page

Table I. Gear ratios for chosen pole pair ratio models 30

Table II. Dimensions for models in preliminary gearing ratio analysis 31

Table III. Torque ripple results between operating modes 34

Table IV. Comparison of performance for 31/4 models 39

Table V. Parameters for ideal machine simulations 57

Table VI. Parameters for 8-pole coupling 61

Table VII. Parameters common to all designs 73

Table VIII. Settling times for base designs and base designs with damper windings 76

Table IX. Cost for magnetic gear prototype 90

Table X. Magnetic gear dimensions 90

Table XI. Stall torque rating for different FEA packages and variations of the stator 93

I. INTRODUCTION*

Electromechanical systems in many industrial areas strive for greater torque density to reduce volume and weight. One of the traditional ways of increasing torque density with regards to an electric motor is to couple it to a gear. Few institutions however have done work in the area of magnetic gears in order to bring the technology to maturity.

A study of the concentric planetary gear will be taken which looks at strengthening the stator pole pieces. This is of key importance towards industrial use, since the stator pole pieces must withstand the sum of the torques for both magnetic rotors. In addition, the use of an interior permanent magnetic configuration is studied and built in a prototype. Finite element analysis is used to study the effect of stall torque rating between the different configurations.

Winding function theory, which has been used to study induction and synchronous machines, will be applied to the magnetic gear. Thus far, analysis of magnetic gears has been restricted to two main methods for torque calculation: Finite Element Analysis (FEA) which most commonly uses either the coenergy or Maxwell stress tensor methods, and numerical analysis using the Maxwell stress tensor method with Fourier

---

This dissertation follows the style and format of the *IEEE Transactions on Magnetics*.

series for the magnetic fields. While both methods are rigorous and yield good results for 2D simulations, they can be lengthy to setup and run. The winding function method allows quicker setup and analysis of gear variations than with FEA, and it can also yield stall torque as well as cogging torque waveforms. The analysis is the first of its kind to apply a theory which has historically been applied to electric machines with windings, and rarely with electric machines containing magnets, to a device devoid of windings altogether.

In addition, the application of damper windings to the magnetic gear will also be investigated. Magnetic gears offer the distinct advantage of overload protection, at the cost of torsional stiffness with respect to mechanical gears. Designs with damper windings will be evaluated for their effectiveness in suppressing transient oscillations due to changes in speed and load. It is believed that this is the first means of passively suppressing oscillations, whereas other means have been active.

I.1. History of Magnetic Gears

The idea behind a gear using permanent magnets dates back as early as the 1940's with a US patent by Faus [1]. A handful of patents over the years have followed, most of them occurring within the past few decades. A summary of patents related to magnetic gearing can be found in Appendix A. Early magnetic gears using ferrite magnets and spur gear configurations yielded poor torque densities. With the advent of rare-earth permanent magnets, more work has been done at achieving greater torque density out of magnetic gears. Early work was done by Tsurumoto [2] with non-concentric magnetic

gears using Samarium Cobalt magnets. More research and prototypes followed with the concentric planetary magnetic gear in [3],[4], and [5].

Since then, more work has been done on new designs which yield greater gearing ratios or control. In [6], windings were placed on the outside of the concentric planetary magnetic gear to help dampen the gearbox against transient responses. In [7], the concentric planetary gear was proposed for use with counter-rotating tidal turbines, and a prototype was built. In [8], the concentric planetary magnetic gear was redesigned with Halbach arrays for the magnetic rotors in comparison to parallel-magnetized magnets. The results showed a higher stall torque rating, as well as lower torque ripple and iron losses. In [9], a concentric planetary magnetic gear was built which used an axial flux configuration for the stator pole pieces, instead of a radial flux configuration.

Other designs have also begun to appear to achieve higher torque density ratings. In [10], a planetary gearing arrangement using a sun gear and planet gears was simulated and fabricated, which yielded a torque density close to 100 kNm/m^3. In [11], a cycloid magnetic gear was analyzed and fabricated. The cycloid gear utilizes a cycloid action to modulate the air gap between the two magnetic rings, thus achieving a high gear ratio and torque density, at the cost of a very complex bearing layout. In [12] the harmonic magnetic gear was studied and built. In this design, instead of using a cycloid action to modulate the air gap between the magnetic rings, a flexible rotor was proposed, in which the inner rotor would change shape and thus the air gap.

I.2. Elements of Comparison from Mechanical Gears

Mechanical gears are found in the writings of Aristotle as early as 330 B.C., and even a chariot used by China's Yellow Emperor for navigation over 4500 years ago. The earliest gears were made of wood, and crafted individually by hand without much regard to mechanical engineering theory. Around 1500, Juanelo Torriano of Spain fashioned the first known gear cutting machine. Greater interest in the engineering theory behind gears followed. Around 1800, metal gears moved from the arena of clocks to larger power drives [13].

If magnetic gears are intended to replace mechanical gears in numerous applications, then parameters must be studied for means of comparison. In general, the layout of magnetic gears borrows directly from layouts intended for mechanical gears.

I.2.1. Spur gears

The first and most basic type of gear is the spur gear, shown in Fig. 1. The two gears transmit motion between parallel rotation shafts, and in the most basic type of spur gear, the teeth are parallel to the axis of rotation. The pitch, p, is defined as the arc length between equivalent points on adjacent teeth. The pitch has a dual in magnetic terms with regards to pole pitch between adjacent magnets. The pitch circles of the two mating gears are tangent to each other and their respective diameters are given by d. Using these parameters, the number of teeth, N, is given by (1).

$$N = \frac{\pi d}{p} \tag{1}$$

The ratio of the velocities of the two gears is given in (2) with respect to their radii.

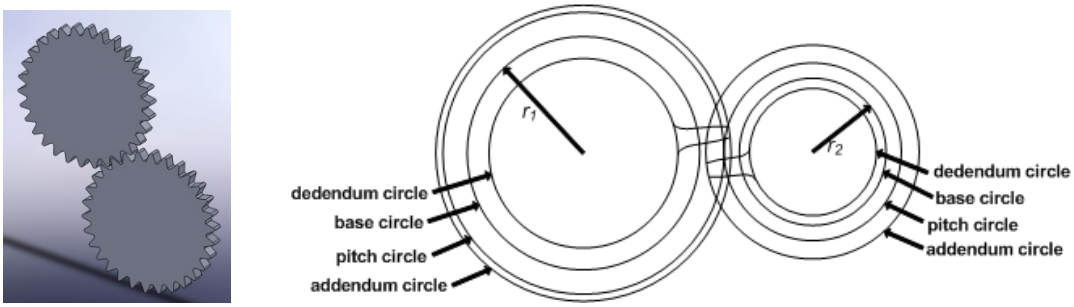

(a) (b)

Fig. 1. Spur gear with (a) equal radii and (b) with parameter circles.

$$\frac{\omega_1}{\omega_2} = \frac{r_2}{r_1} \tag{2}$$

The additional circles in Fig. 1b outline parameters of the teeth in the gears. The addendum circle outlines the top land, or outermost portion of the teeth, while the dedendum circle outlines the bottom land, or lowermost portion of the teeth. Spur gears, and gears in general, use the involute profile to form the teeth. The involute which forms the teeth is formed on the base circles of the respective gears [14].

I.2.2. Planetary gears

A newer and very popular type of gearing arrangement is the planetary arrangement shown in Fig. 2. The multiple gears are arranged around the central sun gear. Around the sun gear are planet gears which rotate about the central axis, as well as their individual axes. The planet gears are connected via a common carrier which can rotate about the central axis. Surrounding all of these is the ring gear.

The gear ratio is found by applying Willis' equation to the gear. In 1841, Willis showed that the motion could be explained by a superposition of partial motions. Using the ratio of the speed of the ring and sun gears relative to the carrier:

$$k = \frac{\omega_r}{\omega_s}, \tag{3}$$

Willis' equation is shown in (4)[15]. Assuming that the carrier is fixed (i.e. ω_c=0), the gear ratio between the ring gear and the sun gear is given in (5) with respect to the number of teeth, *N*, in the respective gears [16].

$$\omega_r - k\omega_s - \omega_c(1-k) = 0 \tag{4}$$

$$\frac{\omega_r}{\omega_s} = -\frac{N_s}{N_r} \tag{5}$$

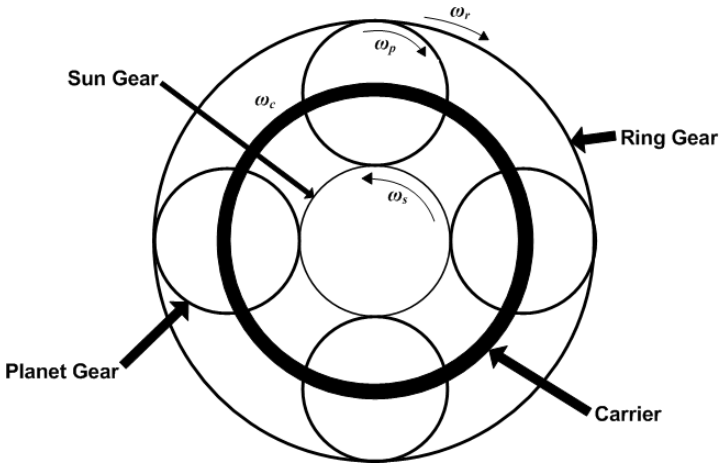

Fig. 2. Planetary gear with parameters.

Planetary gears have grown in popularity due to their high torque density compared to the spur gear arrangement. In the wind turbine industry, one of the most common gear arrangements is to have two planetary stages followed by a final spur gear stage. The first two planetary stages are used due to the extremely high torque output of the blade hub. The final spur gear stage is rated for the lowest torque, and to help achieve an end-to-end gear ratio of 100:1. Throughout this dissertation, one of the driving factors for

improvement of the gear is to increase torque density. With an increase in torque density, the gear becomes more attractive for industrial use.

I.3. Tools of Analysis

Finite element analysis (FEA) has been used to simulate the behavior of the different magnetic gear variations. Maxwell by Ansoft, as well as MagNet by Infolytica are both used here. The methods for calculating torque are different in both packages as well. Maxwell uses the virtual work method of calculating torque for the moving bodies in its transient simulations. MagNet uses the Maxwell stress tensor method of calculating torque on a body in its transient simulations. Fig. 3 shows a screenshot of a model built in Maxwell, with the corresponding solution mesh, regenerated at each time instant. Fig. 4 shows a screenshot of a model built in MagNet, with the corresponding solution mesh, only parts of which are regenerated at each time instant.

The strengths of each FEA package led to their use in certain areas of analysis throughout this research. In particular, MagNet's ability to calculate flux linkage in the 2D transient solver was a powerful tool for verification of the inductances calculated with winding function theory. Maxwell's ability to quickly modify existing designs and solve for torque quickly was a powerful tool for verification of designs used for the prototype, as well as verifying designs for use with damper windings.

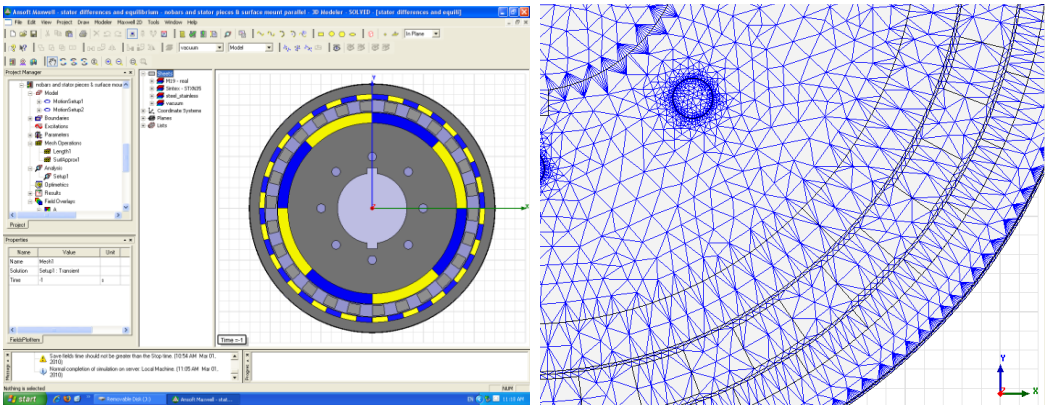

(a) (b)

Fig. 3. Maxwell (a) solid model in design editor and (b) solution mesh.

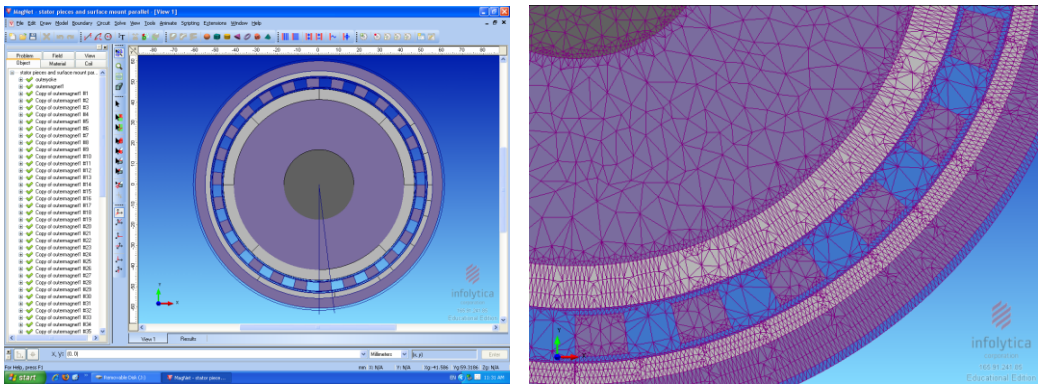

(a) (b)

Fig. 4. MagNet (a) solid model in design editor and (b) solution mesh.

I.4. Winding Function Theory and Damper Windings for the Magnetic Gear

Winding function theory has been used for years on induction and synchronous machines [17][18]. Little has been done however to apply winding function theory to machines with permanent magnets, just two examples of which are found in [19] and [20]. Its usefulness lies in the fact that it can take into account geometrical variations of the machines and be used to simulate transient performance. It can be used to run

simulations in a quicker manner than FEA. Using this, parametric studies for different variations of the gear could be undertaken much quicker than running multiple FEA simulations.

The basis for applying winding function theory to magnetic gears is to treat the magnets as coils. A permanent magnet which is magnetized in a parallel manner can be modeled as a coil wrapped around material with the same permeability as that of the magnet. The coils, with sufficient current, can provide the same magnetomotive force (MMF) as the magnet itself. The magnets on each rotor can then be considered as coils connected in series, giving the magnetic gears two series connected sets of coils, or phases, the inner rotor and the outer rotor. The MMF imposed by the magnetic layout, along with the gap function imposed by the stator pole pieces will be used to calculate the inductance variation as the gear moves. The changing inductance will then be used to calculate the torque of the two rotors.

Compared to mechanical gears, magnetic gears enjoy the advantage of having inherent overload capability. However, their torsional stiffness is much lower than mechanical gears, resulting in oscillations during transient changes in speed and load. Damper windings have been used in synchronous generators to suppress oscillations due to transients, and they are applied to the magnetic gear for the same purpose. A study will be undertaken to determine effective designs which incorporate damper windings within the concentric planetary magnetic gear. The study will also determine the effect of different parameters for the damper cage in each design. It is believed that this is the

first attempt to add a passive means of oscillation damping to the magnetic gear, whereas all other previous means have been active.

I.5. The Prototype

The analysis undertaken is supported by the fabrication of a prototype. The original prototype, begun in [5], was borrowed from the Institute of Energy Technology at Aalborg University in Denmark. The stator and rotor have been reconstructed to verify the new variations. Problems associated with their construction are discussed to help with prototypes in the future, and a layout for an improved prototype is given.

A dynamometer has been setup with torque transducers to monitor the torque waveform of both rotors of the gear. The outer rotor is driven by an induction servomotor and the inner rotor is loaded with a hysteresis brake. Results will be shown which are in agreement with the stall torque rating found with other prototypes.

II. MAGNETIC GEARS *

II.1. Applications

The applications for magnetic gears are as numerous as the applications for traditional mechanical gears. In the case of the gear studied here, it can be suited to three very large industries: wind turbines, ship propulsion, and vehicle traction.

II.1.1. Wind turbines

Sustainable energy accounted for 23% (31 GW) of added power generation capacity worldwide in 2007. The majority of new investments into sustainable energy were dominated by wind, totaling 43% [21]. In 2008, wind energy totaled 45% of all investments worldwide for sustainable energy. As of 2009, wind had climbed to 56% of all financial investments worldwide for sustainable energy [22]. There is a need for improvement in turbine design to not only increase the standard generation capacity of a single turbine, but also reduce maintenance needs for the plethora of turbines located on wind farms throughout the world.

Of primary importance is the migration from purely mechanical components to electromechanical ones. The majority of turbines incorporate a mechanical gearbox in line with the generator to take the high-torque, low-speed output from the hub and

transfer it into a high-speed, low-torque input to the generator. A small but growing segment of the wind turbine industry has resorted to directly driving the generator from the blade hub. This necessitates a generator which is relatively enormous compared to generators in other wind turbines.

Moving to a directly-driven system is approaching size and weight issues however. Compared to their counterparts, directly-driven wind turbines suffer from heavier tower head weights due to the large generators. In the biggest versions supplied by Enercon, the generators are approaching technical as well as economically feasible limits for lifting them high into the air for assembly [23][24].

The gearbox of a wind turbine is placed in a unique situation, one in which the load is stochastically varying and only partial. A failure of this component can cripple a turbine for long periods of time. In the early years of wind turbines, during the WEGA (from the German 'Wind Energie Große Anlagen') program in Europe, a gearbox failure crippled the Tjaereborg turbine in Denmark for 16 months [25]. Indeed one of the largest sources of unplanned maintenance in offshore wind farms in the United Kingdom was the gearbox itself or the gearbox bearings [26]-[29]. Many times this necessitated a replacement of the entire gearbox. Noise complaints are also becoming more common as turbines are placed in urban areas. According to [25], in many cases where complaints about noise were raised from nearby residents, the gearbox was found to be the source.

The gearbox collectively refers to the gears composing different stages housed inside a casing with bearings. This component has been a great concern of the wind industry since its advent in the 1980's. At the time, specialized gearing stages had not

been engineered for wind turbines and thus regular industrial gears were used on these early turbines. Shortly thereafter, it became apparent that these regular gearboxes were ill-suited for the application, and gearbox manufacturers began designing units specifically for their wind turbine customers. Once turbines of 500 kW reached production in the 1990's, gearbox manufacturers began designing planetary stages for added torque density. As wind turbines have continued to grow in size and torque output from the hub, gearbox manufacturers have struggled to keep up with the higher ratings, as well as the demanding requirements of a wind turbine. Gear manufacturers readily admit that wind turbines are the most demanding application which they supply, one in which the loads are variable and arduous to predict [30].

Due to the demanding requirements and technical ability required to design a good gearbox, the field of suppliers for wind turbine manufacturers is greatly narrowed compared to other applications. As of 2005, only two gearbox manufacturers supplied roughly 80% of the wind turbine market, Winergy of Germany and Hansen of Belgium. This forces some wind turbine manufacturers to purchase gearboxes from companies which are owned by rival wind turbine manufacturers. Winergy, owned by Siemens, also supplies Vestas and GE among others. This also limits the variety of gearboxes that a wind turbine manufacturer can spread across its production line. In order to hedge against a single gearbox having a failure across a fleet of turbines, as well as supply-chain interruptions, gearboxes from multiple suppliers will be used in a fleet [31]. The merits of this tactic are best illustrated with the failure of Jahnel-Kestermann gearboxes

in NEG Micon turbines in the late 1990's. This problem, reported in [32] at the time, brought NEG Micon to the brink of collapse, right before they were acquired by Vestas.

Some headway has been made into understanding the causes of gearbox failures. It has been found that bearings are a key instigator in failures, emitting debris which causes damage to the gear itself. In addition, manufacturers have moved away from spherical roller bearings to tapered and cylindrical roller bearings to handle higher torque loads. It is reiterated here that partial loads are a difficult problem for bearings and the gearbox in general. In order for bearings to reduce their failure rate, load prediction is a key issue which must be solved. Progress is slow however due to the proprietary nature among bearing and gearbox manufacturers [33].

Despite the troubles reported by industry, negating the gearbox altogether may not be the answer. In [34] and [35], variations on wind turbine drive trains were examined for weight, cost, and efficiency. In [34], a direct-drive solution for a 1.5 MW wind turbine was roughly 20 tons heavier in the tower head then a fully-geared or single-stage geared design. In addition, the direct-drive solution was more expensive due to the higher costs of magnetic steel laminates and copper in the generator.

Later, in [35], a 5 MW design was carried out using only a single-stage gearbox, termed 'multibrid' ('multi' for multi-megawatt and 'brid' for hybrid). A single-stage gearbox with a gearing ratio of 1/6.17 was designed in order to increase the generator speed past 100 rpm. It was found that this design increased reliability by lowering the rotational speeds which the gearbox has to handle compared to multi-stage high-speed gearboxes, as well as winding temperatures compared to a large direct-drive generator.

It is believed that incorporating a single-stage gearbox in order to increase the generator speed past 100 rpm will benefit the reliability and performance of the entire drive train. In addition, the replacement of a conventional gearbox with a magnetic one will further increase reliability and reduce maintenance.

The advantages of using magnetic gears over traditional gearboxes include inherent overload protection. Gears which are pushed by torque transients over their torque rating will slip, instead of possibly breaking teeth. They also provide the advantage of lower acoustic noise due to the loss of mechanical contact between the teeth. Furthermore, with the loss of contact between teeth, lubrication is negated and thus maintenance due to oil changes [5].

II.1.2. Marine propulsion

In an effort to further increase efficiency as well as reliability, marine propulsion systems are becoming increasingly electromechanical. Electric propulsion has not only migrated towards technology which increases torque density of the electric machine, but also technology such as pod propulsion which can provide 360º thrust capability. In addition, high temperature superconducting (HTS) machines are being studied and built for their increased torque density. These represent some of the state-of-the-art technologies which are currently being developed and improved upon for future marine vessels.

Marine propulsion is an application which demands high torque at low speed. In electric machines, this tends to require high pole numbers as well as high current. Electric machines which are rated for megawatts and the speed rating for large marine

applications, i.e. no more than roughly 250 rpm, are quite large. In [36], an induction machine prototype rated for 19 MW and 150 rpm weighed in at a gargantuan 117 Tonnes and occupied over 85 m^3. However, induction machine technology, while time-tested, yields poor torque density among modern electric machines.

Since that prototype, over the last decade, naval machines have been migrating towards permanent magnets as well as HTS technology to increase torque density. According to [37], induction machine torque densities are in the range of 3.5 ft-lbs/lb while advanced permanent magnet and HTS machines are in the range of 16 ft-lbs/lb. More specifically in [38], modern machine types were compared with the same torque rating, 2 Mft-lbs. Under the comparison permanent magnet machines were on the high end with up to 17.2 ft-lbs/lb while HTS machines were on the low end with 14.2 ft-lbs/lb.

Magnetic gears have been explored more in recent years with the advent of rare-earth permanent magnets. Gears studied in [4], [5], [11], and [12] range from concentric planetary gears to newer more exotic versions such as the cycloid and harmonic gear. The torque densities for the gears studied and built range from 72 Nm/l for early prototypes all the way to 185 Nm/l for the latest prototypes, compared with 30 Nm/l for liquid-cooled electric machines.

II.1.3. Hybrid electric vehicles

The application of vehicle traction is also very popular among the power community and guaranteed to spur further research. The possibilities for drive train layouts are more numerous than those of wind turbines. Another type of electromagnetic gearing machine,

the transmotor, will be examined here for its use in conjunction with the magnetic gear for vehicle traction.

The transmotor is a speed summing electric machine in which the stator, which is usually mechanically grounded, is left to rotate freely on bearings along with the rotor. It is a three-port device, with two mechanical ports, the shafts connected to the rotor and stator, and the electrical port connected to the windings on the stator. Shown in Fig. 5, the transmotor has windings on the stator, while the rotor could have permanent magnets or be a synchronous reluctance type of rotor made solely from silicon steel.

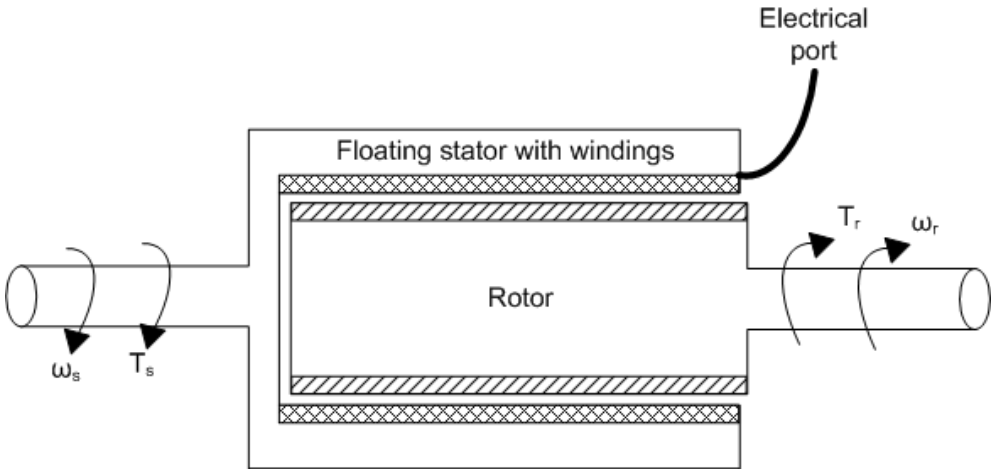

Fig. 5. The transmotor.

One of the first studies of this machine is found in [39]. Here a study was taken to find hybrid electric vehicle (HEV) drive trains which could benefit from new types of gearing. The transmotor, presented as an electromagnetic gear, was studied by looking at all of the different operating modes. Nine distinct operating modes were found, representing cases in which the stator and rotor were either free to move or locked in

position. The power at the electrical port was found through a speed summation in (6). The torque coupling of the machine was found to be just a 1:1 coupling however, as shown in (7).

$$P_{elec} = T_r(\omega_r + \omega_s) \tag{6}$$

$$|T_r| = |T_s| \tag{7}$$

As stated earlier, each of the nine distinct operating modes fell within one of the four categories for operation of an electric machine, except for the case in which the rotor and stator rotated with the same speed, in which case the machine simply functions as an electromagnetic lock. The structure of the electric machine was assumed to be either that of a switched reluctance machine (SRM) or a DC machine for the operating mode in which the rotor was locked. However, for the case in which $\omega_s=\omega_r$, only the SRM was found to be capable of operating in this mode in steady-state.

An HEV drive train is something which can vary drastically based upon fundamental requirements. Most traditional vehicles consist of the same type of drive train, usually varying only in how many wheels are connected to the torque coming from the internal combustion engine (ICE). However, the variation in HEV drive trains can utilize multiple types of gearing, and even disconnect the ICE from the mechanical drive train altogether.

In the series HEV, the ICE simply provides the torque to run a generator. The electrical power from the generator is stored in batteries, and also used to run electric traction motors for the wheels. In a parallel HEV, the ICE and an electric traction motor are connected via a planetary mechanical gearbox to add their torques together. In

another type, the series/parallel HEV, the ICE, an electric traction motor, and a generator are all used in conjunction to either generate electric power or torque for the wheels [40].

The idea behind using an electric machine for vehicle traction dates back to 1900 with [41]. In this example, an electric machine with a floating stator was situated between the rear wheels of a car to provide traction. An HEV drive train shown in Fig. 6 combines many of the elements proposed in [39],[40],[42], and [43]. Here, a transmotor is placed on the driveshaft of a rear-wheel drive vehicle. In the most basic form, there is a combination of clutches and/or locks before and after the transmotor to allow it to operate in the different modes discussed in [39]. This allows the torque from the wheels to be captured by regenerative braking, one of the key advantages of an HEV. It also allows the transmotor to serve as the starter motor for the ICE.

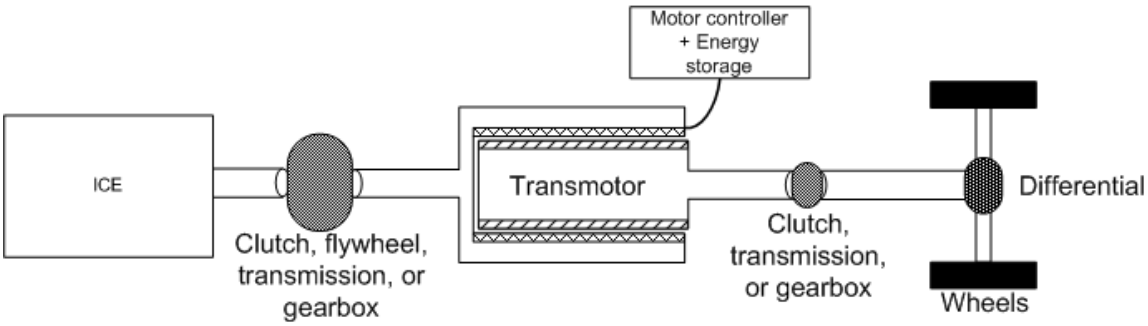

Fig. 6. HEV drive train with transmotor.

The most prominent drawback of the system first proposed in [39] however was the absence of any torque amplification usually required of an ICE during acceleration. At the end of the thesis, it was proposed to add a flywheel between the ICE and transmotor to capture torque transients, also suggested in [42]. The flywheel would also be capable

of delivering torque when needed, and allow the transmotor to be sized smaller. Another drawback to the transmotor has due to do with the need for slip rings with a rotating stator.

More versions in [40] place a transmission in front or behind the transmotor, referred to as ‘posttransmission’ and ‘pretransmission’ respectively. When the transmotor is placed in front of the transmission on the drive train, the ICE and transmotor have the same speed range, and the electric machine can be sized smaller. When the transmotor is placed behind the transmission on the drive train, this serves to optimize the operating points of the ICE, and requires a larger electric machine.

Vehicle traction with the use of magnetic gears is an idea which is relatively new, and has only recently been presented in the literature [44]-[47]. The idea behind using a magnetic gear for traction is similar to the system proposed in [41]. The system is composed of an electromechanical element connected directly to the wheels or via a gear directly in line with the wheels. In [44],[45], and [47] the magnetic gear is sized to accommodate a permanent magnet synchronous machine within the interior of the gear specifically for vehicle traction. Thus, the electromechanical gearbox is a self-contained unit, which could even be capable of fitting inside the wheel itself. This idea is shown in Fig. 7a, with the outer rotor of the magnetic gear connected directly to the rim of the wheel. Fig. 7b shows an assembly of the integrated magnetic gear and PM machine with a more ideal construction. The two magnetic rings are free to rotate, while the two stators are mechanically grounded.

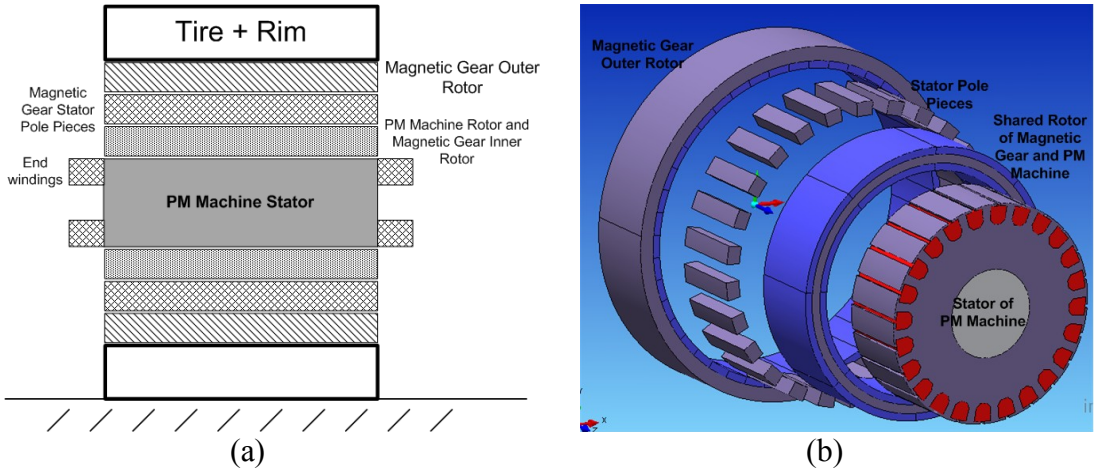

Fig. 7. Integrated magnetic gear/PM machine for traction shown (a) inside wheel and (b) in an assembly of fundamental elements.

Like the transmotor, this integrated magnetic gear/PM machine is a three-port device, with two mechanical ports consisting of the rotors, and the electrical port of the permanent magnet synchronous machine. This unit has the advantage of keeping the stators mechanically grounded, and thus slip rings are not needed, which can significantly increase the volume needed for the machine. This type of unit lends itself easily to the series HEV drive train shown in Fig. 8. The key advantage to this arrangement over previously constructed series HEV drive trains is that the size of the electric traction motor is reduced due to the magnetic gear. In [47], the integrated unit has a calculated torque density of 130 Nm/l. A unit could be placed on multiple wheels and provide independent torque and speed control of their respective wheels.

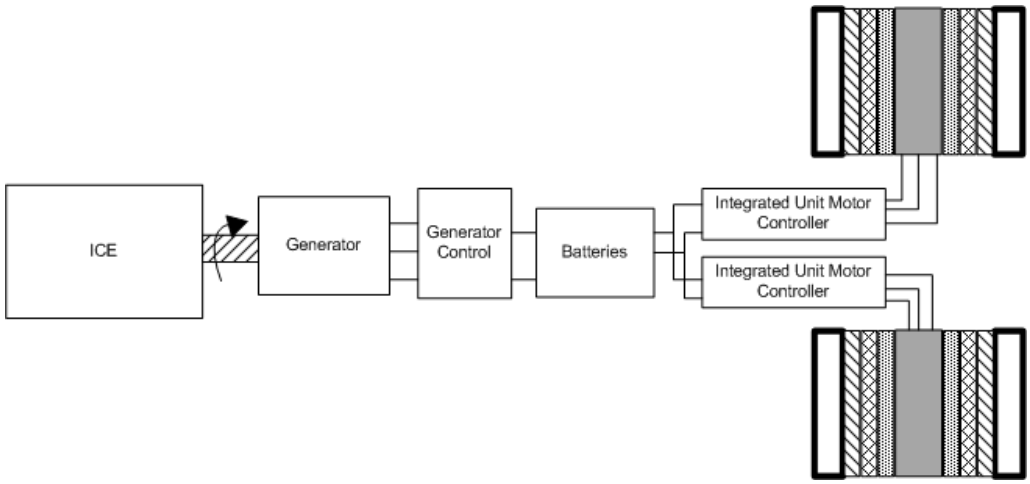

Fig. 8. Series HEV drive train with integrated magnetic gear/PM machine traction units.

The drive train shown in Fig. 8 suffers from the fact that it requires three electric machines, two in the integrated traction units, and one for electric power generation from the ICE. The added complexity for control of three electric machines is also a drawback. Looking again at the drive train with the transmotor in Fig. 6, one of the key drawbacks was the need for torque amplification from the ICE during acceleration. With the torque amplification of a gear, the ICE can be sized smaller. This drive train could be helped with the addition of a magnetic gearbox shown in Fig. 9.

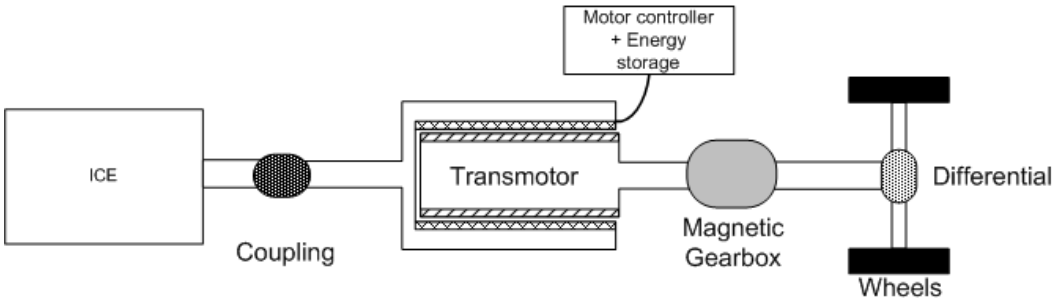

Fig. 9. HEV drive train with transmotor.

The drive train in Fig. 9 has the advantage of needing control of only one electric machine. It has the ability to capture energy from regenerative braking, and the ICE is reduced in size due to the magnetic gearbox. The magnetic gear is a passive element and does not need its own controller.

A more complex HEV drive train is employed in the Toyota Prius and Camry, referred to as an integrated speed- and torque-coupling drive train. A transmotor drive train is proposed in [40] which retains the same advantages of the Toyota Prius and Camry, while still requiring an electric traction motor. This drive train has the advantages of being able to use an electric machine for regenerative braking, while also being able to employ both the ICE and the electric traction motor for torque. However, the drive train proposed can still be improved with the replacement of the electric traction motor by the integrated magnetic gear/PM machine. The increased torque density over a traditional liquid-cooled machine would require the use of a smaller overall system for traction, shown in Fig. 10.

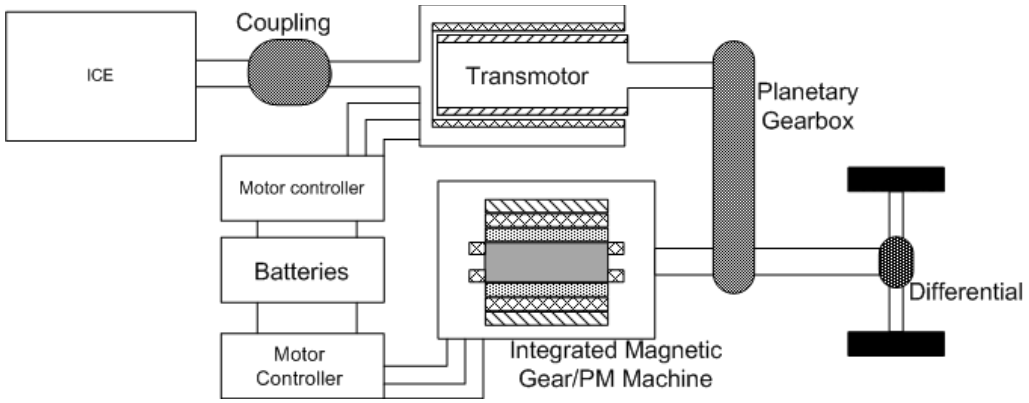

Fig. 10. Integrated speed- and torque-coupling drive train with transmotor and integrated magnetic gear/PM machine.

Looking at the Toyota Camry data presented in [47] and [48], the electric traction motor has a max torque of 270 Nm. The traction motor is interfaced to the wheels via a gearbox with a gear ratio of 8.78:1. The active volume of the electric traction motor is 3.34 L and the base model engine has a power rating of 169 hp. The traction motor has an excellent torque density due to its liquid cooling arrangement. However, this could still be improved by replacing it with the integrated magnetic gear/PM machine, reducing the volume needed down to roughly 2 L (assuming a torque density of 130 Nm/l).

Conversely, the volume could be kept the same and the torque output could be increased to 434 Nm. The power rating of the ICE could be reduced by the added torque from the electromechanical traction unit. The traction motor is capable of delivering up to 42.4 kW in the constant torque region (0-1500 rpm). With the added torque of the magnetic gearing element, the unit could be capable of delivering 68 kW, a 60% increase. Assuming that the added power of the traction unit could be deducted directly from the ICE, the horsepower rating could be reduced by 34. In either case, the arrangement would have the added benefit of eliminating the liquid cooling mechanism needed for the traction motor. In addition, by reducing the size of the ICE, the size of the transmotor which is coupled to it is also reduced.

There are numerous layouts for an HEV drive train, each with their own advantages and disadvantages. The transmotor HEV drive train which had been proposed has the limitation of not being able to amplify torque from the ICE. With the use of a magnetic gear, this torque can be amplified to reduce the size of the ICE. In addition, in a more

complex arrangement, a transmotor can be used with an integrated magnetic gear/PM machine to provide an integrated speed- and torque-coupling drive train similar to the Toyota Prius and Camry. The addition of magnetic gearing elements in general serve to either reduce the volume of the electromechanical elements needed, or can be sized as previously done and reduce the size of the ICE.

II.2. The Concentric Planetary Magnetic Gear

A concentric planetary magnetic gear is shown in Fig. 11, with 31 outer and 5 inner pole pairs. In any variation of this type of magnetic gear, there are two magnetic rings and a set of pole pieces in-between the magnetic rings to modulate the magnetic flux. The yokes of the two magnetic rings and the pole pieces are composed of silicon steel.

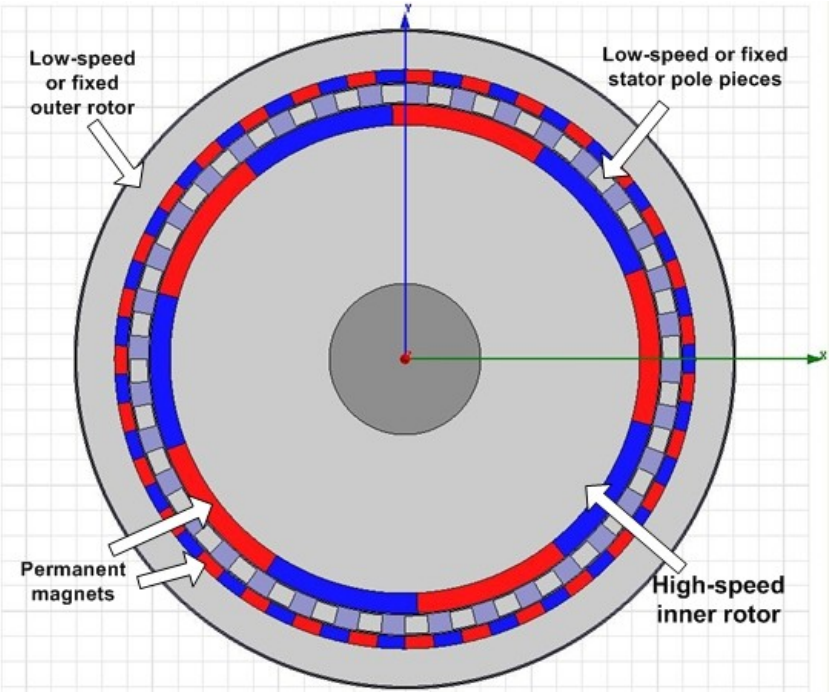

Fig. 11. Magnetic gear with 31 outer and 5 inner pole pairs.

The modulation segments (i.e. the pole pieces) are necessary in magnetic gears in order to transmit torque at different rotational speeds. In magnetic couplings, these modulation segments are absent due to the fact that the rotors have identical pole numbers. Illustrated in Fig. 12, the radial flux density is shown near the inner and outer rotors. The gear, with 4 and 22 inner and outer pole pairs respectively, has the same dominant harmonic in the radial flux density waveforms close to the surface of the magnets. In essence, the modulation segments serve to make the rotors look as if the opposite rotor has the same number of poles.

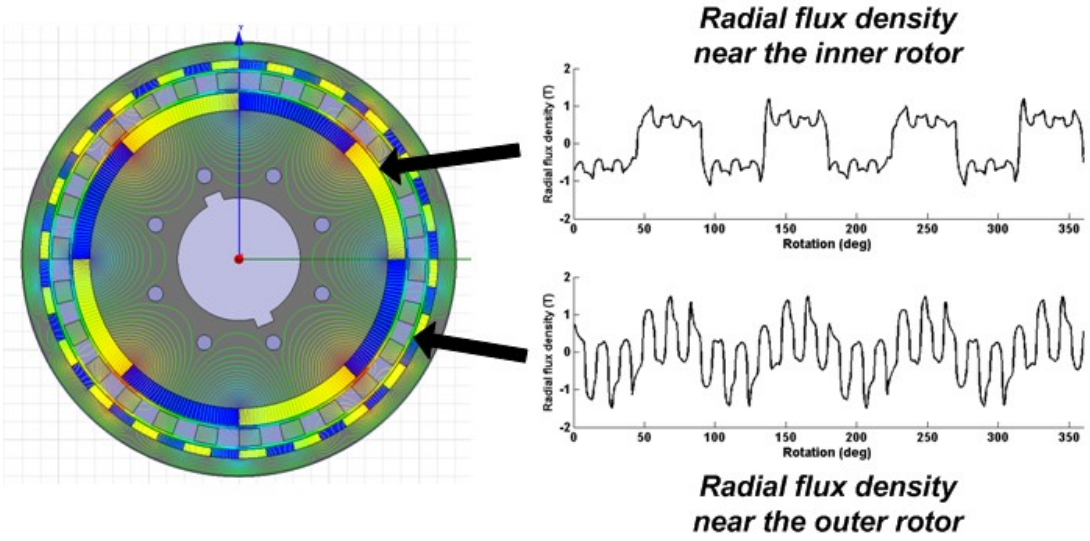

Fig. 12. The modulation of the radial flux density due to the pole pieces in a gear with 4 inner and 22 outer pole pairs.

II.2.1. Equilibrium and gear ratio

In the concentric planetary gear shown in Fig. 13, there are three possibilities for operation, each with its own gearing ratio. In Fig. 13a, the outer permanent magnet ring

is fixed, while the stator pieces and inner permanent magnet ring rotate concurrently. In Fig. 13b, the stator pieces are fixed while the two permanent magnet rings are counter-rotated. In Fig. 13c, the inner magnetic ring is fixed while the outer magnetic ring and stator pieces rotate concurrently. At the same time, the pole combination for the outer permanent magnet and inner permanent magnet rings should be considered. The combination of pole pairs can determine not only the gear ratio, but also the amount of ripple in the torque transmission. In certain applications a high amount of torque ripple may not be acceptable. However, there could be a trade-off to keep the gear ratio high in order to reduce the size of the generator.

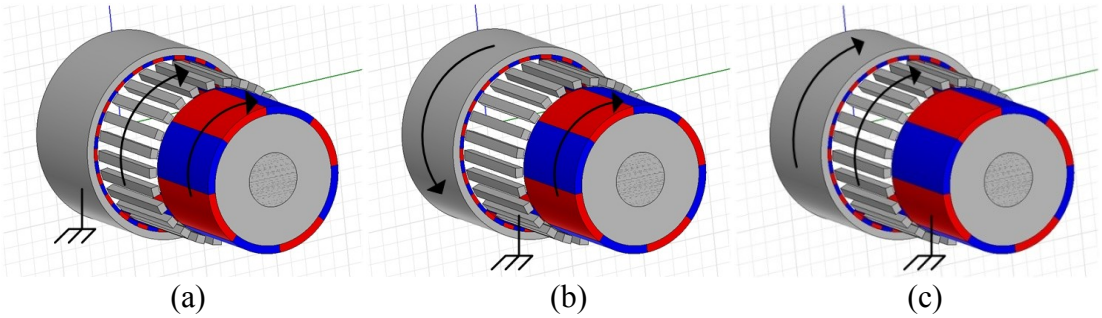

Fig. 13. Assembly showing (a) outer magnetic ring fixed, (b) stator segments fixed, and (c) inner magnetic ring fixed.

The gearing ratios are derived by the process given in [4]. Using a Fourier series for the radial flux density due to the magnets, as well as a modulation function to account for the pole pieces, it is shown that a general Willis equation emerges for the magnetic gear, shown in (8). In (8), m is the order of the space harmonic components and k is the order of space harmonic components due to the introduction of the pole pieces. Indeed,

the mechanical planetary gear components have duals in the magnetic gear. The carrier is a dual to the modulation segments, while the sun gear and ring gear are duals to the inner and outer rotors respectively.

$$\omega_{m,k} = \frac{mp}{mp + kn_s}\omega_r + \frac{kn_s}{mp + kn_s}\omega_s \tag{8}$$

In mechanical planetary gears, k is limited between -1 and 0. In magnetic gears, the highest torque transmission capability results when m=1 and k=-1, resulting in the relationship between the outer pole pairs p_o, inner pole pairs p_i, and stator pole pieces n_s, shown in (9). This results in the Willis equation shown in (10) between the two rotors ω_{r1} and ω_{r2}, and stator pole piece arrangement ω_s, rotational velocities [49][50].

$$p_o = \left| p_i - n_s \right| \tag{9}$$

$$\omega_{r1} = \frac{p}{p - n_s}\omega_{r2} - \frac{n_s}{p - n_s}\omega_s \tag{10}$$

The gearing ratios for the magnetic gear which can be derived from (9) and (10) cover the three modes of operation, given by (11), (12), and (13). A larger difference between pole pairs will result in a higher gearing ratio. Equation (11) covers the mode of operation described in Fig. 13a, (12) covers the mode of operation in Fig. 13b, and (13) covers the mode of operation shown in Fig. 13c.

$$G = \frac{-n_s}{p_o - n_s} = \frac{n_s}{p_i} \tag{11}$$

$$G = \frac{p_i - n_s}{p_i} = -\frac{p_o}{p_i} \tag{12}$$

$$G = \frac{-n_s}{p_i - n_s} = \frac{n_s}{p_o} \tag{13}$$

The equilibrium point for the gear reveals behavioral characteristics of the gear. If one rotor is fixed while the other is rotated, a torque will be exerted until the gear reaches its stall torque rating, at which point it will slip to the next equilibrium point. If the rotor is held below the stall point, and released, the rotor will oscillate between stall points like a spring. This reveals the natural overload protection of the gear, a torque exceeding the stall torque rating of the gear will cause it to slip. A simulation can reveal the physical equilibrium points of the gear. The corresponding torque curves in Fig. 14, representing the torque exerted on the two rotors, intersect at the equilibrium points. Depending upon which rotor is held fixed, the movement required to make the other rotor slip will behave according to the gear ratio.

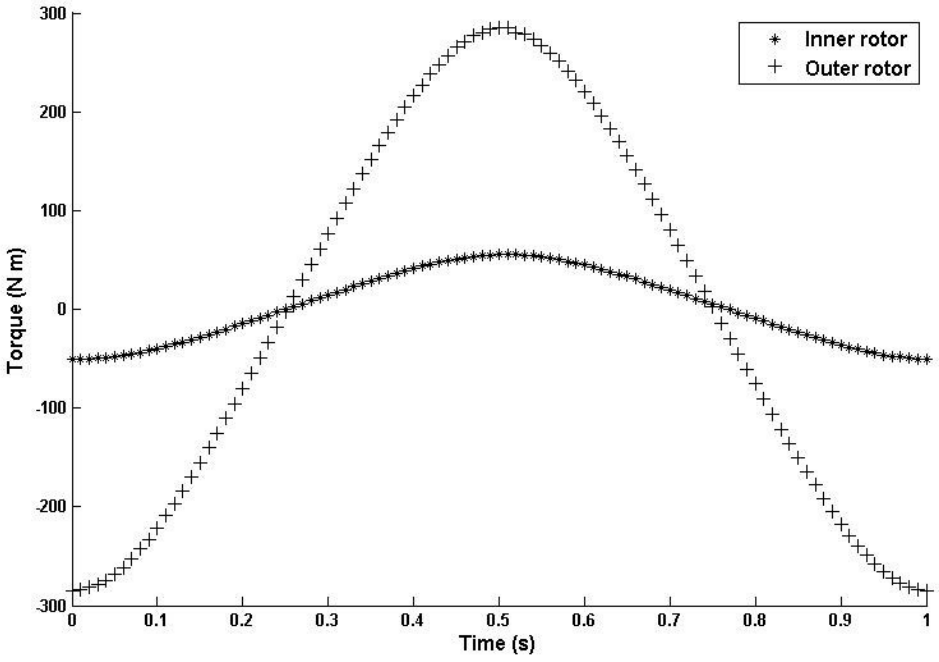

Fig. 14. Torque curves revealing equilibrium points for the 22/4 magnetic gear.

II.2.2. Effect of gear ratio upon torque ripple

By picking thirteen different pole pair combinations in Table I, twenty six different gearing ratios can be simulated and studied for their torque ripple characteristics. The dimensions chosen for the simulation of the different gear models were based upon the notion that a future prototype would be built from one of these models. Thus dimensions are scaled down from a gear which would be implemented in industry, to one which will be implemented in the lab. In addition, the mode of operation in which the inner magnetic ring is fixed is not considered due to its low gearing ratio.

Table I. Gear ratios for chosen pole pair ratio models

Pole Pair Ratio	**Gear Ratios**	
	Stator Pieces Fixed	***Outer Ring Fixed***
22/6	3.67/1	4.67/1
34/6	5.67/1	6.67/1
35/6	5.83/1	6.83/1
31/5	6.2/1	7.2/1
34/5	6.8/1	7.8/1
22/4	5.5/1	6.5/1
28/4	7/1	8/1
29/4	7.25/1	8.25/1
30/4	7.5/1	8.5/1
31/4	7.75/1	8.75/1
20/2	10/1	11/1
21/2	10.5/1	11.5/1

Pole pitch differed among the five different models, along with the number of magnets and stator pole pieces. In order to compare the models, the pitch of all magnets was as great as possible, and the stator pole pieces only spanned half of their maximum possible pitch. For example, the 22/6 model contains 28 stator pole pieces, each one

having a pitch of 6.43º. The dimensions which are common to all the models are given in Table II.

With the chosen dimensions and parameters for the different gear models, simulations are setup in Maxwell. The magnets used in the simulation are composed of Neodymium from Ansoft's built-in library, and radially-magnetized. The yokes for the outer and inner rotors are composed of AK Steel M-45 non-oriented electrical steel. The stator pole pieces are composed of AK Steel M-6 grain-oriented electrical steel.

Table II. Dimensions for models in preliminary gearing ratio analysis

Parameter	Value [mm]
Outer radius of inner rotor yoke	93
Inner radius of outer rotor yoke	115
Outer radius of outer rotor yoke	130
Outer radius of the stator pole pieces	109
Inner radius of the stator pole pieces	102
Shaft radius	30
Stack length	50
Magnet thickness on inner rotor	8
Magnet thickness on outer rotor	5

Care must be taken to note the starting position for the gear simulation. The starting point was determined by looking for the equilibrium points for a gear. A simulation in which one rotor was rotated while keeping the stator pieces and the other rotor fixed was executed. The outer rotor was rotated two full pole pitches in 1 second.

Determining the speed at which to compare the models involved looking at different speeds and their torque ripple characteristics. In Fig. 15, the 22/4 combination gear was given a step change in speed, beginning at 50 rpm on the inner rotor, then increasing to 150 rpm at 0.5 s. From looking at the torque transfer plot in Fig. 15, it is evident that the

frequency of the torque ripple changes with speed, but the percentage magnitude remains fairly constant. Thus, speed was kept to a minimum in order to sample the torque waveforms quickly enough and run each model's simulation in a timely manner.

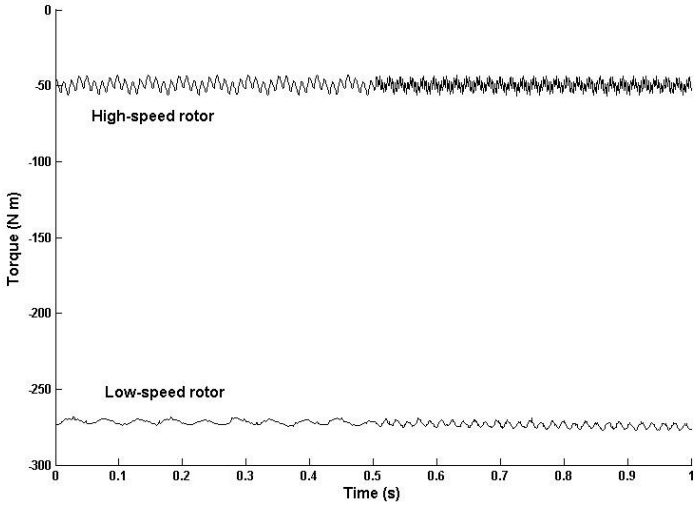

Fig. 15. Torque transfer showing ripple with change in speed.

The gear ratios in Table I were simulated at the same base speed of 60 rpm for the high-speed rotor, i.e. the one which would be attached to the electric machine. The low-speed rotor was spun according to the gear ratio. A simulation of 1/4 second was then carried out for all the models, sampled at 1 kHz.

The plots are divided among three different performance classes which emerged after running the simulations. Models with whole gear ratios offered the worst performance, in Fig. 16, followed by models with half and third gear ratios in Fig. 17. Other fractional gear ratios, shown in Fig. 18, offered the best performance. All of the figures show torque ripple percentage of both the high-speed rotor and low-speed rotors, representing both operating modes. Between the two operating modes per model

tabulated in Table III, the torque ripple percentages show little change. Table III shows the torque ripple of the inner permanent magnet rotor, the one which would be attached to the electric machine, in either operating mode.

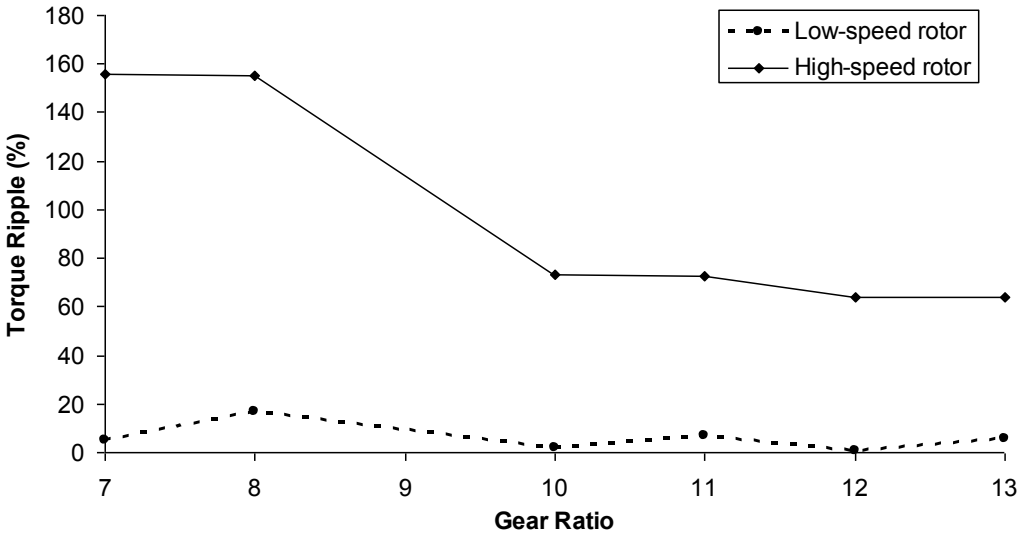

Fig. 16. Percentage torque ripple for high-speed and low-speed rotors for whole gear ratios.

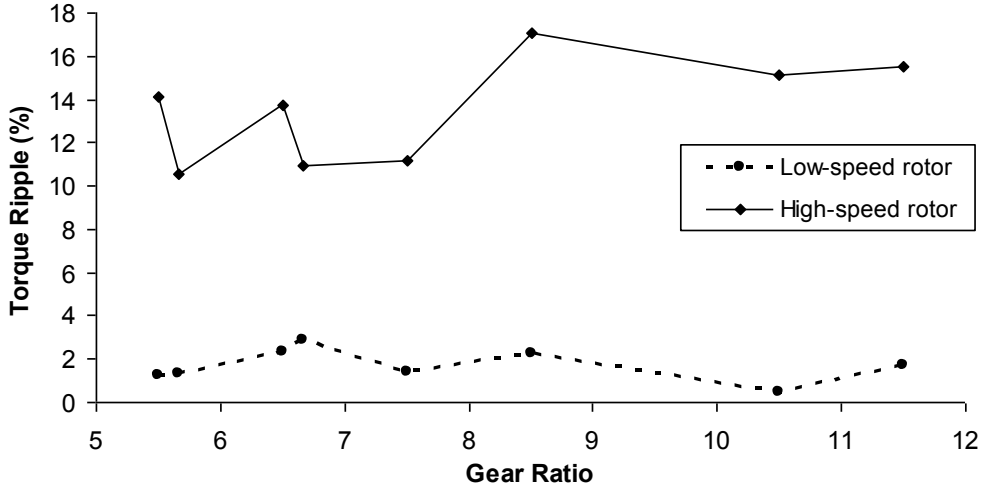

Fig. 17. Percentage torque ripple for high-speed and low-speed rotors for half and third gear ratios.

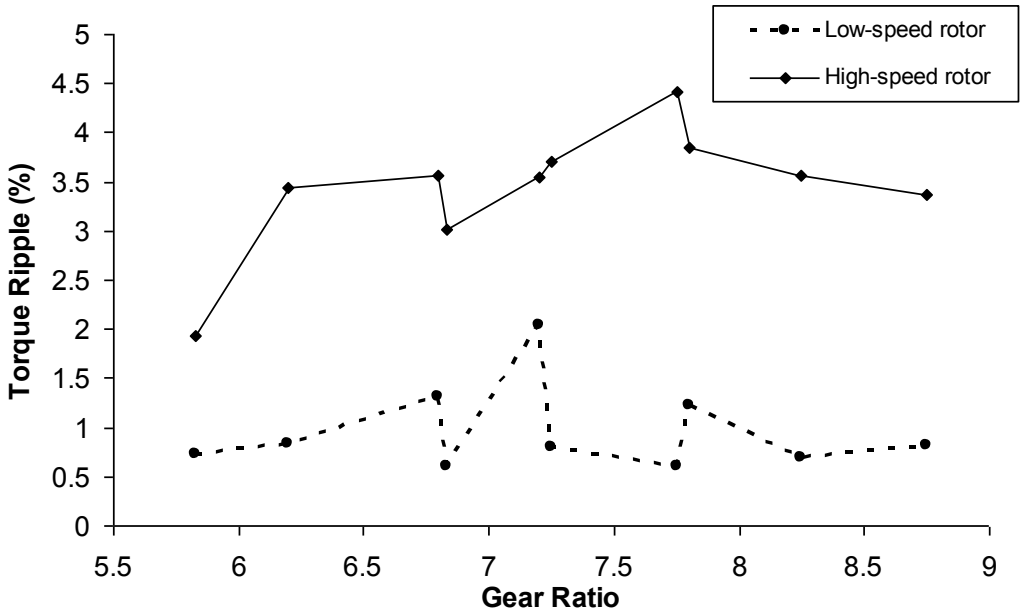

Fig. 18. Percentage torque ripple for high-speed and low-speed rotors for remaining fractional gear ratios.

Table III. Torque ripple results between operating modes

Pole Pair Ratio	**Percent Torque Ripple of Inner Rotor**	
	Stator Fixed	***Outer Rotor Fixed***
22/6	13.92	14.41
34/6	10.58	10.93
35/6	1.94	3.01
31/5	3.44	3.55
34/5	3.57	3.85
22/4	14.12	13.75
28/4	156.10	155.23
29/4	3.70	3.57
30/4	11.14	17.06
31/4	4.42	3.37
20/2	73.38	72.39
21/2	15.13	15.53
24/2	64.23	64.10

Torque ripple in the modeled gears is caused by the interaction of the permanent magnets with the stator pole pieces [4]. The causes of the high torque ripple among whole gear ratios compared to fractional gear ratios can be understood better by examining common multiples between pole pairs. In gears with the worst performance, the dominant order of the torque ripple waveform was one or two times the value of the least common multiple between the number of inner pole pairs, p_i, and the poles on the low-speed rotor. This would either be the number of stator pole pieces, n_s, given by LCM (p_i, n_s) for fixed-stator operation. Or it could be the number of pole pairs on the outer rotor, p_o, given by LCM (p_o, p_i) for fixed outer-rotor operation.

A higher value of the least common multiple would result in a higher fundamental order of the cogging torque waveform, and less ripple percentage. This correlates well with the torque results by looking at the least common multiple for the gear with the worst performance, 28/4, which has a least common multiple of 32, for fixed stator operation, and 28 for fixed outer-rotor operation. Fig. 19 shows torque transfer waveforms for both modes of operation in the 28/4 gear. The gear with the best performance, 35/6, has a least common multiple of 246 for fixed-stator operation, and 210 for fixed outer-rotor operation.

This suggests that higher gear ratios will naturally have higher least common multiples, and thus a higher torque ripple fundamental order. However, there remains a practical limit to the amount of pole pairs which can be placed on the outer rotor. As shown in Fig. 20, there are leakage flux paths which circulate between adjacent magnets

on both magnetic rings. Increasing the number of pole pairs on the outer rotor would increase the number of leakage flux paths and contribute to losses in the magnets.

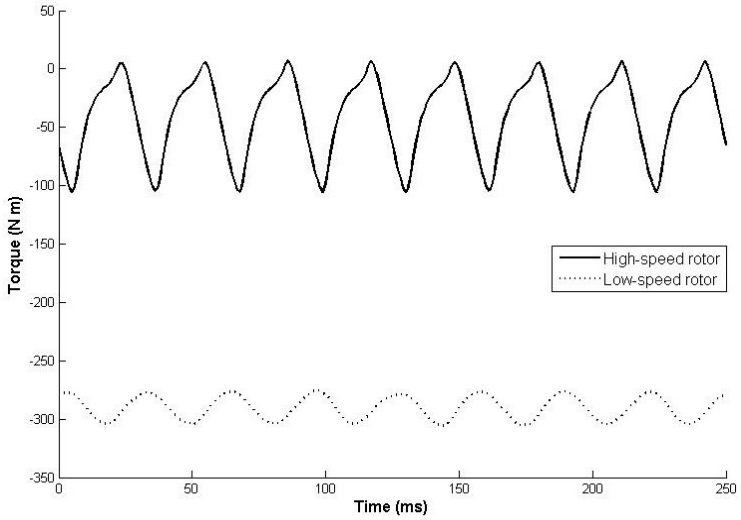

(a)

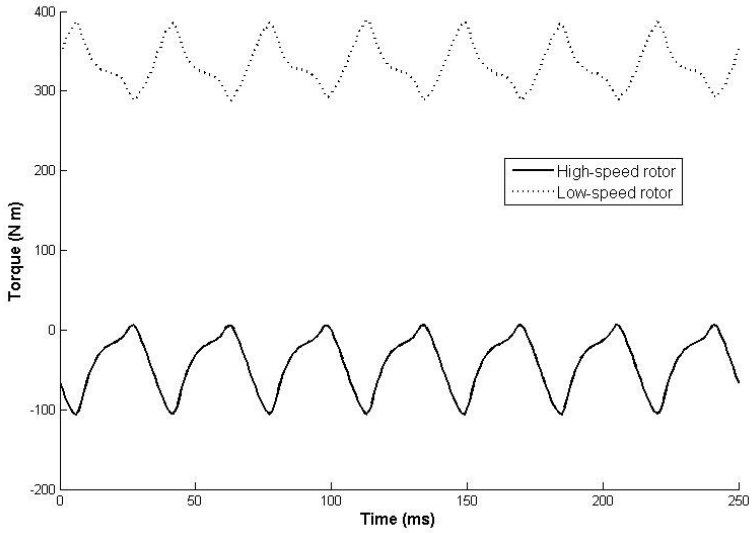

(b)

Fig. 19. Torque transfer in 28/4 gear for (a) fixed stator and (b) fixed outer rotor operation.

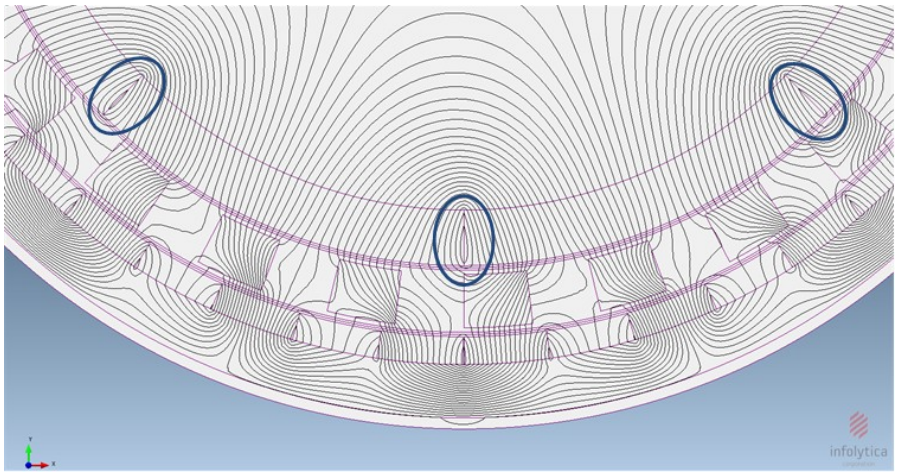

Fig. 20. Flux plot showing leakage flux paths (circled in blue) between adjacent magnets of inner rotor.

II.2.3. Parameters for design

In [4], the prototype gear had an outer diameter of 140 mm, and 27 outer pole pairs. In [5], the prototype gear had an outer diameter of 120 mm and 22 outer pole pairs, using standard rectangular magnets with a width of 7 mm. In the simulated gear for this preliminary analysis, with an outer diameter of 260 mm, fitting up to 35 outer pole pairs is feasible.

In order to choose the optimal gear ratio, the overall dimensions must then be taken into account. Using the results presented, it is recommended to avoid whole, half, 1/3, or even 2/3 gear ratios. Choosing only two pole pairs for the high speed rotor is thus a poor starting point, as it can only provide whole and half gear ratios. Starting with at least four inner pole pairs would allow one to choose a gear ratio which would provide less than 5% ripple torque on the high speed rotor. Increasing the number of pole pairs

on the high speed rotor to five or six would provide more options for gearing ratios with even lower torque ripple.

In addition, the torque ripple shown when fixing the outer permanent magnet ring, is not detrimental to performance, while increasing the gear ratio. It could also offer an advantage in manufacturing as well as mounting of the gear in a wind turbine nacelle.

In looking at the performance of the presented models thus far, the 31/4 model offers the highest gear ratio with acceptable torque transfer performance. It is now investigated whether using designs intended for interior permanent magnet synchronous machines can improve upon the performance of this gear. In Fig. 21, two models are shown which use rectangular magnets with parallel magnetization along with flux barriers in order to impede leakage flux between adjacent magnets.

The performance of the redesigned models compared to the original models is carried out by looking at torque ripple percentage on the inner rotor, which would be attached to the motor/generator, and the stall torque rating of the low-speed rotor, which would be attached to a blade hub or wheel. The stall torque rating is represented by the apex of the torque curve in Fig. 14, in which only one rotor is rotated. Simulations were carried out at a resolution of 10 kHz for the redesigned models, and are shown in Table IV. As expected, the loss of magnet area to the flux barriers produces a loss in stall torque rating. However, the introduction of the flux barriers does show an improvement in torque ripple.

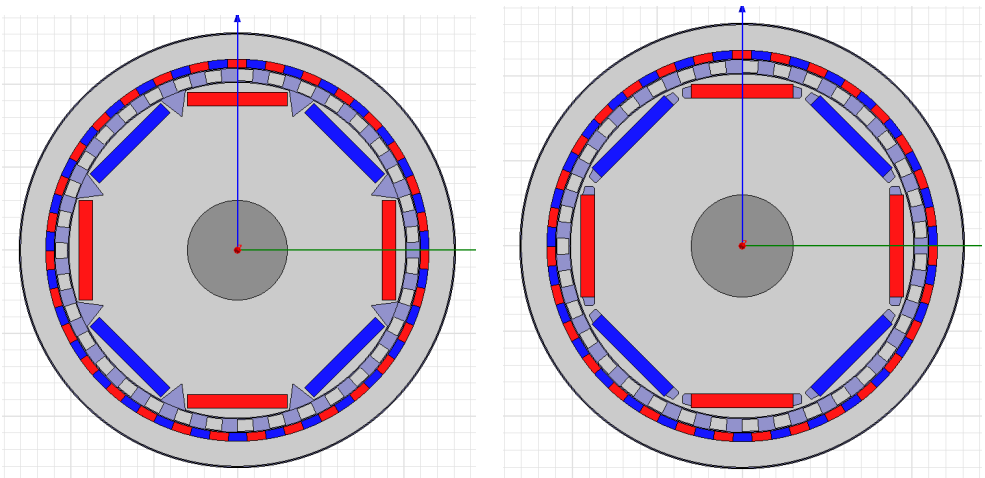

(a) (b)

Fig. 21. 31/4 magnetic gear using (a) saliency for flux barriers and (b) integrated flux barriers.

Table IV. Comparison of performance for 31/4 models

Design	**Percent Torque Ripple of Inner Rotor**		**Stall Torque Rating of Inner Rotor (Nm)**	
	Stator Fixed	***Outer Rotor Fixed***	***Stator Fixed***	***Outer Rotor Fixed***
31/4 original	4.42	3.37	304.60	346.41
31/4 salient	1.37	1.97	257.38	291.81
31/4 integrated	2.09	2.58	250.01	285.23

In comparing the two new designs, it is noted whether the new designs create areas of saturation. In Fig. 22, the magnetic flux density plots are shown for the two models. In the salient design, the areas next to the ends of the magnets experience short-circuiting of the magnetic flux and are saturated. In the integrated design, the magnets still experience some short-circuiting as well, and saturate in the thinnest area close to the perimeter of the rotor.

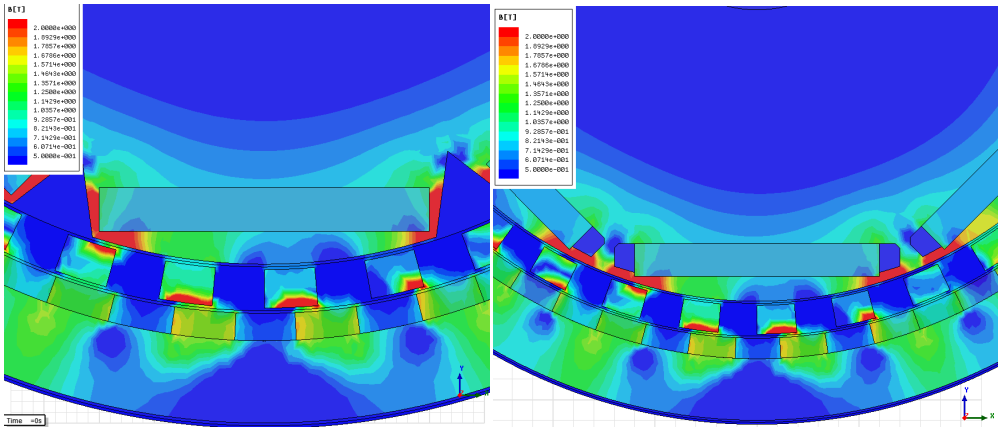

(a) (b)

Fig. 22. 31/4 magnetic gear using (a) saliency for flux barriers and (b) integrated flux barriers.

II.3. Conclusion

Magnetic gear models have been presented and simulated with FEA to study the effects of different pole pair ratios and operating modes on the performance of each gear. It has been found that fractional gear ratios offer the best performance, with an option to increase the gear ratio by fixing the outer permanent magnet ring.

It has also been shown that the design of the high-speed rotor can benefit from techniques used for interior permanent magnet synchronous machine design. The torque ripple can be reduced at the cost of a lower stall torque rating for the gear.

The wind energy industry, along with electric vehicle traction, will continue to grow in production as well as research in the coming years. With the demanded increase in sustainable energy production and efficiency from automobiles, a significant improvement can be made by migrating from mechanical components to

electromechanical ones. With this migration, future wind turbines and cars can continue to improve with maintenance reduction, noise reduction, and increased reliability.

Future marine applications will benefit from electric propulsion systems which have higher torque densities. These systems will facilitate more powerful pod propulsion systems as well as reduce the volume and weight imposed by machines in conventional drive trains. Modern machines, in an effort to increase torque density, have moved into the arena of rare-earth permanent magnets as well as High Temperature Superconducting coils. While these technologies have exhibited exceptional torque densities to date, magnetic gears can further increase the torque densities of electric propulsion systems and bring higher efficiency and reliability to marine vessels.

III. ANALYSIS OF THE MAGNETIC GEAR WITH WINDING FUNCTION THEORY

The analysis of magnetic gears has progressed from that of very simple arrangements to more complex magnetic gears which are currently being studied. Early analysis was carried out on the simplest arrangements for magnetically coupled elements, the 1:1 coaxial coupling and the spur gear. This early work done in [51]-[54] was carried out by using a combination of magnetic field theory and FEA. Magnetic field theory was used in conjunction with Fourier series for the radial and circumferential fields due to the magnets in order to calculate torque. Analysis in [54] calculated the torque in the spur gear by using parallel and radial magnetization vectors for the individual magnets, in which the parallel magnetization was found to give a higher stall torque. This same analysis was applied in [11] to the cycloid gear.

The idealized gear layout, shown in Fig. 23, is comprised of two magnetic rings, and stator pole pieces made of silicon steel between the magnetic rings. There are two modes of operation achieved by either mechanically grounding the stator pole pieces or the outer magnetic ring. The analysis carried out will assume the mode of operation in which the stator pole pieces are mechanically grounded, allowing the magnetic rings to counter-rotate.

This gear has also been analyzed using magnetic field theory in [55]-[57]. The results calculated are very close to that found with FEA. However, a new method of analyzing the gear with considerably less computational burden is needed. This new

method of analyzing the gear should be capable of taking into account geometric variations of the gear such as the shape of the magnets.

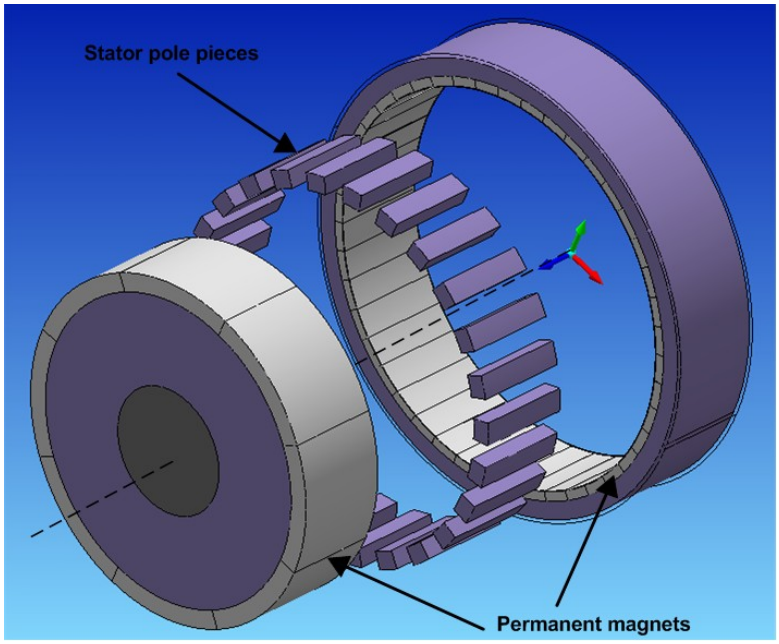

Fig. 23. An idealized construction of the concentric planetary magnetic gear used to develop winding function theory for the gear.

Winding function theory (WFT) has been used primarily on machines without permanent magnets since its early development. It has seen great success when applied to induction machines [58], switched reluctance machines [59], and synchronous reluctance machines [18]. One of the only examples of WFT applied to a permanent magnet machine is found in [19]. However, the radial flux density component due to the magnets is used only to analyze the back-electromotive force (EMF) of the brushless DC (BLDC) machine. The study undertaken here is the first of its kind to apply WFT theory to components with mismatched pole numbers, and no windings at all.

III.1. Winding Function Theory and its Modifications

III.1.1. Basic winding function theory

The derivation of winding function theory begins with a perfectly cylindrical and concentric machine with conductors in the air gap. Later in the analysis, salient air gaps will be handled. Fig. 24 shows the machine with a two-pole winding residing within the air gap. By Ampere's law in (14), the line integral is taken around the conductor in the path 1-2-3-4-1.

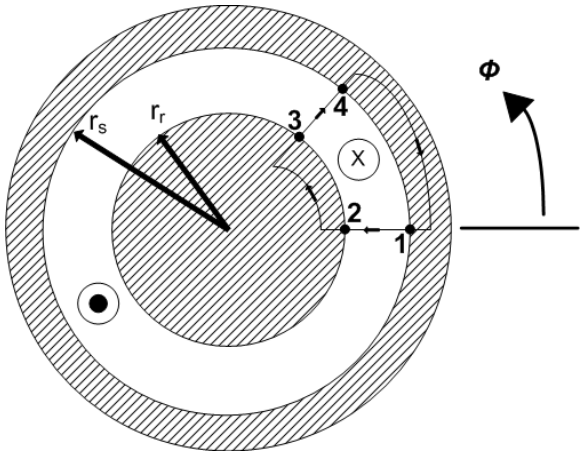

Fig. 24. An idealized machine with conductors in the air gap.

$$\oint H \cdot dl = \int J \cdot ds \tag{14}$$

Following the path 1-2-3-4-1 around the conductor in Fig. 24, the total MMF is calculated in (15). The resultant turns function, $n(\Phi)$, is directly proportional to the MMF in the air gap. The MMF drop in paths 2-3 and 4-1 can be neglected however. This is due to the assumption of the use of linear iron with high relative permeability. With a relative permeability much greater than air, i.e. 10,000, the MMF drop through

the iron is then neglected, leaving the two terms in (16). The magnetic field strength around the air gap, *H(Φ)*, is thus a function of the turns function, in (17).

$$\Im_{12} + \Im_{23} + \Im_{34} + \Im_{41} = n(\phi)i \tag{15}$$

$$\begin{aligned} \Im_{12} &= \int_{r_s}^{r_r} H(r,0)dr = (r_r - r_s)H(0) = -gH(0) \\ \Im_{34} &= \int_{r_r}^{r_s} H(r,\phi)dr = (r_s - r_r)H(\phi) = gH(\phi) \end{aligned} \tag{16}$$

$$H(\phi) = n(\phi)\frac{i}{g} + H(0) \tag{17}$$

Using Gauss' law in (18), the value for the magnetic field strength around the air gap can be found. This assumes a fictitious cylinder encompassing only the rotor of the ideal machine.

$$\begin{aligned} \int B \cdot ds = 0 &= \int_0^l \int_0^{2\pi} \mu_0 H(\phi) r d\varphi dz \\ lr\mu_0 \int_0^{2\pi} H(\phi) d\phi &= 0 \end{aligned} \tag{18}$$

One of the key assumptions of normal winding function theory follows from (18), in that the value of the MMF taken around the circumference of the machine must have no average component, shown in (19).

$$\int_0^{2\pi} \Im_{34}(\phi) d\phi = 0 \tag{19}$$

Through the process shown in (20), the value of *H(Φ)* is found by using the turns function.

$$
\begin{aligned}
lr\mu_0 \int_0^{2\pi} H(\phi)d\phi &= 0 \\
lr\mu_0 \int_0^{2\pi} \left[n(\phi)\frac{i}{g} + H(0) \right] d\phi &= 0 \\
2\pi H(0) + \frac{i}{g}\int_0^{2\pi} n(\phi)d\phi &= 0 \\
H(0) &= -\frac{i}{g}\left[\frac{1}{2\pi}\int_0^{2\pi} n(\phi)d\phi \right] \\
H(\phi) &= \frac{i}{g}\left[n(\phi) - \frac{1}{2\pi}\int_0^{2\pi} n(\phi)d\phi \right] \\
H(\phi) &= \frac{i}{g}\left[n(\phi) - \langle n(\phi) \rangle \right]
\end{aligned}
\tag{20}
$$

From the end result of (20), it is apparent that the magnetic field strength around the air gap is a function of the turns function, *n(Φ)*, minus its average value, which is the winding function, *N(Φ)*, shown in brackets. The differential flux is found in (21). In order to calculate the inductances among windings in the machine, Fig. 25 is used to make sure that orientation is accounted for.

$$
d\phi = B \cdot dA = Brld\phi = \frac{\mu_0 rl}{g} iN(\phi)d\phi \tag{21}
$$

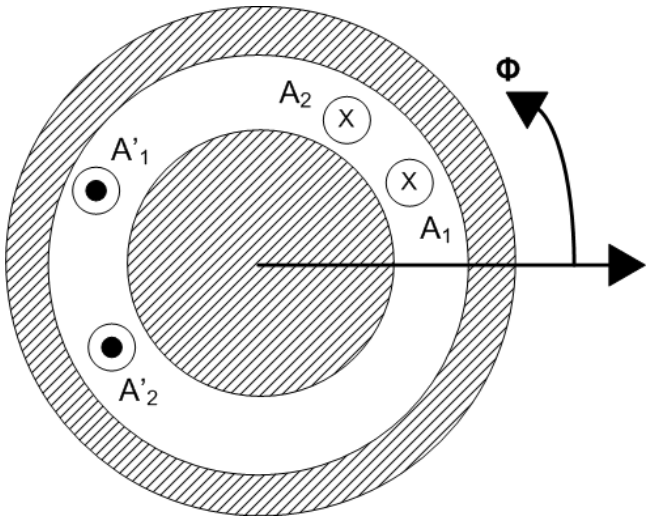

Fig. 25. An idealized machine with multiple coils in the air gap.

Care is taken in (22) to distinguish between the values of flux which can be calculated depending upon the orientation of the winding shown in Fig. 25. The value of (22) could be positive or negative depending upon which coil side of winding A_1 is encountered first.

$$\Phi_{A_1-A_1'} = \frac{\mu_0 r l}{g} \int_{\phi_{A_1}}^{\phi_{A_1'}} i_{A_1} N_{A_1}(\phi) d\phi \tag{22}$$

The problem with accounting for different winding orientations can be handled by including the turns function in the calculation of the flux in (23). Assuming that each winding constitutes its own phase, the mutual flux linkage is shown in (24).

$$\Phi_{A_1-A_1'} = \frac{\mu_0 r l}{g} \int_{\phi_{A_1}}^{\phi_{A_1'}} n_{A_1}(\phi) i_{A_1} N_{A_1}(\phi) d\phi = \frac{\mu_0 r l}{g} \int_{0}^{2\pi} n_{A_1}(\phi) i_{A_1} N_{A_1}(\phi) d\phi \tag{23}$$

$$\lambda_{A_2 A_1} = \frac{\mu_0 r l}{g} \int_0^{2\pi} n_{A_2}(\phi) i_{A_1} N_{A_1}(\phi) d\phi \tag{24}$$

Now that the flux linkage has been found, the mutual inductance of the windings easily follows in (25). In addition, the derivation did not take into account whether the windings were on the rotor or stator. The derivation is also valid if the windings are the same, thus giving the magnetizing inductance in (26)[60][61].

$$L_{A_1 A_2} = \frac{\lambda_{A_1 A_2}}{i_A} = \frac{\mu_0 r l}{g} \int_0^{2\pi} n_{A_1}(\phi) N_{A_2}(\phi) d\phi \tag{25}$$

$$L_{A_1 A_1} = \frac{\lambda_{A_1 A_1}}{i_A} = \frac{\mu_0 r l}{g} \int_0^{2\pi} n_{A_1}(\phi) N_{A_1}(\phi) d\phi \tag{26}$$

III.1.2. Winding function theory for machines with salient air gaps

In basic winding function theory, the inverse gap function is assumed to be composed of only even harmonics. Fig. 26 shows the machine with a two-pole winding residing within the air gap. By Ampere's law, the line integral is taken around the conductor in the path 1-2-3-4-1 in (27). The MMF drops, $\Im$, are equivalent to the turns function of the winding, $n(\Phi)$, multiplied by the current, i, in the winding. As with regular WFT and the assumption of linear iron with a high relative permeability, the MMF drops through the back iron and rotor are negligible and can thus be ignored.

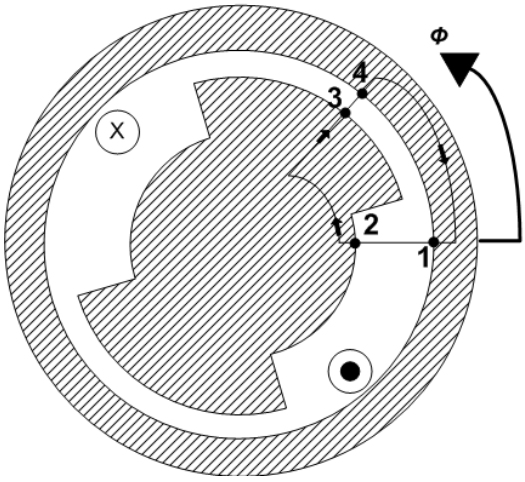

Fig. 26. An idealized machine with a salient rotor and conductors in the air gap.

$$\Im_{12} + \Im_{23} + \Im_{34} + \Im_{41} = n(\phi)i \tag{27}$$

Winding function theory is amended as done in [60] to include a salient air gap for the geometries studied here. An inverse gap function will be used to account for the changing gap thickness, in the same manner that the turns function accounts for the changing MMF throughout the machine. In (28), it is assumed that the average value of the MMF over the circumference of the machine is zero, when multiplied by an inverse gap function $g^{-1}(\Phi)$:

$$\int_0^{2\pi} \Im(\phi) g^{-1}(\phi) d\phi = 0 \ . \tag{28}$$

Following the assumptions associated with (29), the value for the MMF can be derived as follows:

$$\int_0^{2\pi} \left[\Im_{12}(0) + \Im_{34}(\phi)\right] g^{-1}(\phi) d\phi = \int_0^{2\pi} n(\phi) i g^{-1}(\phi) d\phi \, . \tag{29}$$

In [60], it was assumed that the salient air gap was composed solely of even harmonics, allowing for the simplification which resulted in regular WFT. However, in the case of the magnetic gear, the salient air gaps will not be limited to even harmonics. The salient air gap could be composed of odd or all harmonics. In [62] and [63], the inclusion of eccentricity led to the derivation and use of modified winding function theory (MWFT). However, eccentricity is not the only factor that necessitates the use of MWFT; the simple fact of using a salient air gap that is not built from even harmonics necessitates MWFT as well. The derivation continues with (30) to find the right MMF term in (29), assuming that the left MMF term is zero:

$$\begin{aligned} 2\pi\Im_{12}(0)\left\langle g^{-1}(\phi)\right\rangle &= \int_0^{2\pi} n(\phi) i g^{-1}(\phi) d\phi \\ \Im_{12}(0) &= \frac{1}{2\pi\left\langle g^{-1}(\phi)\right\rangle}\int_0^{2\pi} n(\phi) i g^{-1}(\phi) d\phi \\ \Im_{12}(0) + \Im_{34}(\phi) &= n(\phi) i \\ \Im_{34}(\phi) &= i\left[n(\phi) - \frac{1}{2\pi\left\langle g^{-1}(\phi)\right\rangle}\int_0^{2\pi} n(\phi) g^{-1}(\phi) d\phi \right] \end{aligned} \tag{30}$$

The term in brackets is the modified winding function, $M(\Phi)$. In (31) and (32), the modified winding function is shown as a new average value which must be subtracted from the turns function.

$$\left\langle M(\phi)\right\rangle = \frac{1}{2\pi\left\langle g^{-1}(\phi)\right\rangle}\int_0^{2\pi} n(\phi) g^{-1}(\phi) d\phi \tag{31}$$

$$M(\phi) = n(\phi) - \left\langle M(\phi)\right\rangle \tag{32}$$

Assuming two windings A and B, a radius *r*, and a stack length *l*, the new inductance values using the modified winding function are given in (33) for the mutual inductance and in (34) for the magnetizing inductance. The flux linkage λ_{AB} is the flux in winding A due to the current in winding B, while the flux linkage λ_{AA} is the flux in winding A due to its own current.

$$L_{AB} = \frac{\lambda_{AB}}{i_B} = \mu_0 rl \int_0^{2\pi} n_A(\phi) M_B(\phi) g^{-1}(\phi) d\phi \tag{33}$$

$$L_{AA} = \frac{\lambda_{AA}}{i_A} = \mu_0 rl \int_0^{2\pi} n_A(\phi) M_A(\phi) g^{-1}(\phi) d\phi \tag{34}$$

III.2. Winding Function Theory Applied to Magnetic Devices

Now that the need for MWFT has been presented, it will be applied to magnetic devices. The modeling of a magnetic gear must begin with the most fundamental component of the gear, the individual magnets themselves, first looked at in [64] and [65] in conjunction with FEA. In Fig. 27, a single magnet is shown with a magnetization vector which is parallel to its thickness. A coil wrapped around a material of equal permeability to that of the magnet will provide an equivalent magnetization vector, assuming sufficient current. The magnets used in this analysis have a thickness, l_m, of 2.5 mm and a remanent magnetism, B_r, of 1.21 T. The magnets on the inner rotor are stacked doubly compared to the outer rotor. Hence, the required MMF for one stack of magnets is:

$$\Im = H_m l_m = \frac{B_r l_m}{\mu_0 \mu_r} = \frac{1.21(0.0025)}{\left(4\pi * 10^{-7}\right)1.052} = 2288 At \tag{35}$$

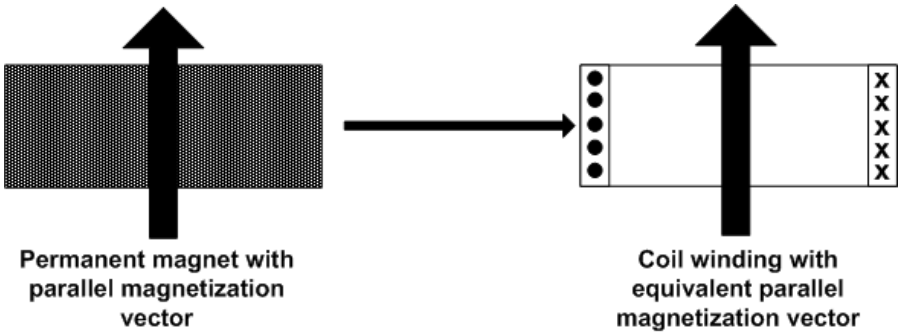

Fig. 27. Model of a permanent magnet with coils fed by DC current which produces an equivalent magnetization vector.

In the simplest case, surface-mounted magnets on a rotor lie adjacent to each other and form the basis for a single turns function, as visualized in Fig. 28. The adjacent magnets are simply modeled as coils which are wrapped in opposing directions adjacent to each other. They are fed equivalent DC current because magnets on the same rotor will all have the same thickness in the magnetic gear. These assumptions allow us to treat the adjacent magnets as though they are part of a single phase. The turns function reaches a magnitude of *2N* if each magnet has *N* windings. This is due to the fact that adjacent coil sides lie next to each other to create alternating magnetic flux vectors.

Fig. 29 displays an 8-pole rotor with surface-mount magnets modeled as coils. Assuming that the coil sides are infinitesimally narrow, the turns function resulting from the rotor is also shown in Fig. 29 as a square wave. Since the magnets have a full pitch, the resulting square wave is symmetric.

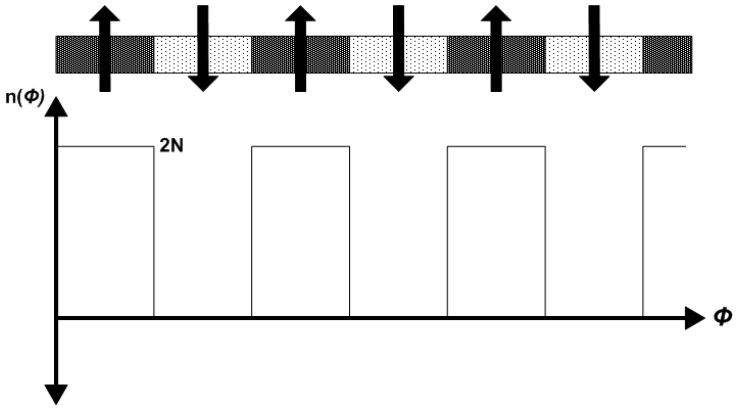

Fig. 28. Permanent magnets with alternating vectors form the basis for a single turns function over the circumference of the rotor.

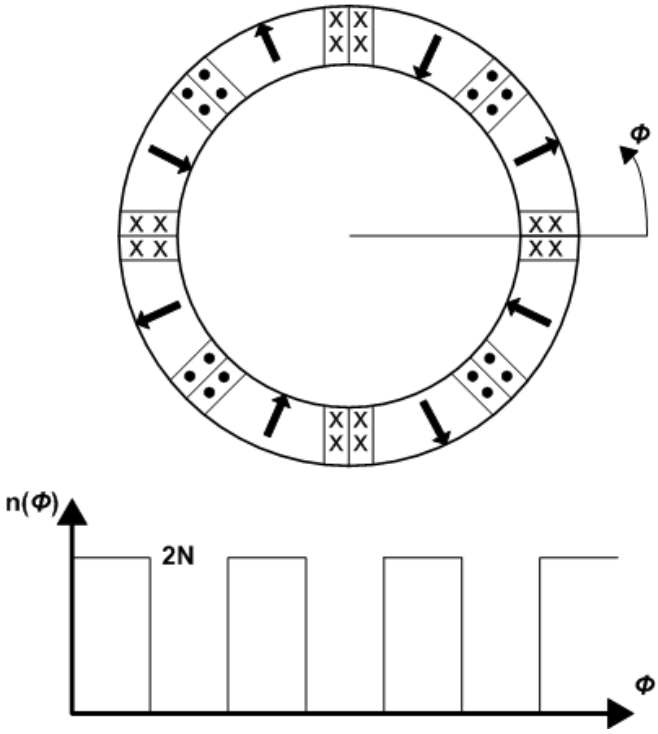

Fig. 29. An 8-pole rotor with infinitesimally narrow coil sides and its resulting turns function.

The turns functions for the windings in this study are built from Fourier series, given in (36) and shown in Fig. 30, which can be phase-shifted easily in simulations.

$$n(\phi) = \frac{d}{x} + \frac{2}{\pi}\sum_{h=1}^{\infty}\frac{(-1)^h}{h}\sin\frac{h\pi d}{x}\cos\frac{h\pi\phi}{x} \tag{36}$$

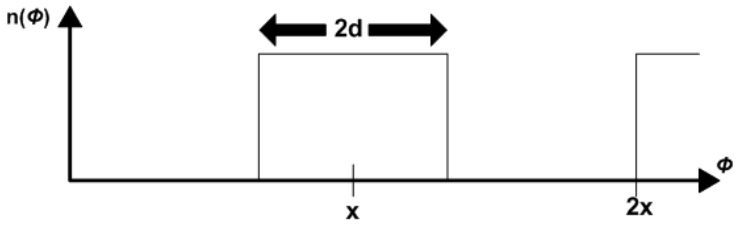

Fig. 30. The turns function modeled with the Fourier Series.

III.2.1. Verification of a single phase per rotor

The first assumption must be verified that the ring of magnets can be assumed to be a single phase, rather than as multiple phases. It will be done by looking at a simple case, shown in Fig. 31, in which an ideal four-pole machine is shown. The inductances will be calculated for the case in which the two coils, *A* and *B*, are treated as distinct coils, and ones which are connected in series.

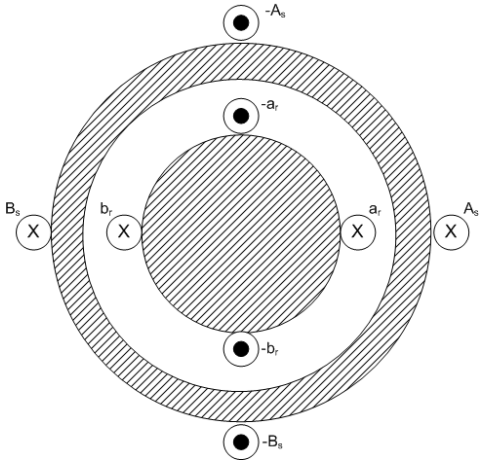

Fig. 31. An ideal four pole machine.

The turns functions and winding functions for the stator are shown in Fig. 32. The two phases *A* and *B* are assumed to have *N* windings. The average value is used to turn the turns function into the winding function. The average number is found in (37).

$$\langle n(\phi)\rangle = \frac{1}{2\pi}\int_0^{2\pi} n(\phi)d\phi = \frac{N}{4} \tag{37}$$

The self or magnetizing inductance is found in (38) for phase *A*.

$$L_{AA} = \frac{\mu_0 rl}{g}\int_0^{2\pi} N_A^2(\phi)d\phi = \frac{\mu_0 rl}{g}\left[\int_0^{\pi/2}\left(\frac{3N}{4}\right)^2 d\phi + \int_{\pi/2}^{2\pi}\left(\frac{-N}{4}\right)^2 d\phi\right] = \frac{\mu_0 rl}{g}\pi N^2\left(\frac{3}{8}\right) \tag{38}$$

Likewise, the mutual inductance is calculated in (39) between phases *A* and *B*.

$$L_{AB} = \frac{\mu_0 rl}{g}\int_0^{2\pi} N_A(\phi)n_B d\phi = \frac{\mu_0 rl}{g}\int_{\pi}^{3\pi/2}\left(\frac{-N}{4}\right)N d\phi = \frac{-\mu_0 rl}{g}\pi N^2\left(\frac{1}{8}\right) \tag{39}$$

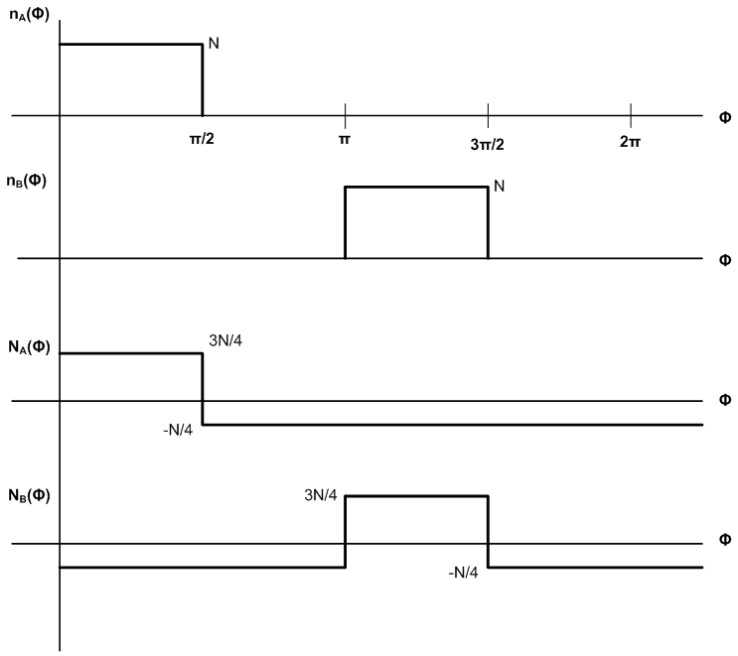

Fig. 32. Turns and winding functions for stator phases.

The total flux treating *A* and *B* as separate phases is given by (40). This assumes that the currents in the phases are equal, and that the mutual inductances are equivalent as well. Then the total inductance is computed in (41).

$$\lambda_s = L_{AA} i_A + L_{BB} i_B + L_{AB} i_A + L_{BA} i_B = 2L_{AA} i_A + 2L_{AB} i_A \tag{40}$$

$$L_s = \frac{\lambda_s}{i_s} = \frac{\mu_0 rl}{g} \pi N^2 \left(\frac{3}{8} + \frac{3}{8} - \frac{1}{8} - \frac{1}{8} \right) = \frac{\mu_0 rl}{g} \pi N^2 \left(\frac{1}{2} \right) \tag{41}$$

Now the inductance is calculated by treating the stator phases as a set of series connected coils, done in (42). It is apparent that the inductance is the same as that found in (41).

$$L_{AB} = \frac{4\mu_0 rl}{g} \int_0^{\pi/2} \frac{N^2}{4} d\phi = \frac{\mu_0 rl}{g} \pi N^2 \left(\frac{1}{2} \right) \tag{42}$$

III.2.2. Applying modified winding function theory to ideal machines

In transferring the proposed theory to the magnetic gear, MWFT will first be tested on four different machines to verify its ability to account for machines with unmatched pole numbers on the rotor and stator. These machines, shown in Fig. 33, represent the four combinations between a stator with either 2 or 4 poles, and a rotor with 2 or 4 poles. The ideal machine parameters are given in Table V. They are analyzed with FEA in order to provide a basis for the inductance calculation using MWFT. The coil sides are built as small as possible to mimic the assumptions taken in winding function theory. Linear iron is used to mimic the assumption that the MMF drop through the iron is negligible, i.e. saturation is not taken into account. In addition, the difference between

g_{min} and g_{max} is exaggerated to help reduce the effect of fringing flux in the FEA calculation.

Table V. Parameters for ideal machine simulations

Symbol	Quantity	Value
g_{min}	Minimum air gap thickness	0.8 mm
g_{max}	Maximum air gap thickness	45.6 mm
l	Stack length	26 mm
r_r	Rotor radius	51.9 mm
r_s	Stator outer radius	60 mm

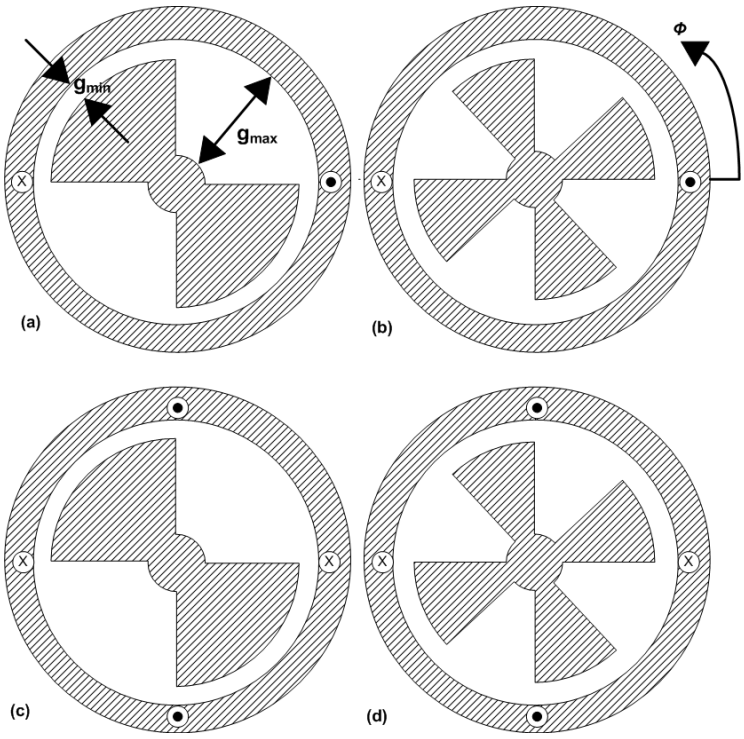

Fig. 33. Idealized machines built in MagNet showing combinations among 2 and 4 pole stator windings and 2 and 4 pole synchronous rotors, (a) machine 1, (b) machine 2, (c) machine 3, and (d) machine 4.

The flux linkages are calculated for each of the *h* coils in the four models, and a full rotation. The inductance is then calculated from the flux linkage for each coil, λ_k, produced from the FEA solver in (43). The inductances calculated from FEA for a full rotation of each of the machines is shown in Fig. 34. The models built are comprised of one turn per coil.

$$L = \frac{\lambda_{tot}}{i} = \left(\sum_{k=1}^{h} \lambda_k \right) / i \tag{43}$$

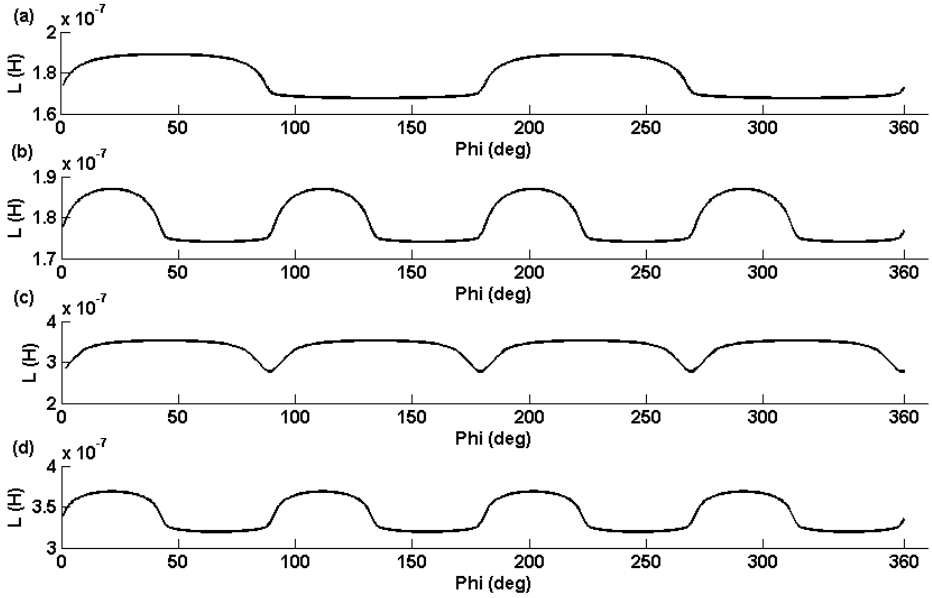

Fig. 34. Inductances calculated with FEA for (a) machine 1, (b) machine 2, (c) machine 3, and (d) machine 4.

The flowchart for using MWFT to calculate the inductance is shown in Fig. 35. The inductance calculations are run in Matlab/Simulink using a fixed time step solver. While the turns functions are built from Fourier series, the inverse gap functions are built from piecewise-linear functions in their exact form since they do not have to be shifted. The inverse gap function is shown in Fig. 36.

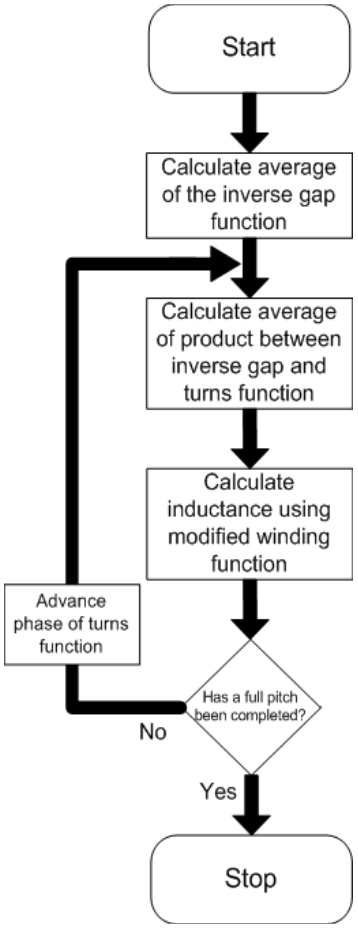

Fig. 35. Flowchart for calculated inductances using MWFT in Matlab/Simulink.

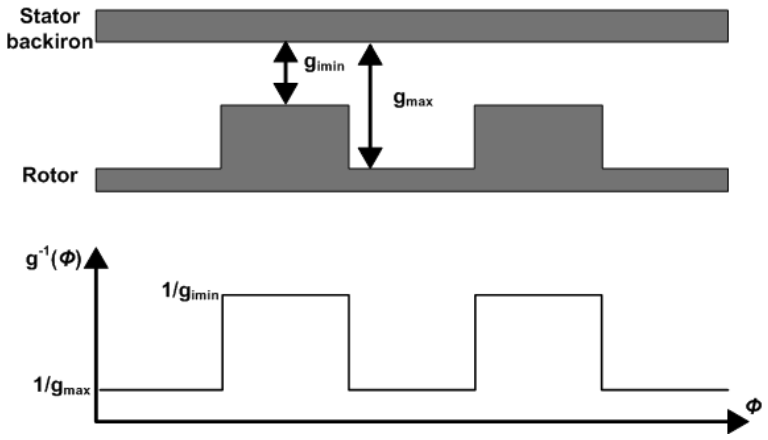

Fig. 36. Inverse gap function used for ideal machines in inductance calculations.

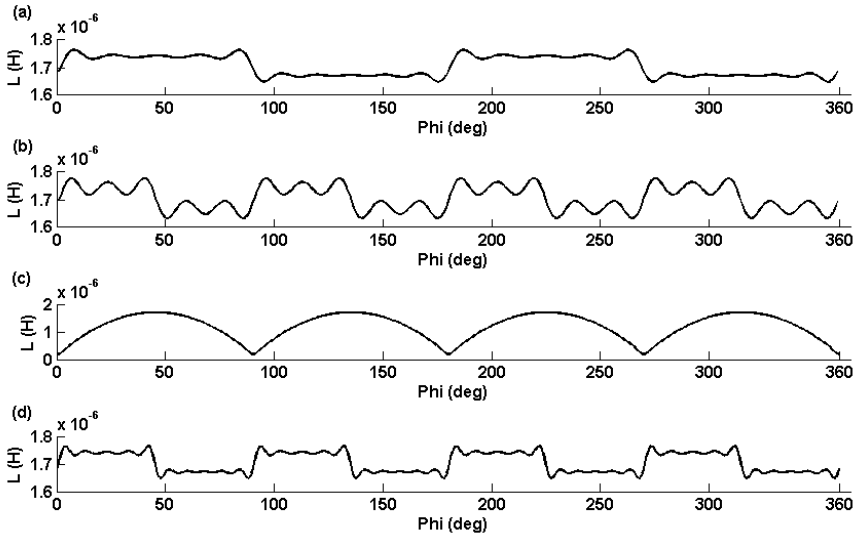

Fig. 37. Inductances calculated with MWFT for (a) machine 1, (b) machine 2, (c) machine 3, and (d) machine 4.

The results of using MWFT to calculate the inductance are shown in Fig. 37. Each of the machines reveals the correct fundamental frequency, with differences in magnitude coming from unavoidable added MMF drops in the back iron of the FEA simulations. In particular, the correct fundamental frequency of machine 3 could only be determined with MWFT.

III.2.3. Winding function theory applied to the magnetic coupling

The flux which links the two rotors in the magnetic gear serves as useful flux which will provide the torque-angle curves characteristic of magnetic gears and couplings. A magnetic coupling, essentially a 1:1 magnetic gear, will first be considered to verify the use of MWFT on purely magnetic devices [66]. Fig. 38a shows an 8-pole magnetic coupling with surface mounted magnets, the parameters of which are given in Table VI. The magnets are modeled as individual coils connected in series for each rotor, shown in

Fig. 38b. The coils are fed a DC current equivalent to twice that found in (35), due to the fact that the magnets are 5 mm thick, and rotated one pole pair pitch.

Table VI. Parameters for 8-pole coupling

Quantity	Value (mm)
Outer radius of outer rotor	60
Outer radius of inner rotor	46.3
Stack length	26
Shaft radius	17
Magnet thickness on either rotor	5
Air gap	1

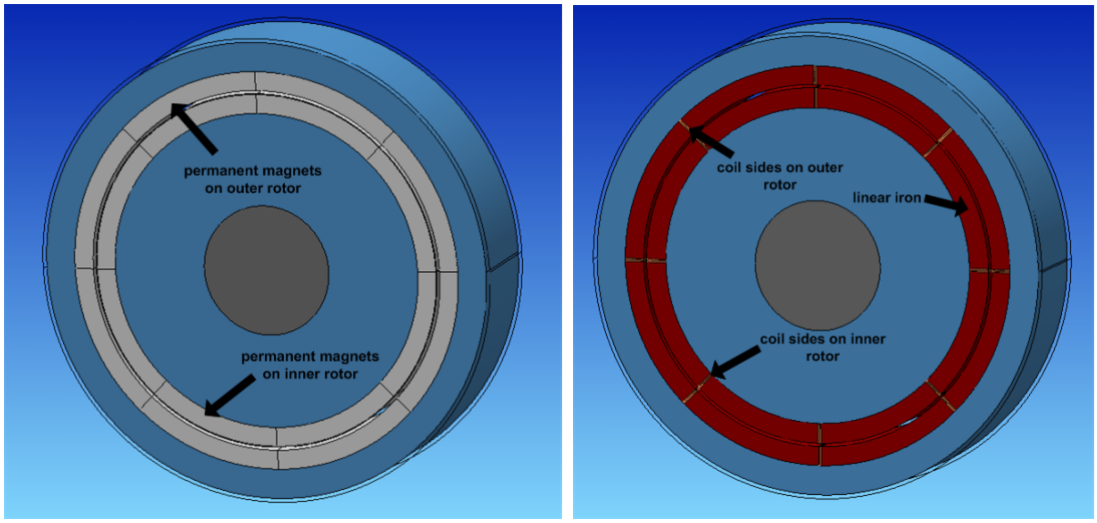

(a) (b)

Fig. 38. 8-pole radial magnetic coupling with (a) permanent magnets and (b) coils.

Using a model with coils, the flux linkage is collected over a pole-pair rotation and used to calculate the mutual inductance of the inner rotor due to the current in the outer rotor, L_{io}, using (43). L_{io} is shown in Fig. 39, which is equivalent to the inductance of the outer rotor due to the current in the inner rotor, L_{oi}.

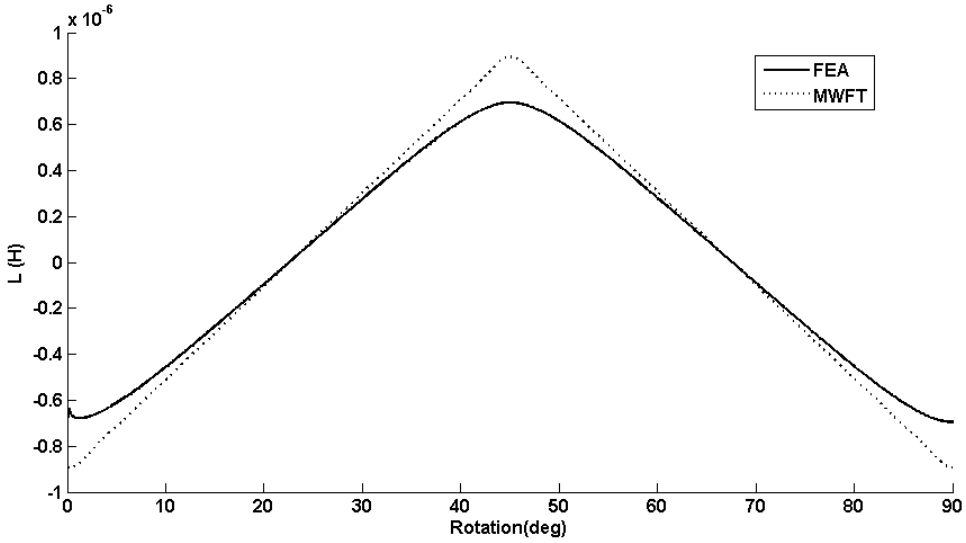

Fig. 39. Mutual inductance of inner rotor calculated with FEA and MWFT.

The mutual inductance calculated with MWFT agrees well with that from FEA. The difference in the peak value is due to the fact that the MMF described by the turns function drops off steeply between magnets. By contrast the MMF seen by FEA would have a shoulder which tapers off between adjacent magnets.

III.2.4. Winding function theory applied to the concentric planetary magnetic gear

Before modeling the entire magnetic gear with winding function theory, the gear will be separated into its two rotors to see how winding function theory can describe the rotors by themselves. Physically, this would represent the magnetic rotor facing stator teeth with the same pitch as the pole pieces, assuming there is a back-iron to the stator. It is also assumed that the rotors have surface-mount magnets. The inductances are again calculated from FEA for comparison.

The models used for the calculation are shown in Fig. 40. Each magnet is built as an individual coil with an infinitesimally narrow coil side. Each of the *h* coils will provide a

flux linkage to calculate the inductance, using (43). The spaces between the coil sides are built with linear iron as well, but with a relative permeability equal to that of the magnet. The back-iron is composed of linear iron with a relative permeability of 10,000. The inverse gap function is built in the same manner as the ideal machines in Fig. 33.

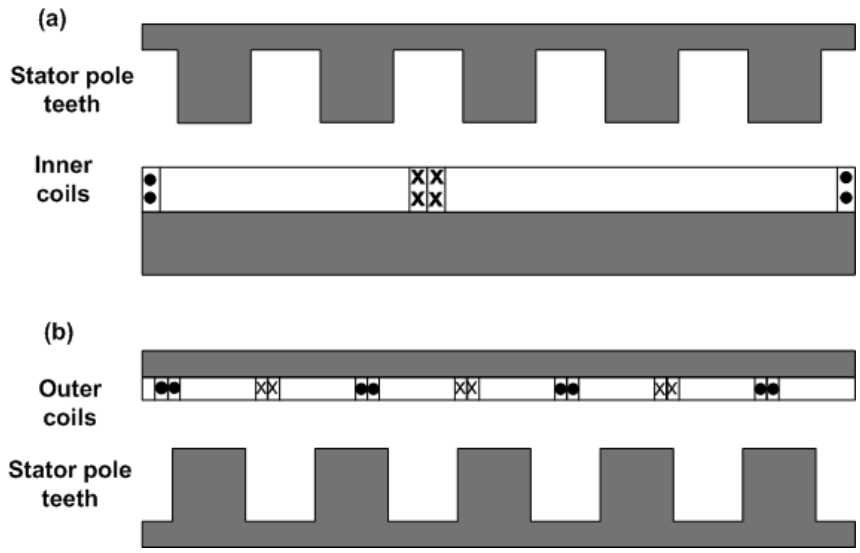

Fig. 40. Linear sections of magnetizing inductance calculations for (a) inner rotor and (b) outer rotor.

The inductances calculated from FEA are shown in Fig. 41. The inner and outer rotors are rotated a complete pole pair pitch. The inductances calculated from MWFT are shown in Fig. 42.

After performing an FFT of the magnetizing inductance for the outer rotor, the apparent differences of the two waveforms are better understood. MWFT gives a fundamental frequency equal to the number of pole pairs, 22, along with added harmonics which are multiples of 22. A prominent harmonics exists which is equal to the number of pole pairs multiplied by the number of stator pieces, 572. FEA on the other

hand gives a fundamental frequency equal to the number of poles, 44. FEA also shows prominent harmonics which are even multiples of 44.

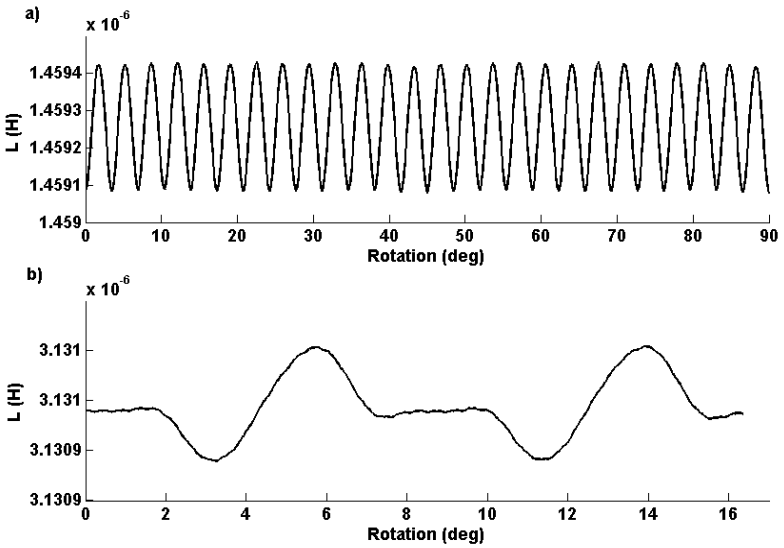

Fig. 41. Magnetizing inductances calculated with FEA for (a) inner rotor and (b) outer rotor.

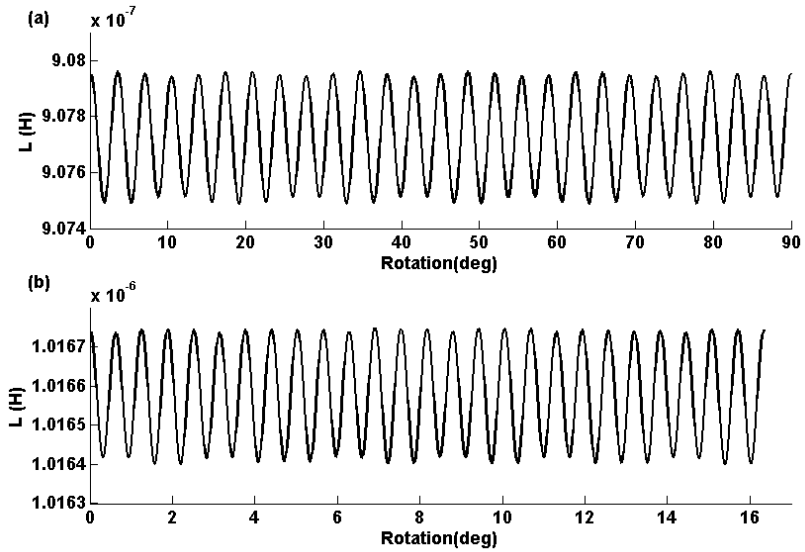

Fig. 42. Magnetizing inductances calculated with MWFT for (a) inner rotor and (b) outer rotor.

The differences in the harmonic content are due to the difference in which MWFT handles flux paths compared to FEA, shown in Fig. 43. The fringing flux in FEA has a damping effect upon the inductance waveform and thus the fundamental frequency is dominated by the number of stator pole teeth in the model. The combination of pole pairs to slots (i.e. teeth in the case of magnetizing inductance) in the gear studied also matches a combination presented in [67] for a machine which is incapable of generating strong high frequency components. In this special combination, the physical system, as well as that calculated by FEA, will mask higher slot harmonics than those calculated with MWFT.

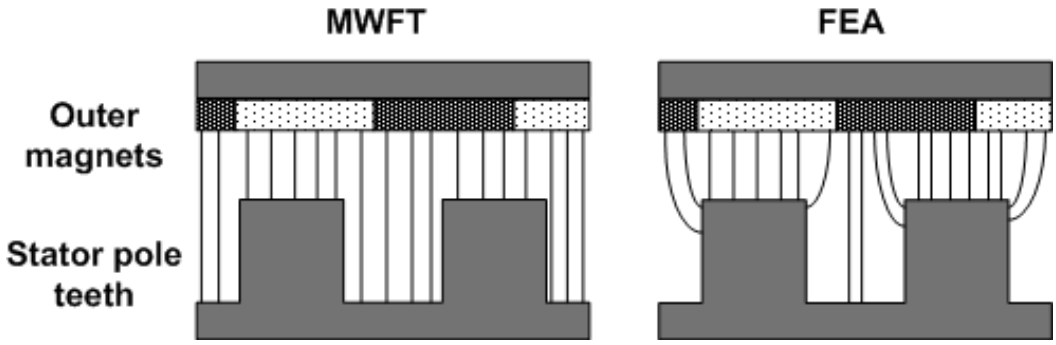

Fig. 43. Difference in flux paths with MWFT and FEA.

The magnetic gear is now built by replacing all of the magnets with coils. This will provide the flux linkage for the cases of mutual inductance. The inverse gap function is built as shown in Fig. 44. The mutual inductance term L_{io} is shown in Fig. 45a ('*i*' for inner and '*o*' for outer rotors). This corresponds to the flux linkage in the inner windings due to the current in the outer windings. The inner rotor is rotated while the outer rotor is fixed. The mutual inductance term L_{oi} is shown in Fig. 45b. This corresponds to the

flux linkage in the outer winding due to current in the inner windings. The outer rotor is rotated while the inner rotor is fixed.

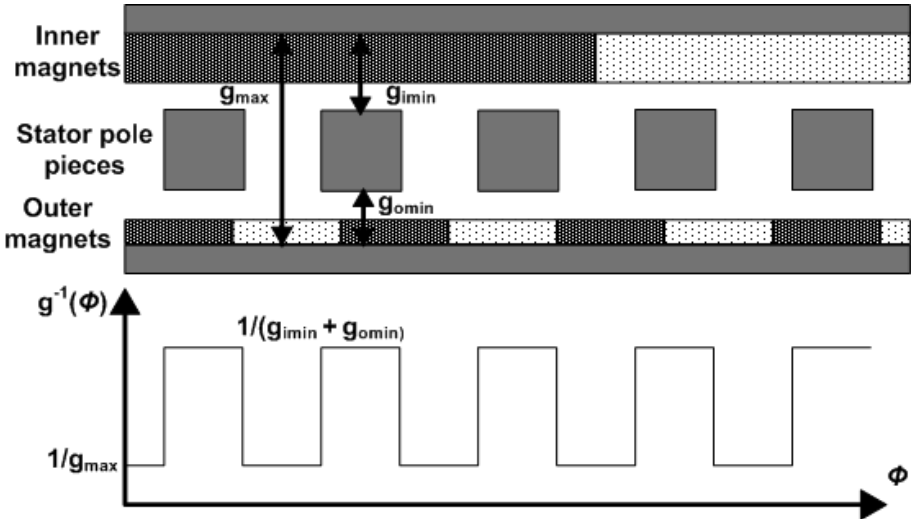

Fig. 44. Inverse gap function used for mutual inductance calculations.

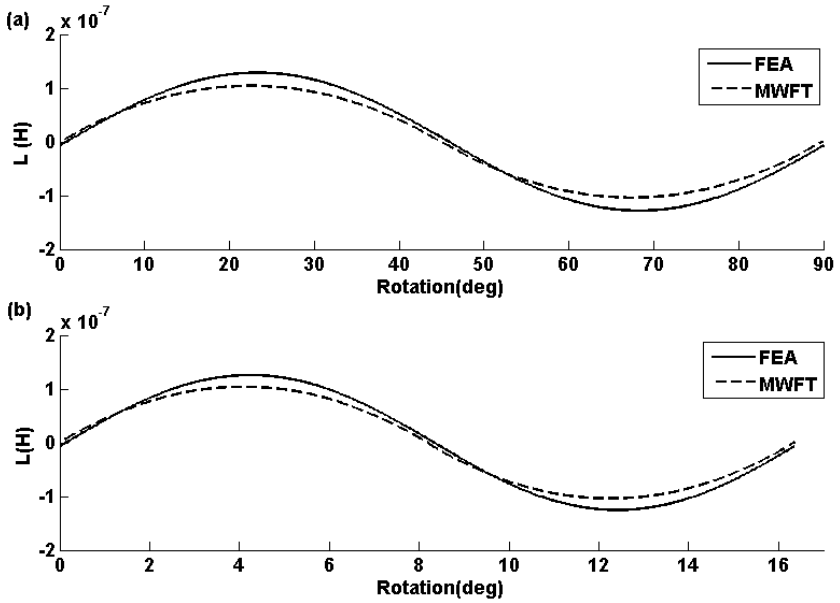

Fig. 45. Mutual inductances calculated by MWFT and FEA for (a) the inner rotor and (b) the outer rotor.

As can be seen in the figures, the results for the mutual inductances agree very well, with the differences in magnitude coming from a difference in the air gap with FEA compared to MWFT.

III.2.5. Torque calculated from inductance

In finding the torque for the gear, FEA will once again be used as a basis for comparison. In this section, the viability of replacing magnets with coils is investigated. Fig. 46 shows the FEA calculated torque with an ideal magnetic gear built from permanent magnets and with coils. The torque waveforms shown in Fig. 46 reveal an operating point for the magnets which is less than the remanent magnetization used in (35). The operating point for conventional permanent magnet machines is below the remanent magnetization. This is due to the demagnetization from the stator field, as well as the excitation requirement of the air gap [68]. This reduction however comes only due to the excitation requirement for the air gap in the magnetic gear. Adjusting for the operating point, the MMF for the magnets used in the inductance calculations is 2151 ampere-turns.

Torque is generated in the magnetic gear by the interaction of the magnetic rings with each other and the stator pole pieces. This can be calculated by looking at the changing reluctance in the gear, which is illustrated in Fig. 47. This changing reluctance, $\Re$, is represented in (44) and (45) as either unaligned, u, or aligned, a.

$$\Re_u = \frac{l_u}{\mu_0 A_u} \tag{44}$$

$$\Re_a = \frac{l_a}{\mu_0 A_a} \tag{45}$$

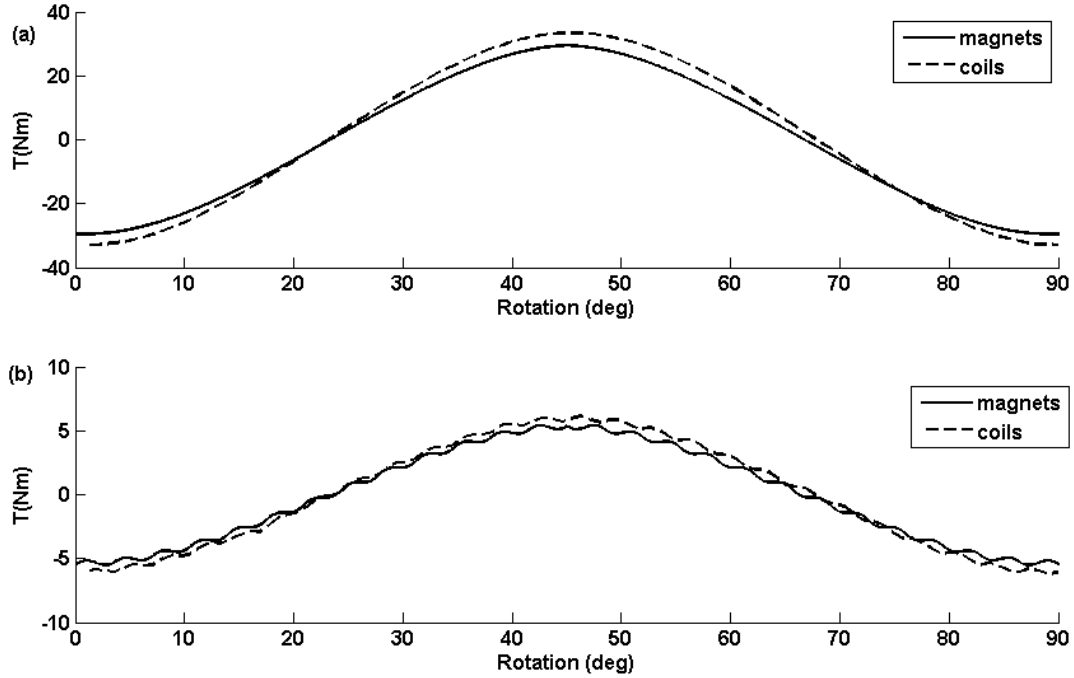

Fig. 46. Validity of replacing magnets with coils shown over a pole pair pitch showing torque curves for the (a) outer rotor and (b) inner rotor.

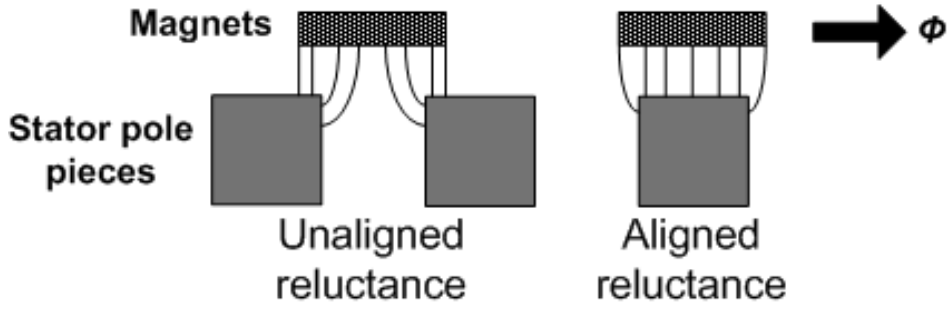

Fig. 47. Changing reluctance as magnets move over pole pieces.

The changing reluctance translates into a change in inductance, and thus a change in energy, as shown by the distinct energy values in (46) and (47). This is also known as

the coenergy, W_{co}, shown in matrix form in (48) as a function of the four inductances for the magnetic gear.

$$E_u = \frac{1}{2} L_u i^2 \tag{46}$$

$$E_a = \frac{1}{2} L_a i^2 \tag{47}$$

$$W_{co} = \frac{1}{2} \begin{bmatrix} i_i & i_o \end{bmatrix} \begin{bmatrix} L_{ii} & L_{io} \\ L_{oi} & L_{oo} \end{bmatrix} \begin{bmatrix} i_i \\ i_o \end{bmatrix} \tag{48}$$

Using these, the torque is found in (49), and expanded into (50) and (51). The first two terms represent the cogging torque of the respective rotors, and the last two terms represent mutual inductances, which reveal the torque transfer in the gear (Φ_o for outer rotor rotation and Φ_i for inner rotor rotation).

$$T = \left[\frac{\partial W_{co}}{\partial \phi} \right]_{I_{const.}} \tag{49}$$

$$T_i = \frac{1}{2} \left[I_i \frac{dL_{ii}}{d\phi_i} I_i + I_o \frac{dL_{oo}}{d\phi_i} I_o + I_i \frac{dL_{io}}{d\phi_i} I_o + I_o \frac{dL_{io}}{d\phi_i} I_i \right] \tag{50}$$

$$T_o = \frac{1}{2} \left[I_i \frac{dL_{ii}}{d\phi_o} I_i + I_o \frac{dL_{oo}}{d\phi_o} I_o + I_i \frac{dL_{oi}}{d\phi_o} I_o + I_o \frac{dL_{oi}}{d\phi_o} I_i \right] \tag{51}$$

The torque equations can be reduced to (52) and (53), noting that the terms containing mutual inductance are nominally equivalent, and the terms containing magnetizing inductance of the opposite rotors are null due to the fact that they are not rotated.

$$T_i = \frac{1}{2} I_i^2 \frac{dL_{ii}}{d\phi_i} + I_i I_o \frac{dL_{io}}{d\phi_i} \tag{52}$$

$$T_o = \frac{1}{2} I_o^2 \frac{dL_{oo}}{d\phi_o} + I_o I_i \frac{dL_{oi}}{d\phi_o} \tag{53}$$

Using (52) and the inductance calculated in Fig. 39, the torque of the inner rotor of the magnetic coupling is shown in Fig. 48. The torque waveforms are in good agreement, with the differences coming from the MMF taper between adjacent magnets seen in the inductance calculations. The absence of the stator pole pieces in the magnetic coupling yields a constant air gap, and thus no cogging torque.

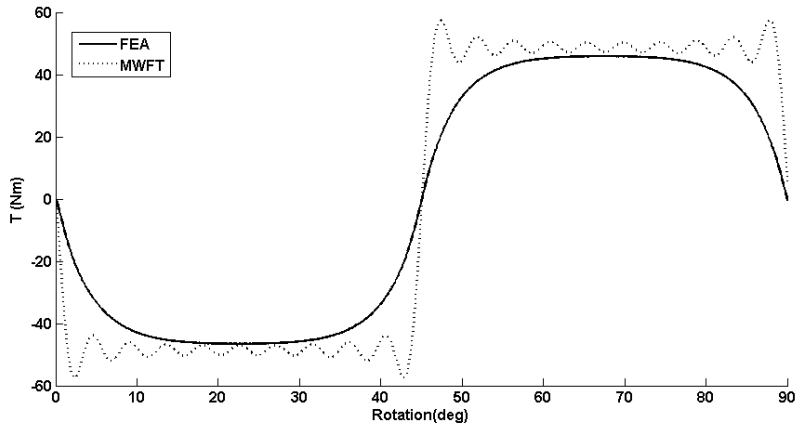

Fig. 48. Torque of inner rotor of magnetic coupling calculated with FEA and MWFT.

As for the concentric planetary magnetic gear, the torques are calculated and shown in Fig. 49, using the values of current adjusted for the operating point of the magnets. The magnitude of the torque ripple on the inner and outer rotors is close to one another. The frequency component of the torque ripple is also the same. The stall torque for the outer rotor is 27 Nm with MWFT, compared to 29.5 Nm with FEA.

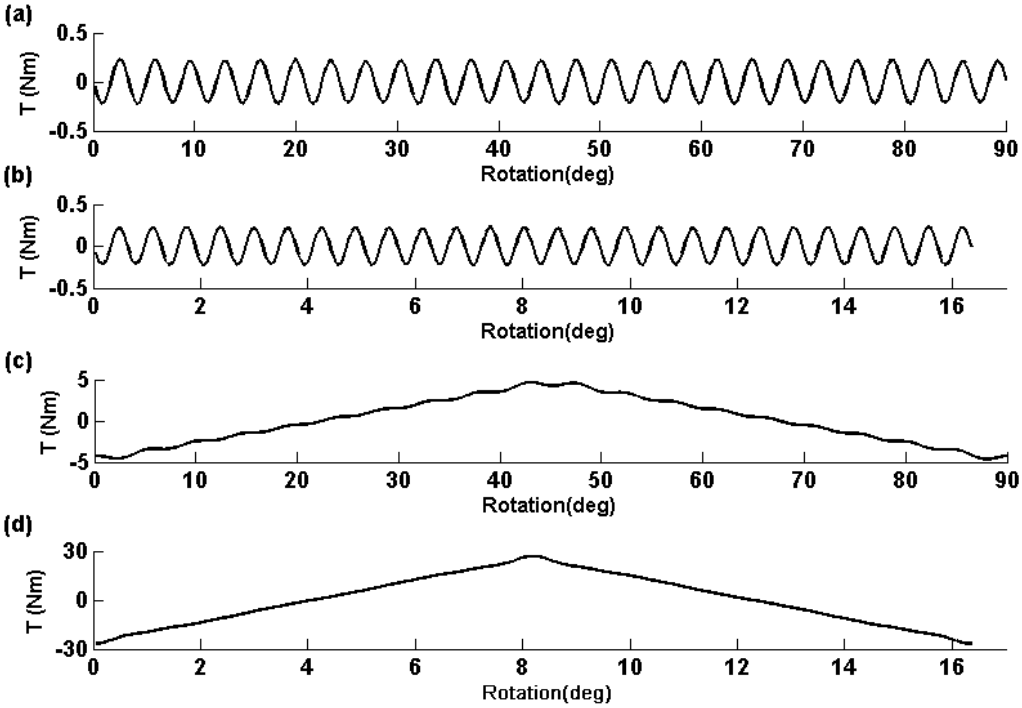

Fig. 49. Torques calculated with MWFT for (a) inner rotor cogging torque, (b) outer rotor cogging torque, (c) inner rotor stall torque, and (d) outer rotor stall torque.

III.3. Conclusion

The alternative MWFT analysis is a good approach to analyzing the magnetic gear because of the reduced computational burden. The analysis for magnetic gears has been undertaken previously using calculation of the Maxwell stress tensor with Fourier series as well as Finite Element Analysis. While FEA yields results which are generally accurate and need only to be scaled due to 3D end effects, its setup is lengthy and study of variations can be quite tedious depending upon the solver type and fidelity of the model. The use of MWFT, which had primarily been used on electric machines that did not utilize permanent magnets, is a novel idea and can be applied to magnetic gears, as well as other types of permanent magnet machines in the future.

IV. DAMPER WINDINGS FOR THE MAGNETIC GEAR

IV.1. The History of Damper Windings

The idea of damper windings is closely tied to synchronous generators. Damper, or armotisseure, windings were added to the synchronous rotor in order to kill transient oscillations caused by the load in [69]-[71]. More recently, damper windings have been added to synchronous machines with permanent magnets [72]-[77]. These special types of machines are referred to as line-start permanent magnet machines. The machine is designed to start as an induction machine, i.e. as an asynchronous machine. The permanent magnets actually detract from the performance of the machine during start-up, since they provide a braking torque. Once the machine reaches synchronous speed, the torque is provided by the permanent magnets and currents are no longer induced in the rotor bars. In the case of a change in speed or load, current will be induced in the rotor bars once again and arrest transient oscillations quicker than a conventional permanent magnet machine. These types of machines have also been investigated for their use in grid-connected synchronous generators [78][79].

It is here that the idea for adding damper windings to the magnetic gear is taken. Magnetic gears, while enjoying multiple advantages over conventional mechanical gears, are not as torsionally stiff [5]. Magnetic gears can be described by a stiffness constant, K, measured in Nm/rad. This is equal to the slope of the stall torque curve for the gear at the origin [66]. Gears undergoing changes in speed or load will experience oscillations due to their relatively low stiffness, as shown in [6].

IV.2. Design and Placement of the Damper Windings

Before beginning with the transient analysis, four magnetic gears with three base designs for the inner rotor are presented in Fig. 50. In [76], it was found that the interior permanent magnet configuration yielded a higher efficiency than surface type magnets with damper windings. The first one borrows from synchronous machine design, using a salient pole design to limit leakage flux between adjacent magnets. The second design uses the spoke design presented in [5]. The third and fourth designs use the interior permanent magnet (IPM) configuration used in [80]. All of these designs are modified to include damper windings, shown in red. The parameters common to all the designs are given in Table VII.

Table VII. Parameters common to all designs

Quantity	Value
Outer radius of outer rotor	60 mm
Outer radius of stator pole pieces	51.9 mm
Inner radius of stator pole pieces	47.1 mm
Outer radius of inner rotor	46.3 mm
Shaft radius	17 mm
Magnet thickness on outer rotor	2.5 mm
Magnet dimensions per pole on inner rotor	5 x 28 mm
Back iron and stator pole material	M19
Duty cycle of stator pole pieces	0.5
Inner rotor pole pairs	4
Outer rotor pole pairs	22

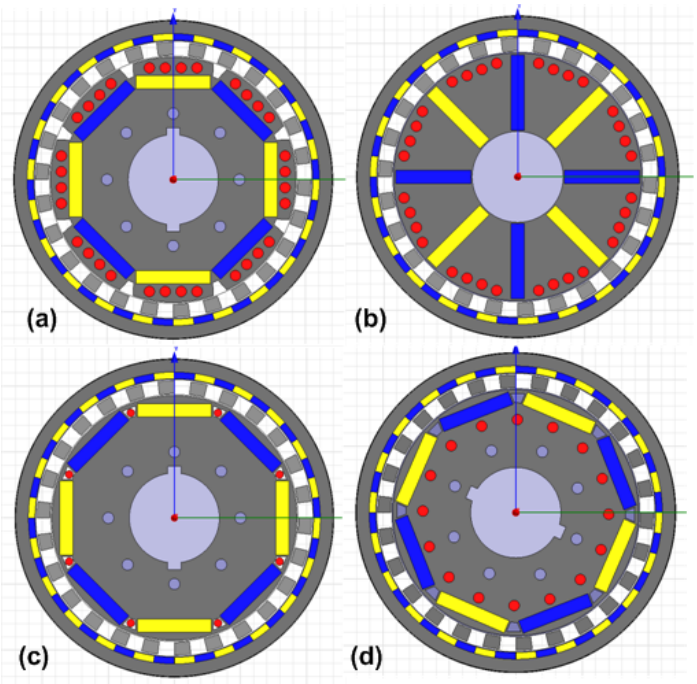

Fig. 50. Base designs with damper windings included for (a) salient pole design, (b) spoke design, (c) IPM design with damper bars in the flux barriers, and (d) IPM design with damper bars behind the magnets.

IV.3. Testing the Effectiveness of the Designs

IV.3.1. The value of the spring constant

One of the key parameters in studying the transient performance of the gear is its torsional stiffness. Compared to a mechanical gear, the torsional stiffness of a magnetic gear can be much lower [5][66]. In measuring the torsional stiffness of the magnetic gear, the torque transfer curve is linearized about the origin, shown in Fig. 51 for the salient pole design. For the salient pole design, K is approximated to be 12.75 Nm/rad.

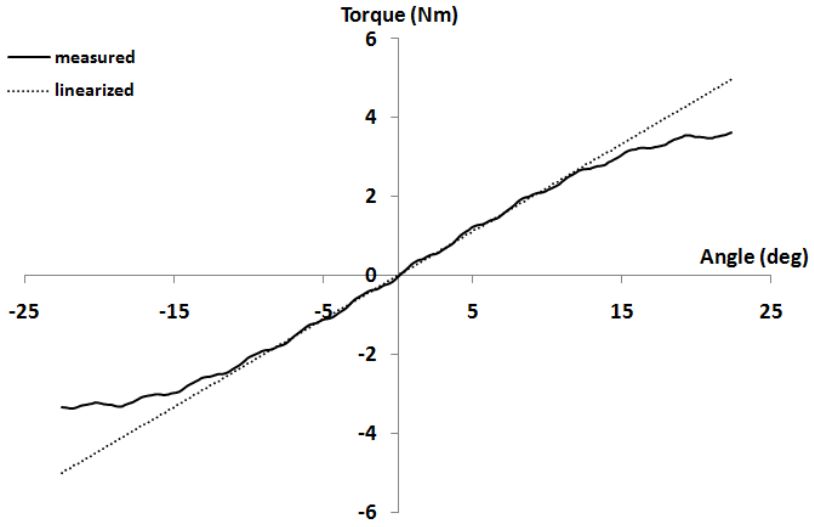

Fig. 51. Value of spring constant *K* shown linearized about the origin for the salient pole design.

In the gear designs, the settling time will be measured by pulling the rotor in question to just below its stall point, and then releasing it, shown in Fig. 52 for the salient pole design with and without damper windings. The settling time will be defined as the time it takes for the gear to reach 1% of its final resting position. The settling time for the base designs are given in Table VIII. For a second order system, the settling time t_s is given by:

$$t_s = \frac{4.6}{\xi \omega_n}, \tag{54}$$

where ζ is the damping ratio, and ω_n is the undamped natural frequency [81]. This undamped natural frequency is approximated in [6] by:

$$\omega_n = \sqrt{\frac{K}{J}}, \tag{55}$$

where J is the inertia of the rotor. The inertia is held to .0012 kgm^2 for the duration of the study to focus solely upon the effect of the damper windings. The oscillation dynamics of the gear, with one rotor fixed, are a dual to the linear oscillations of a spring mass damper system, given by the second order differential equation in (56). However, the linear distance x is replaced by the oscillation angle θ, and the mass m is replaced by the inertia J.

$$\frac{d^2\theta}{dt^2} + 2\xi\omega_n \frac{d\theta}{dt} + \omega_n^2\theta = 0 \tag{56}$$

The damping ratio is thus given by:

$$\xi = \frac{B}{2\sqrt{KJ}}, \tag{57}$$

where B is the viscous damping coefficient, held nominally at 0.001 Nms/rad for the designs without damper windings. This coefficient damps the oscillations after a relatively lengthy time in Fig. 52a. The addition of damper windings in Fig. 52b has damped the oscillations much quicker, corresponding to a 6-fold increase in B.

Table VIII. Settling times for base designs and base designs with damper windings

Design	Settling time (s)
Salient pole	7.745
Spoke	8.133
IPM	7.5
Salient pole with 4 damper bars per pole	1.262
Spoke with damper bars	6.461
IPM with damper bars in flux barriers	4.942
IPM with damper bars behind magnets	7.412

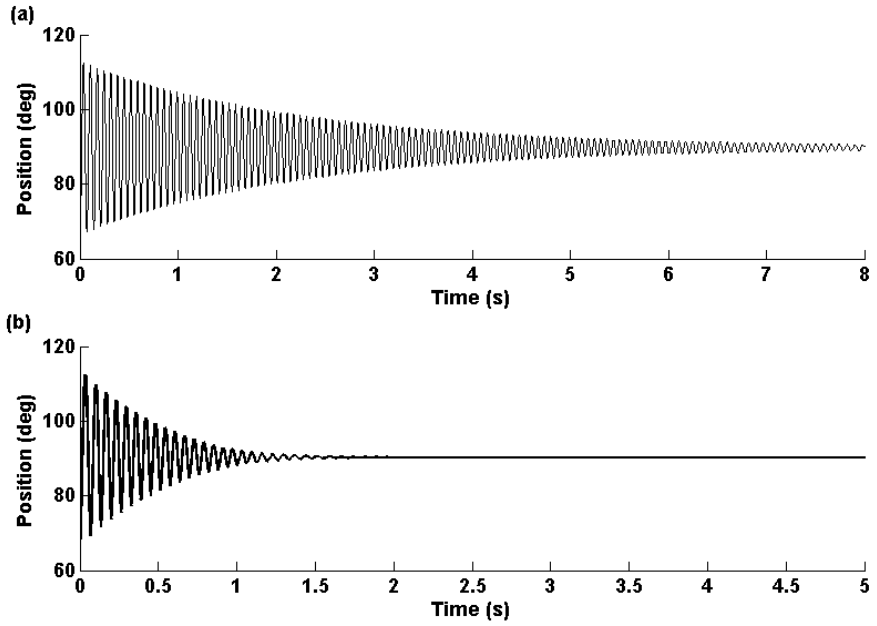

Fig. 52. Comparison of settling times between (a) salient pole design and (b) salient pole design with damper windings.

IV.3.2. Parameters for the damper windings

In designing the damper windings, a few variations must be taken into consideration. The most apparent variation is the number of bars to place on the rotor and their resistance. The resistance will be a property of the length, which is fixed in the case of this study, the length of the stack plus the length to connect to the end rings. It is also a function of the area of the bar and the material. The bars in this study will be fixed to a purely cylindrical shape and made of copper. In [69] it was found that minimizing the rotor copper losses, i.e. keeping the resistance of the cage low, increased the ability of the rotor to synchronize. In [78] and [79] it was also found that resistance was a key factor in the ability of the damper windings to successfully suppress transient

oscillations. In these and other cases, keeping the resistance low allows for higher induced currents in the damper cage and thus a higher damping torque generated by the cage.

The other variation which is not so apparent is whether or not the damper cage is interrupted. In the salient pole design, bars on the poles may form their own damper cage without being connected to other pole cages. This will be investigated for its effect upon the transient performance, along with the diameter of the bars, i.e. their resistance. The end rings themselves, are also given a resistance and inductance in the FEA simulation.

The performances of the base designs with the addition of damper windings are given in Table VIII in comparison to the base designs without damper windings. For a nominal value of 1μΩ and 1nH between adjacent conductors for the end ring, a bar diameter of 2 mm, and an uninterrupted cage, the salient pole design shows an 84% reduction in settling time compared to the base design. The spoke design with damper windings shows a 20% reduction in the settling time compared to the base design. The IPM design with bars (limited to a diameter of 1.5 mm) inside the flux barriers shows a 34% reduction settling, while the design with bars behind the magnets shows almost no reduction in settling time. Due to the maximum effectiveness of the salient pole design in reducing oscillations, it is the only design which will be investigated further.

IV.3.3. Transient performance with respect to number of bars

With the salient pole design, the number of bars per pole is varied between 3 and 4. With the nominal values used to compare the effectiveness of adding damper windings

to the base designs, the settling time with an even number of bars on each pole is 1.262 s, while an odd number of bars gives a settling time of 1.596 s.

The difference in performance can be better understood by examining the flux linkage in the individual bars. In [60], the d-axis flux linkage between two bars, *n* and *n'*, in a synchronous machine with damper windings was given by:

$$\Phi_{n,n'} = \frac{\mu_0 r l}{g_{\min}} N_{s1} I_s \sin \omega_e t \sin\left[\frac{(2n-1)\gamma}{2}\right], \tag{58}$$

where N_{s1} is the number of stator turns of the fundamental components of the winding functions for the three stator phases, g_{min} is the minimum air gap thickness, and I_S is the maximum amplitude of the sinusoidal phase current. Shown in Fig. 53, the angle γ separates each bar.

However, in the magnetic gear, the stator windings are replaced by the MMF due to the magnets. The factor in brackets gives an indication of the amount of flux linking the different bar pairs. The factor in brackets in (58) suggests that bars on the outside will see more flux linkage than bars on the interior. Indeed, this is shown with the FEA in Fig. 54, where bars on the interior see less flux linkage. Thus, a higher number of bars spread out across the pole will be able to provide a better damping action than a lower number of bars, given identical parameters such as diameter.

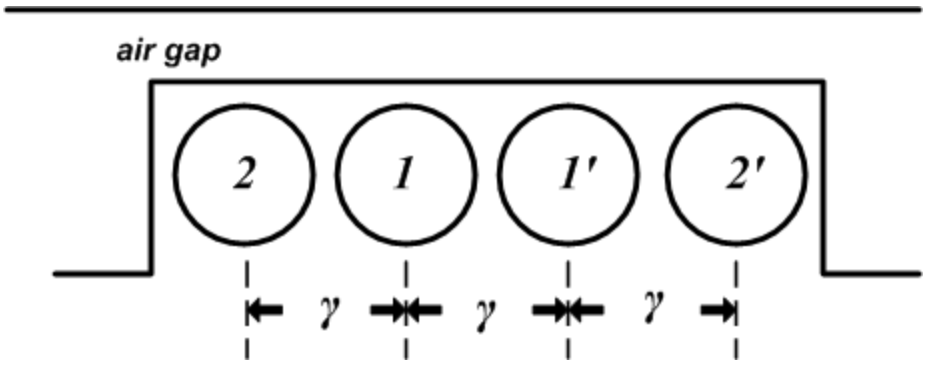

Fig. 53. Bar arrangement for 4 bars in one pole of the magnetic gear.

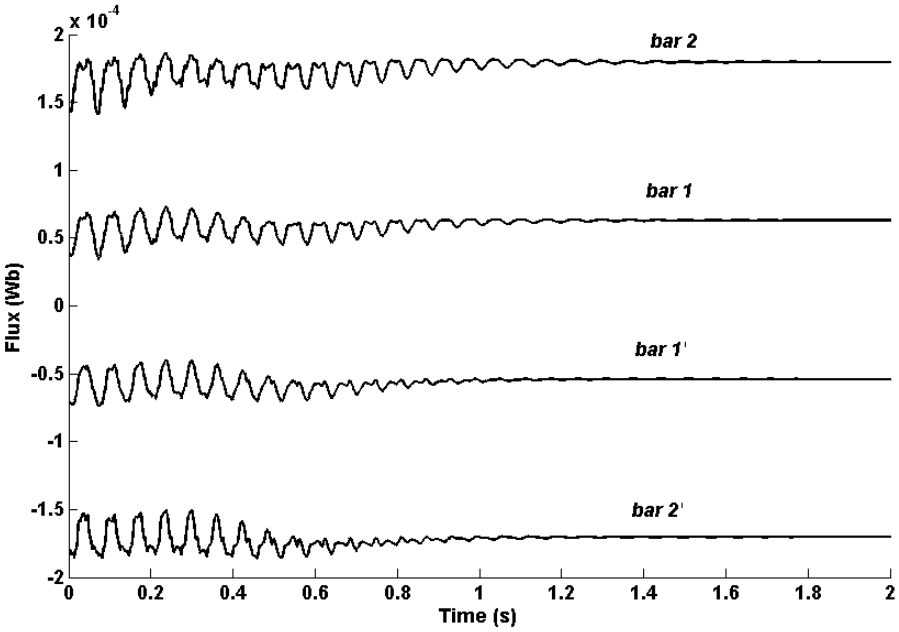

Fig. 54. Flux linkage in the salient pole design with 4 bars per pole as it settles to equilibrium.

However, there remains a practical limit to the number of bars which can be placed on each pole. In addition, the bars obstruct the path of the flux needed to provide useful torque transfer for the magnetic gear, since the copper bars have a relative permeability almost equal to air.

IV.3.4. Transient performance with respect to interrupted and uninterrupted cage

Using the settling times calculated for an uninterrupted cage, the designs with even and odd numbers of bars per pole are simulated with interrupted cages. Thus, each set of bars per pole constitutes its own damper cage. For the design with 4 bars per pole, a settling time of 3.153 s is calculated. For the design with 3 bars per pole, a settling time of 3.132 s is calculated. For both designs, the results show a settling time at least 1.5 s greater than the design with an uninterrupted cage.

In the case of having a continuous cage, the induced currents, both in the end rings and in the bars, are higher than for the case of the interrupted cage. From the results obtained with both designs, having an interrupted cage provides no discernible advantage in performance or construction, and will not be considered for the rest of this study.

IV.3.5. Transient performance with respect to bar radius

With a simple cylindrical shape, the resistance of an individual bar is given by (59). As stated earlier, the stack length l is fixed in this study, at 26 mm. With an approximate overhang of 1 mm for each side before attaching to an end ring, and for a conductivity of 1.72×10^{-8} Ωm for copper, a bar with a 2 mm radius has a resistance of 38.3 μΩ.

$$R = \frac{\rho l}{A} \tag{59}$$

The transient performance as the radius of the damper bars increases from 0.5 mm to 2 mm is shown in Fig. 55 for both 3 and 4 bars per pole. The performance shows that the gear becomes stiffer and settling time decreases as the radius increases. In both

designs, a practical limit is reached around the maximum of 2 mm. As with the number of bars, the radius of each bar also obstructs the path of the useful flux needed for the magnetic gear.

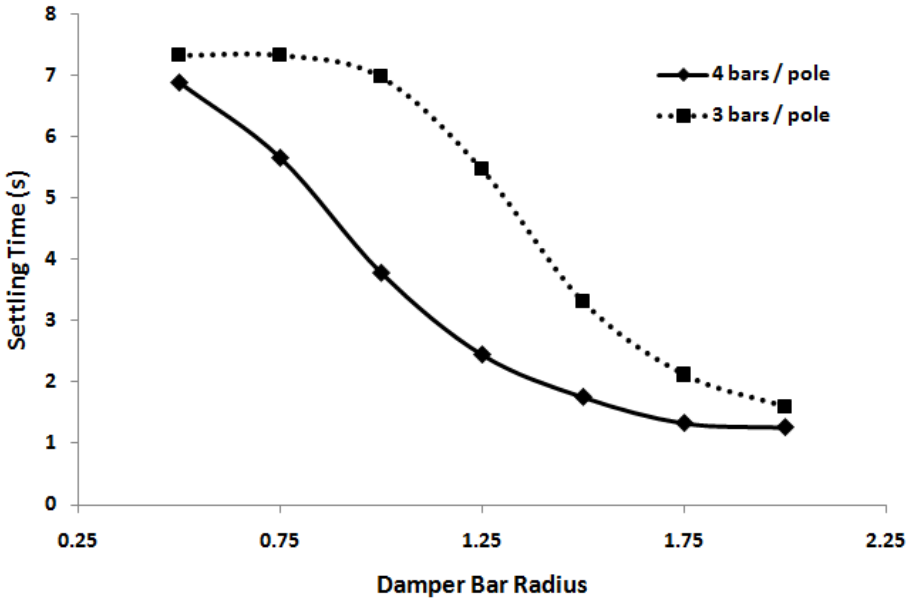

Fig. 55. Effect of damper bar radius on settling time.

IV.3.6. Transient performance with respect to end ring resistance

As the radius of the damper bars changes the resistance, so can the thickness of the end rings also change the resistance between adjacent conductors. A nominal value of 1 μΩ has been used thus far. For the case of 4 bars per pole, with an end ring that has a radial thickness of 8 mm, and an average length of 8.3 mm between adjacent conductors, this would dictate an end ring which has an approximate 17 mm axial thickness. The end ring resistance is varied from 1 to 10 μΩ, corresponding to a thickness of 17 to 1.5 mm. The settling time is shown for the designs with 3 and 4 bars per pole in Fig. 56. It is clear

that the settling time has a direct variation with the resistance, with the case of 4 bars per pole giving a better performance at lower resistances. The performances converge at higher resistances.

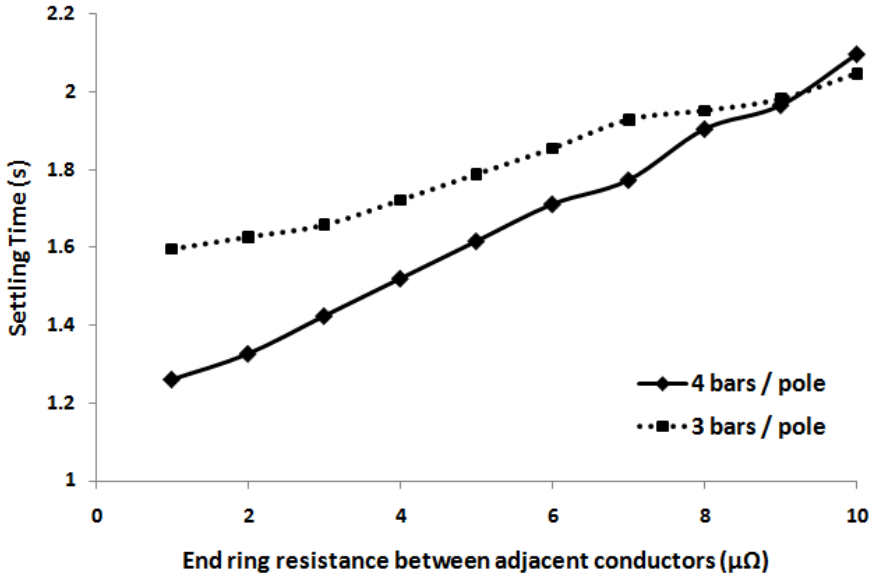

Fig. 56. Effect of end ring resistance on settling time.

IV.3.7. Transient performance with respect to end ring inductance

The inductance between adjacent conductors on the end ring can also be varied. However, due to the relatively low frequencies in the oscillations, the end ring inductance can be set nominally low, or even ignored. Fig. 57 shows a linear relationship between the end ring inductance and the settling time for the salient pole design with 4 and 3 bars per pole. As the inductance, and thus impedance, increases between bars, the settling time increases as it does for the case with resistance. However, the end ring inductance will be kept nominally low at 1 nH for the remainder of the study due to the relatively low frequency of the oscillations concerned.

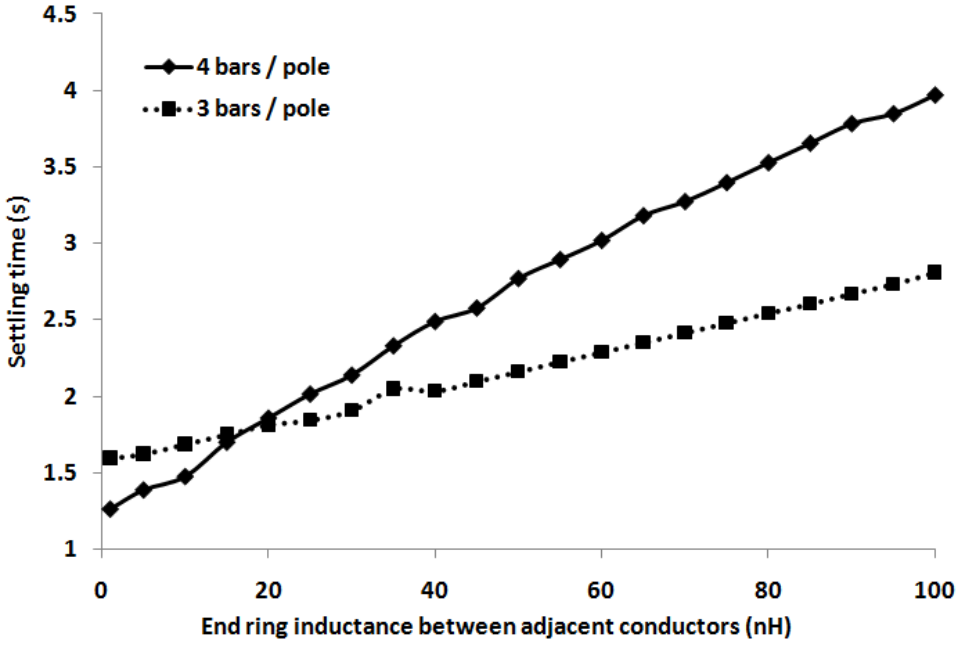

Fig. 57. Effect of end ring inductance on settling time.

IV.4. A Final Design

IV.4.1. Final design parameters

The design using the IPM layout and the salient barriers between adjacent magnets is adopted for the final design, shown in Fig. 58, due to its effectiveness in damping oscillations. The torque density of the gear will be effected by the distance the magnets on the inner rotor are inset. The nominal distance without damper bars for r_{mag} is 43.3 mm. This distance can be offset by up to 4 mm, moving the magnets closer to the shaft to allow room for the damper bars. The effect upon stall torque for the outer rotor is shown in Fig. 59, showing a linear drop with respect to the offset distance due to the added MMF drop in the silicon steel of the rotor yoke.

Using the results obtained earlier, an uninterrupted cage is used, along with a nominal value of 5 μΩ for the end ring, which dictates a roughly 5 mm thick end ring. The nominal value of 1 nH is also used. Due to the relatively good performance of 3 bars compared to 4 per pole, as well as the saturation of the performance due to bar diameter, 3 bars per pole, with a radius of 1.5 mm for each bar, is used in the final design as a tradeoff to limit the flux obstruction in front of the magnets. The bars are set closer to the air gap, and placed in slots to limit the leakage flux due to the bars. In order to keep the stall torque of the gear as high as possible, the magnets are only set back 2.5 mm instead of 4 mm, yielding a stall torque of 21.7 Nm without the damper windings.

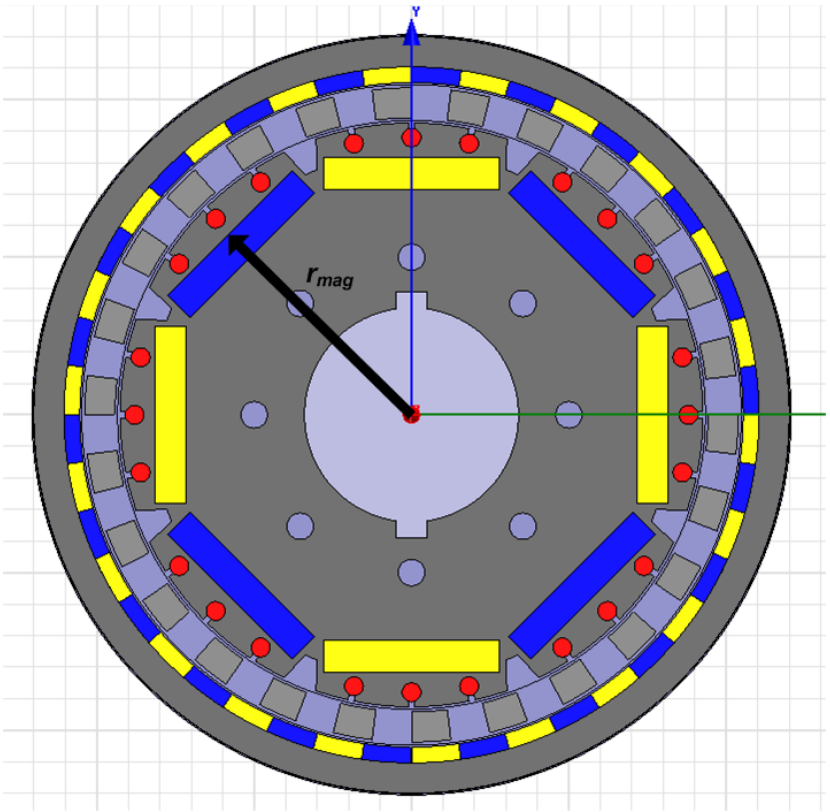

Fig. 58. Final design for the concentric planetary magnetic gear with damper windings.

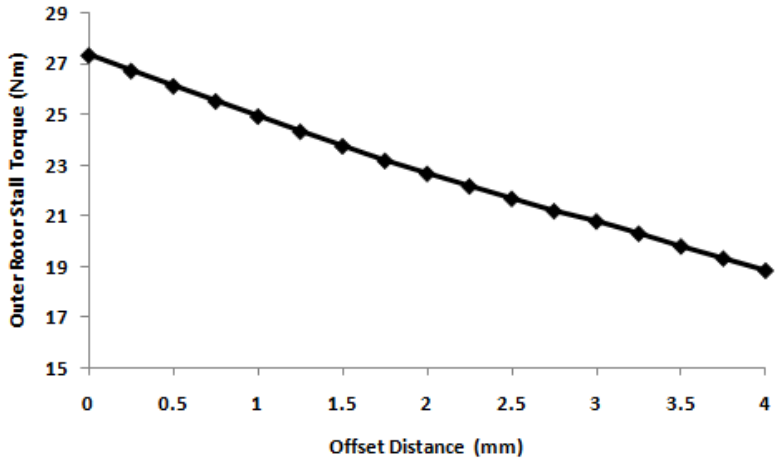

Fig. 59. Stall torque rating of the outer rotor as the inner rotor magnets are shifted towards the shaft.

IV.4.2. Performance of the final design

Fig. 60 shows the transient performance of the final design, with a settling time of 642 ms, compared to 7.817 s without damper windings. The stall torque calculated with FEA with the damper windings is 23.4 Nm. The energy dissipated in the damper windings until the rotor settles to equilibrium is 690 mJ.

It is also worth noting the steady state currents of the damper windings which are shown in Fig. 61. In synchronous generators or line start PM machines, damper windings are expected to carry a negligible current at steady state; however, this is not true for the magnetic gear. This fact can be explained through field analysis of the gear in [4]. The gear under study has 4 pole pairs on the inner rotor, 22 pole pairs on the outer rotor and 26 fixed pole pieces, and thus a gear ratio of -5.5:1. If the gear is run in steady state with the inner rotor rotating at 1 rps, a 4 pole pair field would rotate in the inner air gap at the same speed and direction. Moreover, a 22 pole pair field would be present in

the same air gap due to the outer rotor magnets. The latter field, however, would rotate in the opposite direction at a speed of -1/5.5 rps; thus rotating at the speed of 1-(-1/5.5)=13/11 rps with respect to the inner rotor. A 22 pole pair field rotating at the speed of 13/11 rps induces a voltage in the damper windings whose frequency is 22×13/11=26 Hz. The frequency of the damper bar current waveform presented in Fig. 61 is in very good agreement with this analysis.

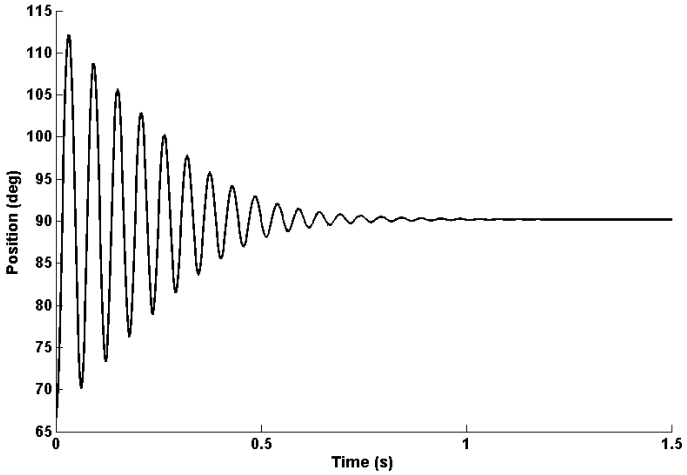

Fig. 60. Transient performance of the final design.

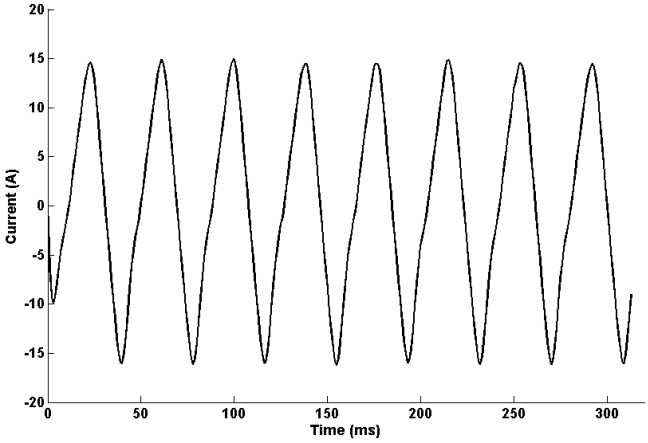

Fig. 61. Current in a damper bar at steady state.

IV.5. Conclusion

While the advantages of magnetic gears over mechanical gears are clear, their effectiveness can be improved using passive means. In particular their torsional stiffness could be a problem in certain applications. Damper windings have been shown to reduce the time in which it takes the inner rotor to oscillate to its final equilibrium position. Different designs have been shown to study their effectiveness, as well as parameters for the damper windings themselves. A design has been settled upon and chosen for its effectives in increasing the torsional stiffness, while maintaining torque density attractive to magnetic gears.

V. THE PROTOTYPE *

V.1. Background and Motivation

The prototype for this dissertation was begun in [5] at the Institute of Energy Technology at Aalborg University. The original prototype was designed for a maximum stall torque of 30 Nm and a stack length which could be supported with bearings from mainly one side. Later, an additional bearing was added to support the inner rotor. The magnetic forces tend to pull the rotors into the stator, causing the gear to grind to a halt.

This prototype was chosen for the envelope in which the variations presented below could be studied. A magnetic gear designed from the ground up requires a considerable amount of design and machine time. In addition, the cost to procure the magnets and cut the laminations can be considerable. In Table IX, a summary of the approximate costs involved in building a magnetic gear prototype are given. The table presents a conservative estimate for a construction which should be relatively "problem free." That is, it is assumed problems discussed later with regards to assembly are avoided with sufficiently good design and mechanical experience. Problems encountered with assembly can quickly escalate cost. The costs are based upon quotes received from various sources, and a machinist's rate of $50/hour.

Table IX. Cost for magnetic gear prototype

Item	Cost (USD)
Magnets (Nd-Fe-B)	800
Lamination cutting	2000
Bearings	200
End caps, housing, bracket	500
Labor	2000
Total	5500

V.2. Design

The proposed gear, the parameters of which are given in Table X, has different variations of the stator which can be fabricated. Shown in Fig. 62, three ways of connecting the stator pieces are shown, with 0.3 mm bridges between them.

Table X. Magnetic gear dimensions

Parameter	Value (mm)
Outer radius of outer rotor	60
Inner radius of outer rotor	52.7
Inner rotor radius	46.3
Inner radius of stator pole pieces	47.1
Outer radius of stator pole pieces	51.9
Stack length	26
Inner rotor magnet thickness	5
Outer rotor magnet thickness	2.5

These correspond to the smallest possible bridges which could be fabricated with an electrostatic discharge machine (EDM). First looked at in [47], the effect of closing the segments on the interior was found to have a 4% reduction in stall torque rating. These variations will be studied initially to find if there is a greater cost to having bridges adjacent to one rotor or another.

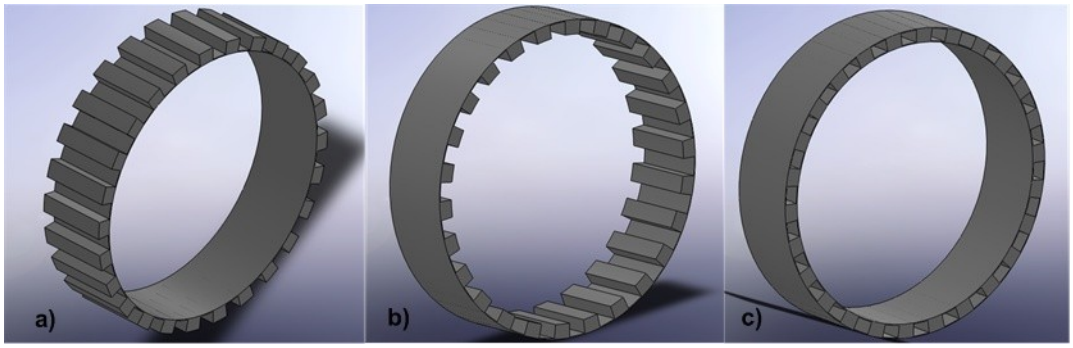

Fig. 62. New variations of the stator with arrows pointing to bridges connecting the stator pieces on the (a) interior, (b) exterior, and (c) both sides.

In addition to a new stator arrangement, it is also possible to use interior permanent magnet design tools used on synchronous machines for the magnetic gear. This has the advantage of negating the use of a retaining can for surface mount magnets. This could be used as an advantage for electromechanical systems which need to be run at higher speeds as well. Shown in Fig. 63a, the configuration uses the same amount of magnetic material used in [5]. The corresponding torque angle curves calculated with FEA are given in Fig. 63b. Finite element analysis has been used to simulate the behavior of the different magnetic gear variations. The results of the variations are presented in Table XI for Maxwell and MagNet.

The results also show that connecting the stator pieces on the interior costs less in stall torque rating than connecting them on the exterior, roughly 2% versus roughly 23% respectively. The results also show a considerable drop in stall torque rating between surface mount magnets and the IPM layout. The surface mount configuration however is an ideal configuration which does not account for the retaining can. In [47], a 3 mm

thick retaining can was used for the surface mount magnets, resulting in a 23% drop in stall torque rating.

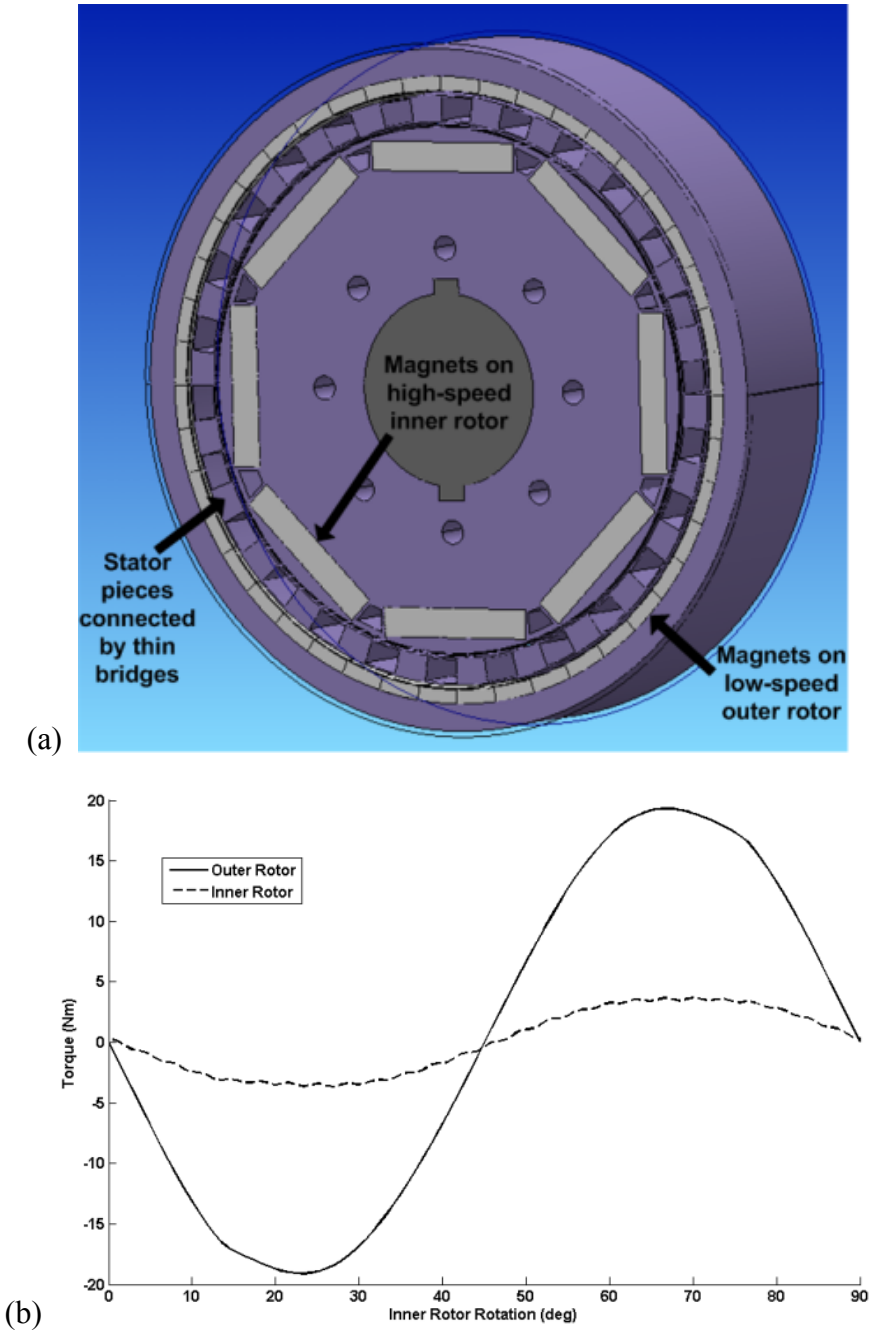

Fig. 63. Prototype (a) FEA model and (b) FEA-calculated torque angle curve.

Table XI. Stall torque rating for different FEA packages and variations of the stator

Variation	Maxwell Torque (Nm)	MagNet Torque (Nm)
Surface mount magnets with pole pieces	32.67	31.61
Interior magnets with pole pieces	24.49	25.95
Interior magnets with pole pieces connected on interior	24.08	25.43
Interior magnets with pole pieces connected on exterior	19.24	19.72
Interior magnets with pole pieces connected on interior and exterior	18.85	19.33

Fig. 64 shows the results of changing the thickness of the bridges, when only one side is taken into account. It is apparent that the bridges on the exterior detract from the stall torque rating at a quicker rate than the addition of bridges on the interior. The shorter span between adjacent poles on the outer rotor leads to more leakage flux paths with the addition of the bridges. In terms of the magnetic flux path, it is ideal for the bridges to be as thin as possible to achieve the highest stall torque rating for a given stack length.

There is a trade-off for mechanical strength in the addition of the bridges. The torsional twist angle exerted upon the stator, with a given torque, material, and stack length, will only change with respect to the polar moment of inertia of any stator model. In fact, the torsional twist angle, shown in (60) is inversely proportional to the polar moment of inertia, which is the highest for the stator with bridges on both sides. Thus, this model would result in the smallest twist angle for a given torque. Compared to this model, there is a 4.8% decrease in the polar moment of inertia when bridges are only

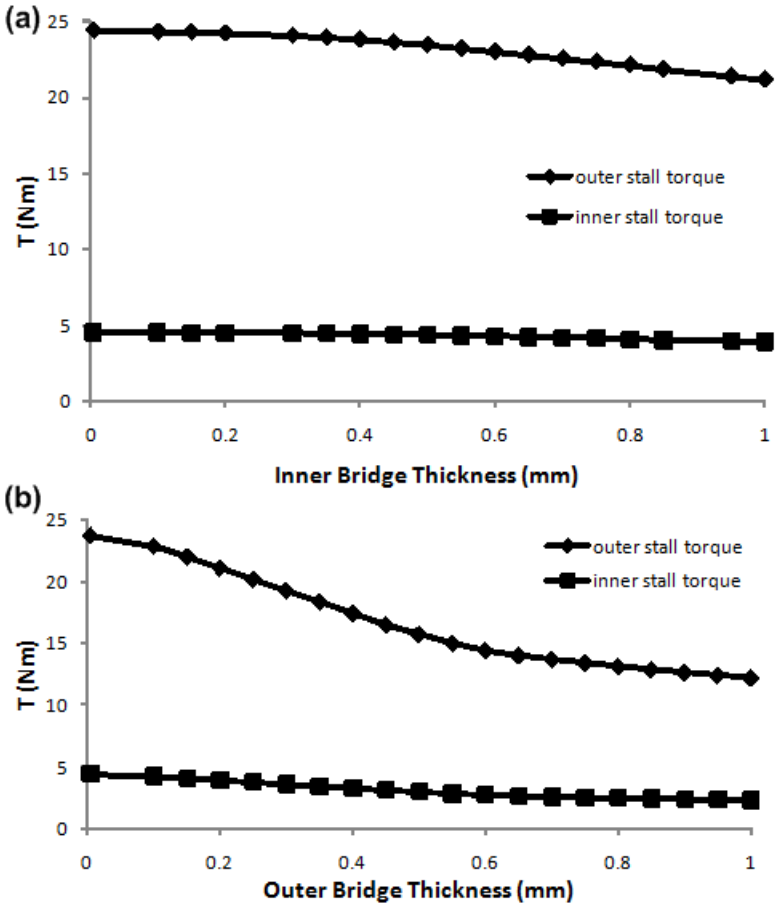

Fig. 64. Stall torque raring with respect to bridge thickness for (a) inner connection and (b) outer connection.

$$\theta = \frac{Tl}{GJ} \tag{60}$$

on the outside, and 6.33% decrease when bridges are only on the interior.

V.3. Analysis of the New Construction with Modified Winding Function Theory

The theory behind analyzing the gear with MWFT has been presented for an ideal construction, and will now be applied to the new variation of the magnetic gear, an FEA model of which is shown in Fig. 63a, and the resultant torque angle curves in Fig. 63b.

The validity of building the model with coils is tested by comparing the stall torque ratings of the models built with coils and with magnets, shown in Fig. 65.

The torque waveforms shown in Fig. 65 reveal an operating point for the magnets which is less than the remanent magnetization used in (35). Adjusting for the operating point, the MMF for the magnets used in the inductance calculations is 2061 ampere-turns.

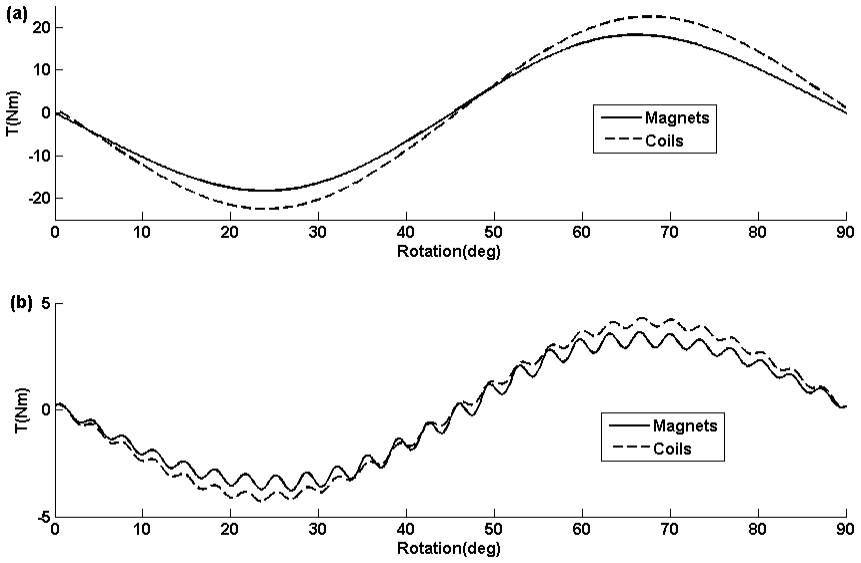

Fig. 65. Torques calculated using coils and permanent magnets with FEA for (a) outer rotor and (b) inner rotor.

V.3.1. Effect of the IPM geometry upon inductance

Now the models built with coils are used to calculate the inductance waveforms for the rotors. The magnetizing inductances for one pole pair rotation of each rotor are given in Fig. 66. The mutual inductances for a single pole pair rotation of the rotors is presented in Fig. 67.

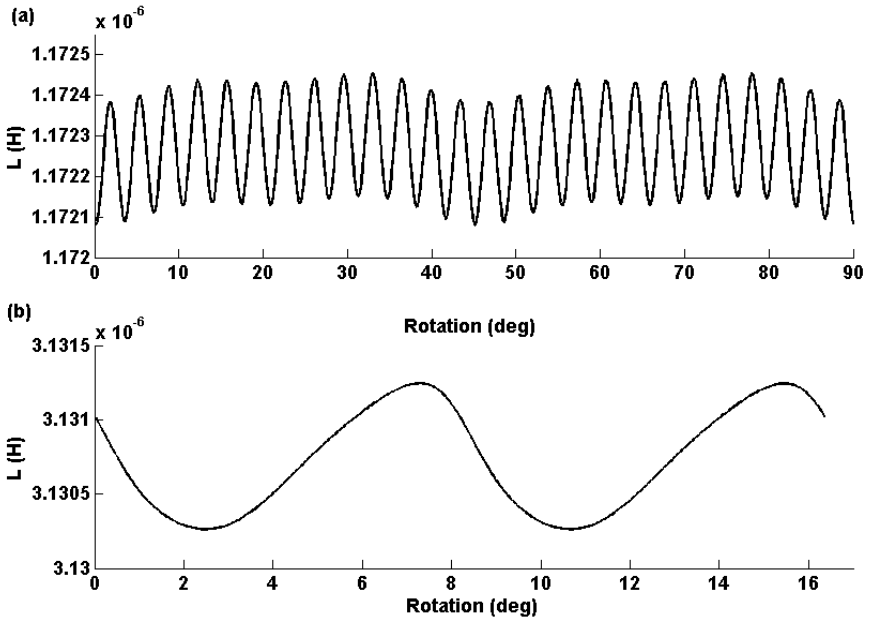

Fig. 66. Magnetizing inductances calculated with FEA for (a) inner rotor, and (b) outer rotor.

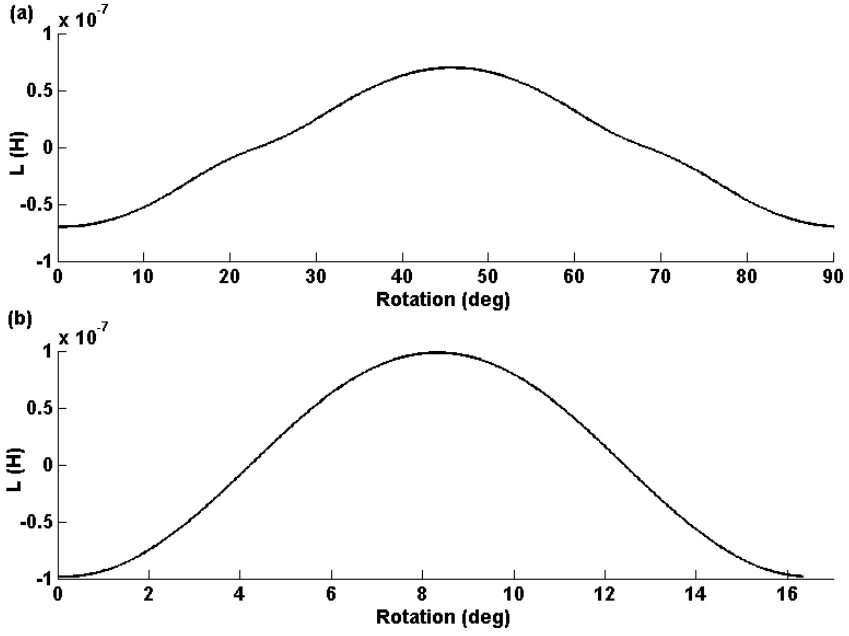

Fig. 67. Mutual inductances calculated with FEA for (a) inner rotor and (b) outer rotor.

From a look at the magnetizing inductances in Fig. 66, the FEA results show a fundamental frequency equal to the number of poles of the interior rotor, 8, and a prominent harmonic of pole pairs multiplied by stator pole pieces, 104. For the outer rotor, a fundamental frequency exists which is equal to the number of poles on the outer rotor, 44. The mutual inductances exhibit a sinusoidal shape per pole pair pitch which will later result in the stall torque curves. While the mutual inductances are nominally equivalent for the ideal construction, as seen in Fig. 45, their calculation for the IPM geometry produces different magnitudes due to the flux leakage paths shown circled in Fig. 68.

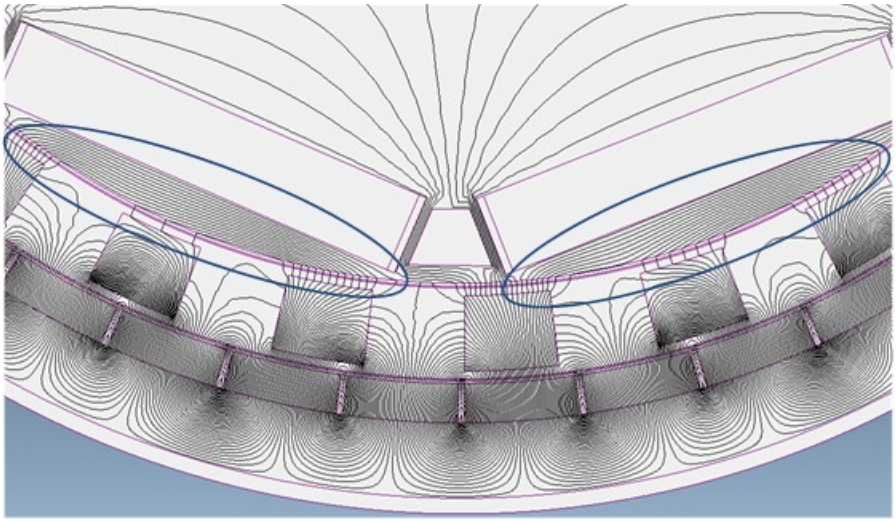

Fig. 68. Additional flux leakage paths shown circled in the calculation of L_{io}.

Care is taken to construct the turns function of the inner rotor. While the turns function of the outer rotor is more equivalent to a full-pitched square wave, the inner rotor will resemble a trapezoidal wave which is short-pitched. The Fourier series, shown in Fig. 69 and described by (61) is used to model the field due to the inner rotor [60]:

$$n(\phi,\theta) = N + \frac{2*N}{\pi}\sum_{h=1,3,5,..}^{\infty}\frac{\sin\left(\frac{h\beta}{4}\right)}{\frac{h\beta}{4}}\cos\left(\frac{\varepsilon}{2}\right)\left(\frac{1}{h}\right)\cos(h\theta + h\phi) \quad (61)$$

,

where Φ is a phase shift which represents the rotation of the rotor and N is the number of turns in a single coil, one in this case. The measure of how the MMF tapers off at the magnet ends is given by β, 16.24° in this case. The short pitching between the magnets is represented by ε, 28.76° in this case.

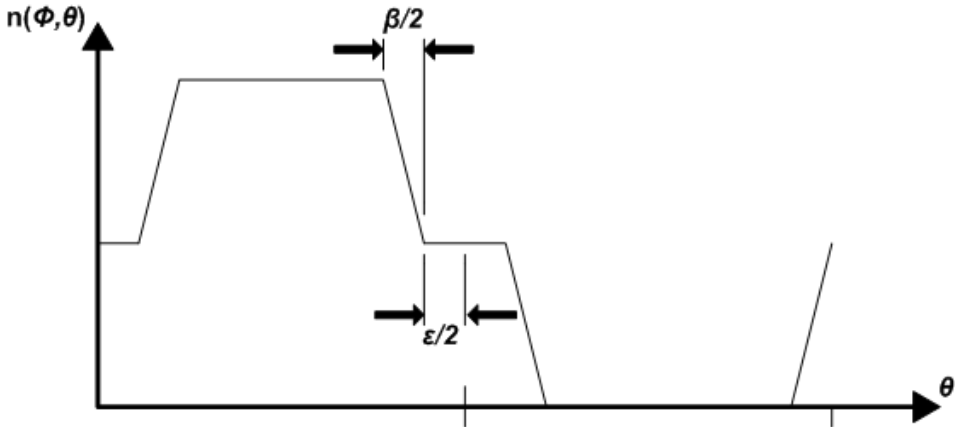

Fig. 69. Turns function for inner rotor.

The inductances are calculated using Matlab/Simulink, shown in Fig. 70 for the magnetizing inductances and Fig. 71 for the mutual inductances. Over a pole pair pitch, the magnetizing inductance calculated for the inner rotor has a fundamental harmonic equal to the number of poles, 8. In addition, both inductances calculated with FEA and MWFT show a prominent harmonic equal to the number of stator pole pieces multiplied by the number of pole pairs, 104.

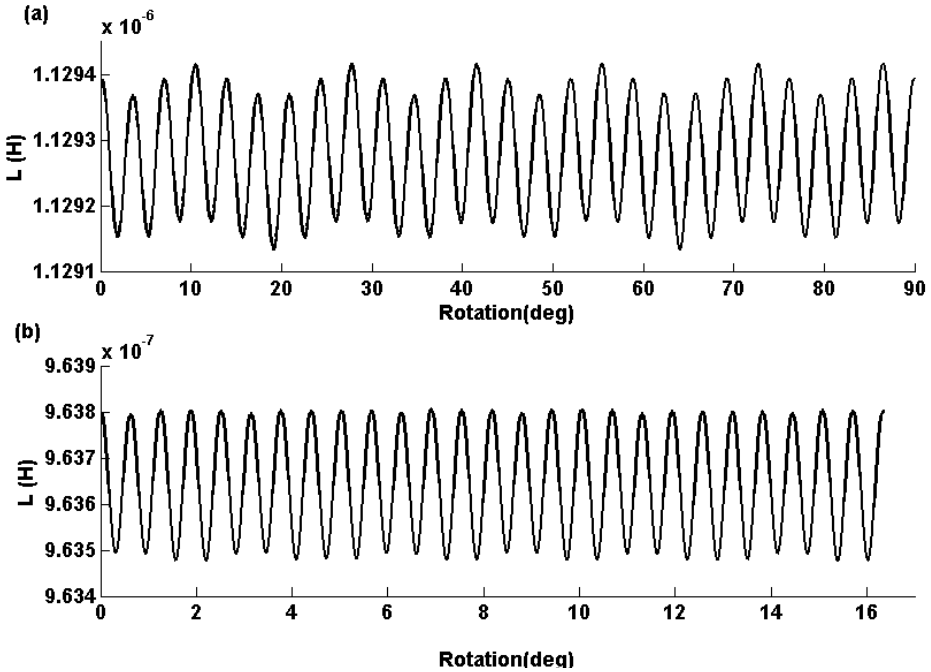

Fig. 70. Magnetizing inductances calculated with MWFT for (a) inner rotor and (b) outer rotor.

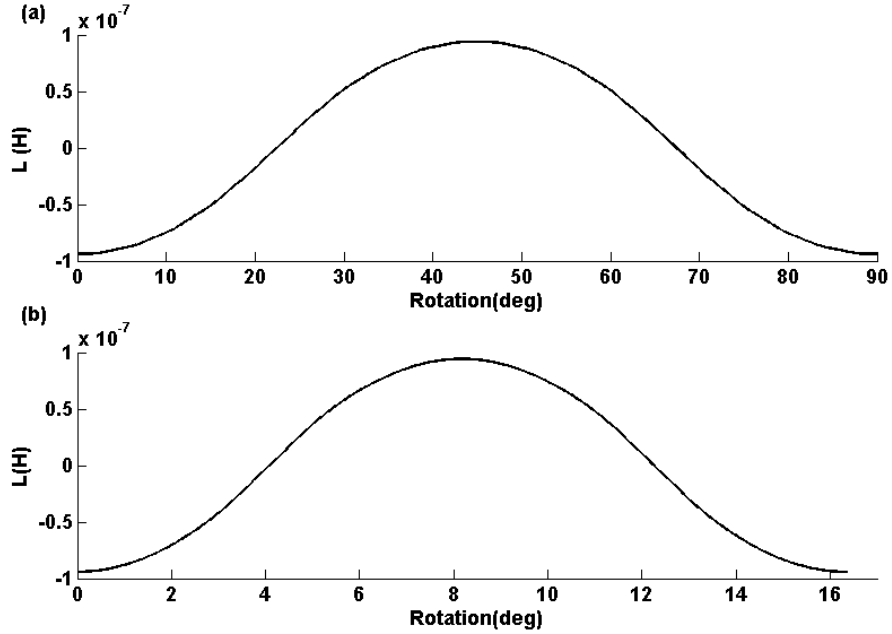

Fig. 71. Mutual inductances calculated with MWFT for (a) inner rotor and (b) outer rotor.

The magnetizing inductance of the outer rotor has a fundamental harmonic equal to the number of pole pairs, 22, and prominent harmonics which are multiples thereof. The inductance calculated with MWFT exhibits in particular a prominent harmonic equal to the number of pole pairs multiplied by pole pieces, 572.

These differences exist due to the fact that the MWFT calculations do not take fringing flux into account. As seen with the analysis for the ideal construction, the combination of pole pairs to slots (i.e. teeth in the case of magnetizing inductance) in the gear studied also matches a combination presented in [67] for a machine which is incapable of generating strong high frequency components. In this special combination, the physical system, as well as that calculated by FEA, will mask higher slot harmonics than those shown with MWFT. The mutual inductances are in good agreement with those calculated by FEA, with the difference in magnitude coming from added MMF drops in the FEA calculations.

V.3.2. Effect of the stator bridges upon inductance

As with teeth in a conventional electric machine, the change in the reluctance over the circumference of the stator has an effect upon the inductance and thus the cogging torque of the machine. Closing the segments has the effect of reducing the cogging torque, at the expense of introducing more leakage flux paths, shown in Fig. 72, and thus detracting from the stall torque rating of the gear. Fig. 73 shows the magnetizing inductances calculated with FEA by closing the segments between the stator pole pieces with 0.3 mm bridges.

The addition of the bridges induces more prominent harmonics in the inner rotor magnetizing inductance equal to twice the number of the stator pole pieces, 52. Another prominent harmonic exists equal to twice the number of pole pieces multiplied by the number of pole pairs, 208. The outer rotor magnetizing inductance retains a harmonic equal to the number of poles, 44. However, higher harmonics which are multiples of 44 are more prominent than the inductance waveform calculated without bridges.

The addition of bridges in the calculation of the mutual inductances shown in Fig. 74 shows a reduction of magnitude compared to Fig. 71. This is also due to the addition of flux leakage paths shown in Fig. 72.

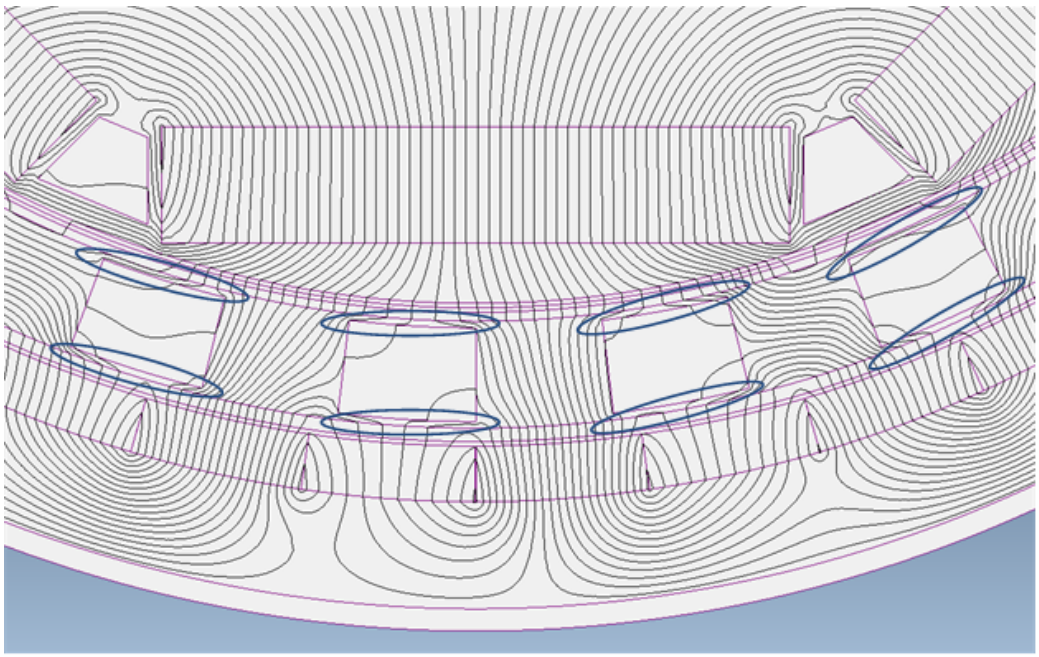

Fig. 72. Flux aided by the addition of stator bridges shown circled.

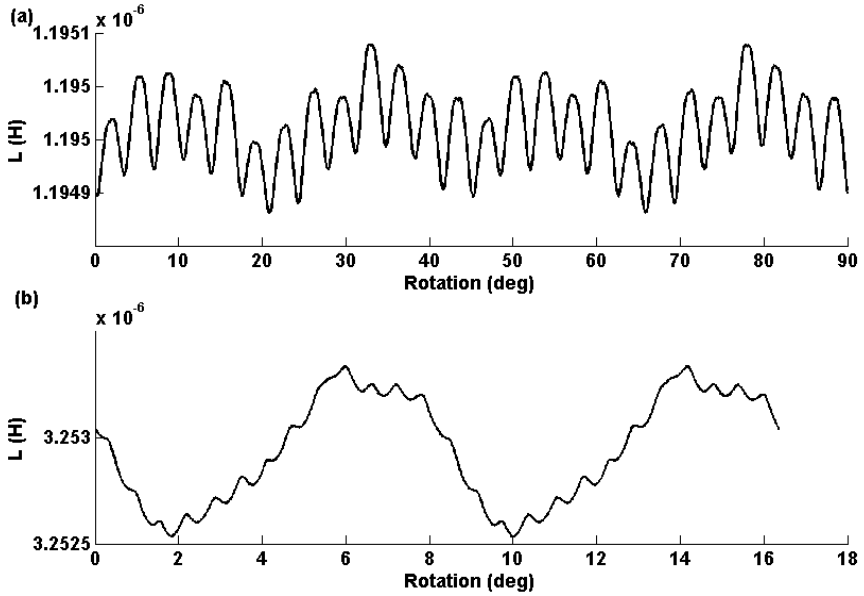

Fig. 73. Magnetizing inductances for stator segments connected with bridges calculated with FEA for (a) inner rotor and (b) outer rotor.

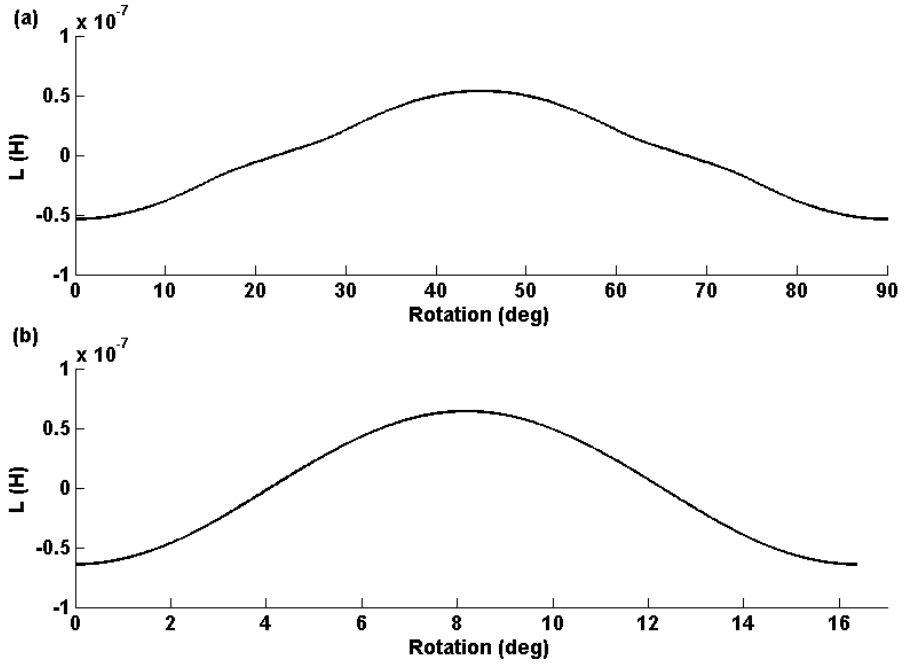

Fig. 74. Mutual inductances for stator segments connected with bridges calculated with FEA for (a) inner rotor and (b) outer rotor.

V.3.3. Torque output using MWFT

Using the inductances calculated with the IPM layout, and the MMF values adjusted for the magnetic operating point, the torques are calculated using (52) and (53) and shown in Fig. 75. The cogging torque shows an amplitude of ±0.098 Nm on the inner rotor and ±0.19 Nm on the outer rotor. The stall torque for the outer rotor is 19.73 Nm while the inner rotor is 3.71 Nm, providing a gearing ratio of 5.32:1.

By comparison, FEA gives a stall torque of approximately 19 Nm between the two packages. The stall torque curves calculated by FEA are given in Fig. 63b. By contrast, the steady state torque ripple calculated with FEA is given in Fig. 76. Neglecting offsets which are present due to an operating point along the stall-torque curve which is near zero, the dominant frequency for a rotation of one pole-pair is equivalent to that seen in Fig. 75.

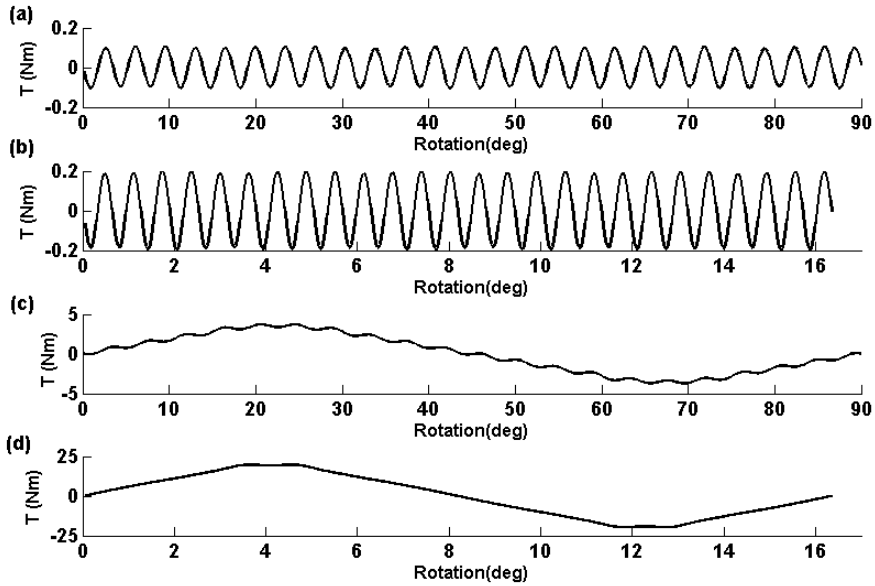

Fig. 75. Torques calculated with MWFT accounting for IPM geometry for (a) inner rotor cogging torque, (b) outer rotor cogging torque, (c) inner rotor stall torque, and (d) outer rotor stall torque.

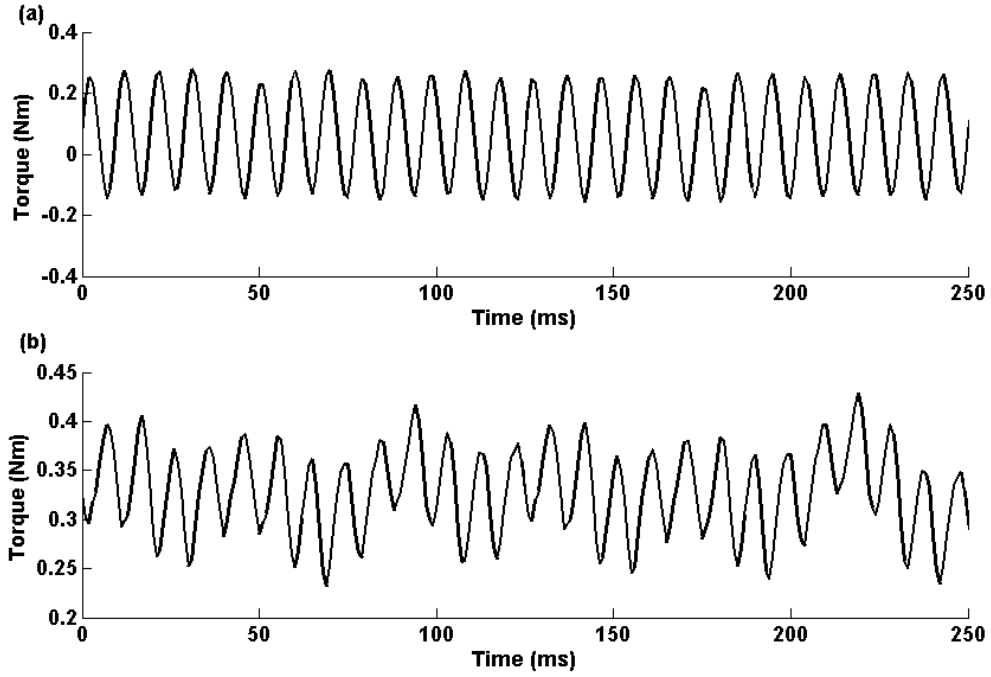

Fig. 76. Steady state torque ripple calculated with FEA for the (a) inner rotor and (b) outer rotor.

V.4. Construction

A new prototype has been assembled using the stator configuration with both an inner and outer connection, and an interior permanent magnet configuration. The laminations, cut by EDM are shown in Fig. 77a before their assembly. The assembled stator and inner rotor within the mechanical housing of the magnetic gear is shown in Fig. 77b. The inclusion of bridges on both sides of the stator allowed for a construction which could be accomplished in the lab. A mold, a sectioned assembly view of which is shown in Fig. 78a, was used to stack the stator laminations in concentricity with the outer and inner rotors. The holes created by stacking the laminations allowed for the

simple use of epoxy and threaded aluminum rods to adhere the stator stack to the mechanical base, shown in Fig. 78b.

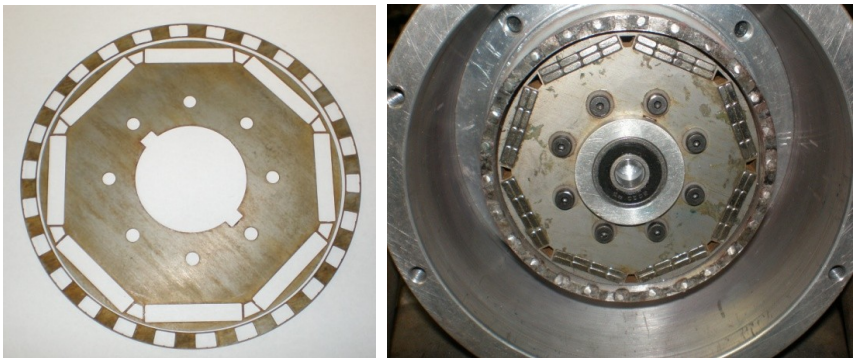

(a) (b)

Fig. 77. New inner rotor and stator redesign with (a) laminations shown and (b) assembled with magnets.

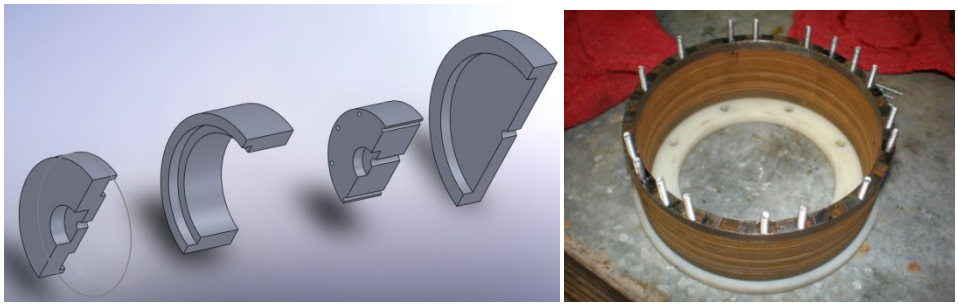

(a) (b)

Fig. 78. Assembly of stator with (a) sectioned view of mold and (b) stack with aluminum rods to adhere stack to base.

V.4.1. Assembly problems for the inner rotor

The assembly of the inner rotor was relatively straightforward compared to the stator stack. With proper design and cutting of the laminations, problems are avoided with placement of magnets as well as the shaft. The rectangular holes cut for the magnets, shown in Fig. 79a, were made larger to account for the magnet coatings as well as the glue which held the magnet pairs together, and to the lamination stack. *Loctite 330*

glue was used to join the magnets in pairs, and then glue individual pairs in the slot holes. Each slot could accommodate 16 magnets, shown in Fig. 79b. Thus, each slot was filled with 8 pairs of magnets placed and glued individually. The final pair in each slot proved to be the most difficult, due to the repulsion by neighboring magnets, and the tight fit.

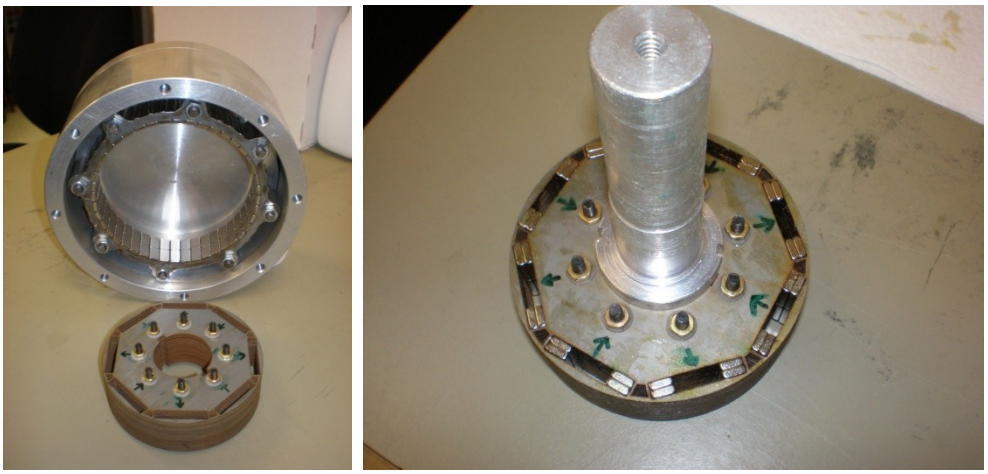

(a) (b)

Fig. 79. Assembly of the inner rotor (a) before magnets shown in front of outer rotor assembly and (b) during placement of magnet pairs.

V.4.2. Assembly problems for the stator stack

The stator stack was the most difficult component to assemble for the magnetic gear prototype. One of the key difficulties in the construction and assembly of the stator stack was due to the existence of critical air gaps on both sides of the laminations. This made construction more difficult, as common means of adhering stacks together for traditional electric machines such as welding could not be used. Nor could bolts be used in the final construction, since the bolts themselves were large enough to interfere with the air gaps.

Shown in Fig. 80, the second and third iterations of the stator stack are shown. The first iteration, not pictured, failed due to the poor adhesion between the stack and the base. Once threaded aluminum rods were added, shown in Fig. 78b, the stator stack was sufficiently strong enough to withstand the forces which could pull it off during assembly. The new problem encountered however was due to the concentricity between the inner and outer rotors. The mold used, was not sufficient to guarantee concentricity with 0.8 mm air gaps on both sides. This resulted in contact and thus scraping between the outer rotor and the stator stack. A blue marker was used on the second iteration of the stator stack, shown in Fig. 80 to identify the points of contact. The points of contact were obvious on the magnets, resulting in a loss of their coating, shown in Fig. 81.

Fig. 80. Second (left) and third (right) iteration of the stator stack.

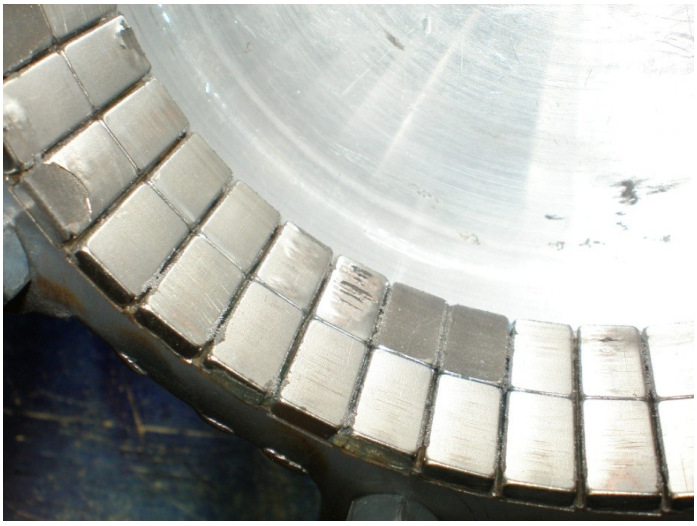

Fig. 81. Magnets on the outer rotor with lost coatings due to contact with stator stack.

In the third and final iteration of the stator stack, the mold was still required. However, the lath was used, along with a dial indicator to verify concentricity. The stator stack inside the mold, operated in the lathe is shown in Fig. 82. Also shown are the bolts at the top of the threaded aluminum rods. These bolts were used to press the stack down. As epoxy was added to the holes, and later hardened, these bolts were removed.

Fig. 82. Verification of stator stack concentricity by using the lathe.

V.5. Results

A dynamometer has been setup to test the gear, shown in Fig. 83. The high-torque side of the gear is driven by an induction servo-motor. The low-torque side is loaded by a hysteresis brake capable of stalling the gear. Each side of the gear has its own torque transducer and encoder.

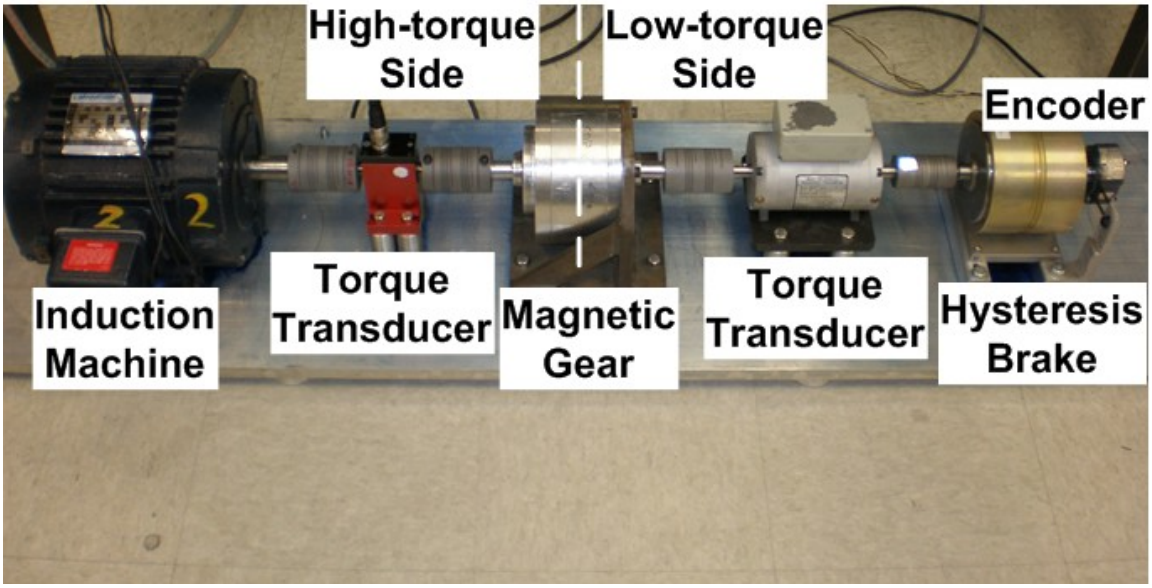

Fig. 83. Dynamometer for testing the magnetic gear prototype.

For the no-load test performed on the gear, Fig. 84 shows a 1.4 Nm peak-to-peak torque ripple on the outer rotor and a 0.067 Nm peak-to-peak torque ripple on the inner rotor. The load from the hysteresis brake is steadily increased to verify the stall torque of the gear, shown in Fig. 85. The outer-rotor torque waveform shows the torque exerted on the rotor increasing until 12.3 Nm, when the inner rotor stalls.

The stall torque of the new prototype corresponds well with that found in [5], 16 Nm. The new prototype, with 0.3 mm bridges on the inside and outside corresponds with

an approximate 23% reduction in stall torque. The new prototype also has a 0.1 mm increase in the air gap on both sides as well to aid in assembly.

The stall torque for the new prototype has a torque density of approximately 42 Nm/l for the volume of the active components, compared with a calculated torque density of 64 Nm/l with Maxwell and almost 66 Nm/l with MagNet. Thus the constructed prototype yields 64-65% of the calculated torque density. This is in good agreement with results obtained in [4] and [5] , with the reduction coming from end effects of the magnets.

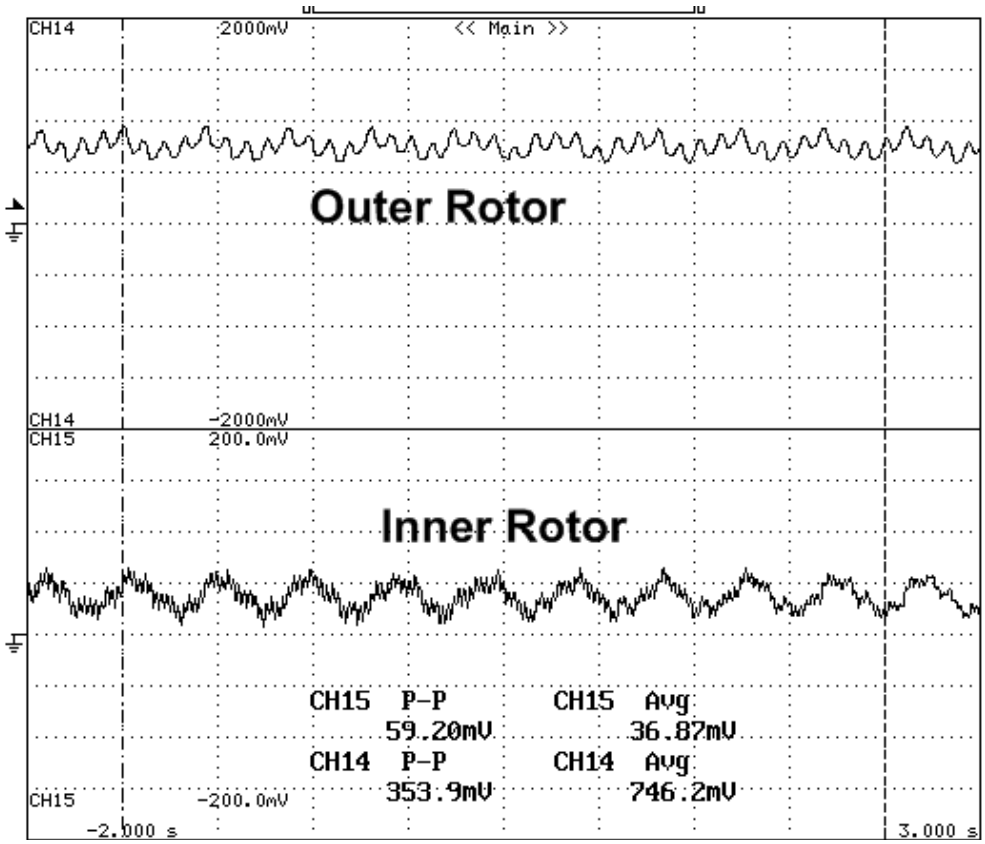

Fig. 84. Steady-state torque ripple of the gearbox under no load.

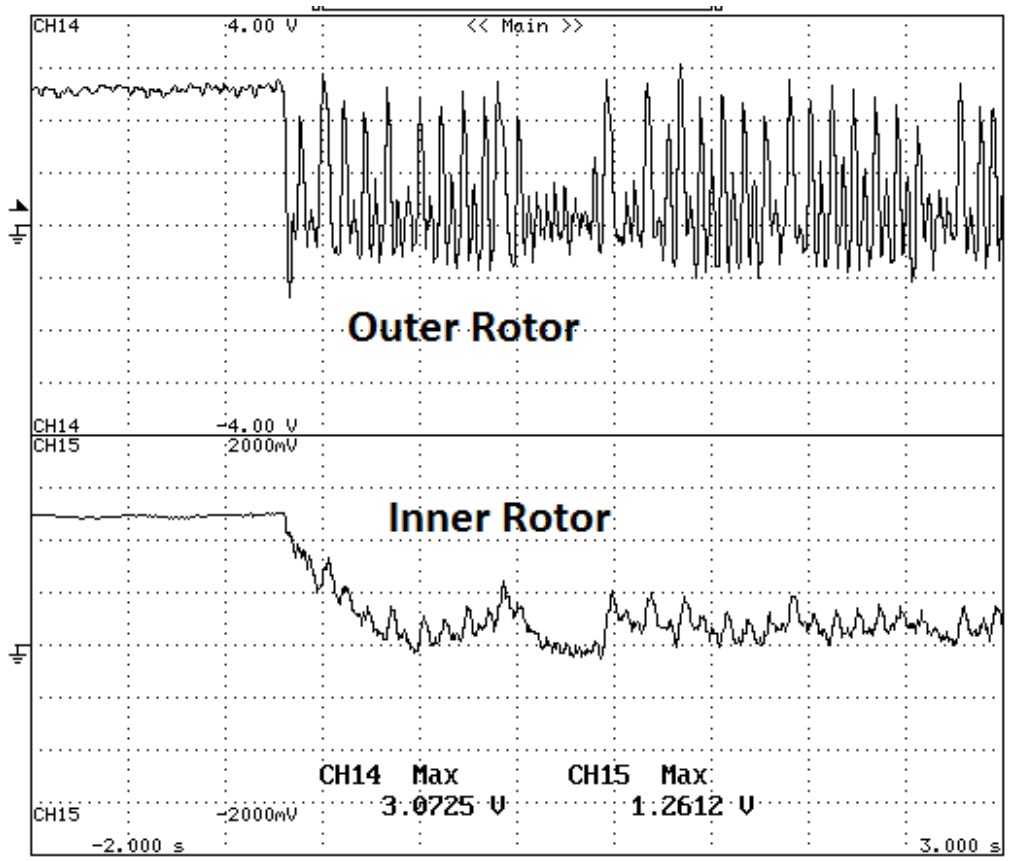

Fig. 85. Torque waveforms of both rotors when inner rotor experiences a stall.

V.6. An Improved Design

The prototype discussed in this work suffers from limitations incurred by the original prototype. This prototype was supported from bearings which were primarily on one side of the rotor. An additional bearing was placed between the rotors in [5], which was not part of the original design. The modifications to the prototype in this work included the replacement of all of these angular contact bearings, shown in Fig. 86a. Since the rotors were supported mainly from one side, this necessitated the use of tapered roller bearings, which are loaded, shown in Fig. 86b.

(a) (b)

Fig. 86. Replacement of bearings from (a) angular contact to (b) tapered roller.

A modification to this prototype would eliminate the losses incurred by the use of the tapered roller bearings. These modifications are shown in Fig. 87. In this modified design, the bearings would not need to be loaded, and would result in a higher overall efficiency for the gearbox. In addition, by fixing the outer magnetic gear, a full incremental gear ratio is achieved within the same volume.

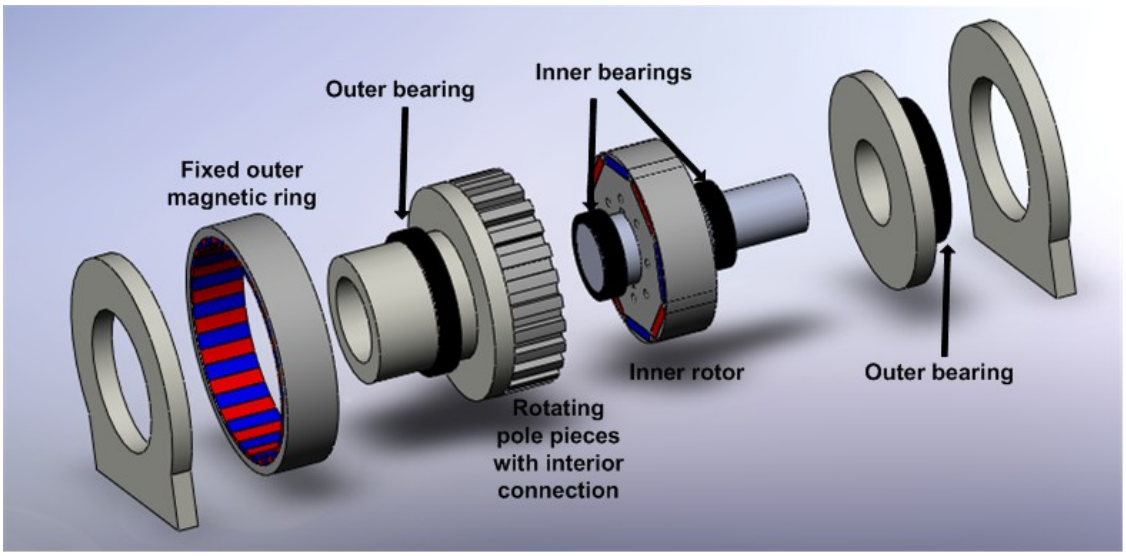

Fig. 87. New prototype with rotors supported from both sides.

V.7. Conclusion

Different variations of the magnetic gear have been presented which could spur more use by strengthening one of the key components of the gear, the stator pole pieces. It has been shown that the stator is not only a critical component to the performance of the gear, but also requires detailed analysis for any models to be accurate. Finite element analysis, while useful and accepted, is tedious for testing different variations and performing parametric studies of certain components of the gear. A new method of analysis which uses winding function theory can run quicker and offer faster insight into changing parameters of the gear. In the magnetic gear studied, it has been shown that while using a more convenient stator segment construction and IPM layout, this also comes at the expense of stall torque rating of the gear.

VI. SUMMARY AND CONCLUSIONS

VI.1. The Appeal of Magnetic Gears

While mechanical gears have been around for centuries, their development in certain applications has come to a plateau. Applications such as wind turbines continually demand more reliable components which can handle the high stresses which blade hubs produce. Magnetic gears provide a significant leap over mechanical gears due to the loss of contact, and their inherent overload capability. In addition, for applications such as traction in which volume constraints are much tighter, the ability to integrate a synchronous machine within the gear can greatly reduce system size and provide added torque and control.

VI.2. Future Work

While the idea of permanent magnet gears is roughly 70 years old at the time of this writing, the majority of the prototyping has only been done in the last ten years. More institutions are seeing this emerging field and recognizing its potential. There is still a great deal of work to be done with magnetic gears to bring them to maturity and industrial use on a wide scale.

One of the biggest challenges remains to be tackled is the scaling of the gear. While large electric machines, even permanent magnet machines, have been built in industry and are in wide use, it is left to be studied how the magnetic gear scales in size and torque compared to an electric machine, and even mechanical gears.

In addition, while the efficiencies which are calculated with magnetic gears are comparable to mechanical gears, a study has yet to be done to accurately measure and characterize core losses as well as eddy current losses in the coatings of the magnets in magnetic gears which are run at high speed. While magnetic gears share the same bearing losses as mechanical gears, they differ in these core losses.

New designs continue to emerge for magnetic gears which offer higher torque densities and even variable gear ratio. There will undoubtedly be future work with regards to new designs. However, the success of any new design will ultimately be judged upon its ease of construction. New designs which offer good torque densities, yet require exotic magnetic and bearing layouts could ultimately remain an academic exercise while designs which are simpler to manufacture are slowly introduced into industrial products.

With the increasing computational power of personal computers, the ability to tackle 3D FEA simulations is quickly becoming a new tool to machine designers. The end effects mentioned in the 2D analysis of this dissertation detract a considerable amount of the final stall torque of the prototype, depending upon stack length. Future work in magnetic gears will undoubtedly benefit from 3D FEA, an example of which is shown in Fig. 88 using MagNet's 3D static solver. The process is still slow compared to the 2D solution and models must be made with fewer errors in order to converge upon a solution. However, even the use of the static solver could help determine the correct scaling factor for the 2D analysis to estimate a true stall torque for prototyping.

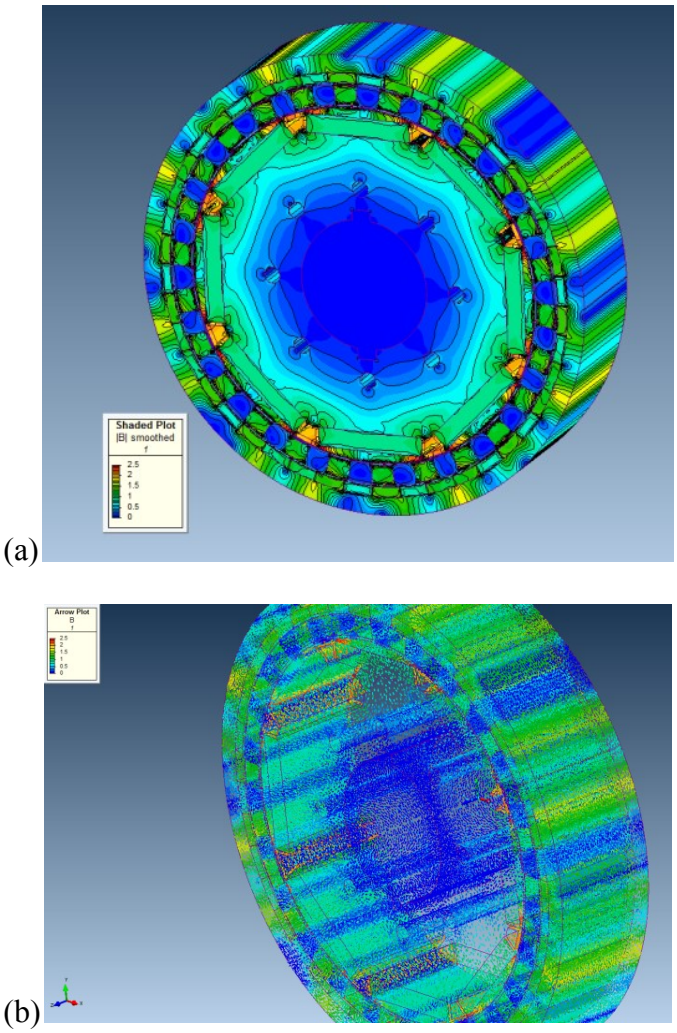

Fig. 88. 3D model of the magnetic gear simulated in MagNet's 3D static solver showing solutions for the (a) shaded flux density field and the (b) vector field of flux density.

There are three questions that I'm continually asked as I present this work on magnetic gears:

- How does the efficiency compare to mechanical gears?
- How does the torque density compare to mechanical gears?

- Is there a way of constructing the magnetic gear to have a variable gear ratio?

Each of these three questions constitutes its own research project and will be a welcome addition to the body of work being done on magnetic gears.

VI.3. Conclusion

This dissertation has presented variations of the concentric planetary magnetic gear which could lead to its adoption in industrial use. The preliminary analysis has showed that the gear ratio plays a key role in torque ripple, as well as the layout of the magnets. A new means of analysis has also been employed the magnetic gear which can quickly yield stall torque and cogging torque waveforms to aid in analysis which is primarily done with FEA. To aid in the torsional stiffness problem of the magnetic gear, damper windings have been added to suppress transient oscillations due to changes in speed and load. In addition, a prototype has been constructed which implements a variation of the stator pole pieces.

The continued interest in magnetic gears is very promising. The number of institutions performing research into magnetic gears is increasing, and continued research should yield industrial products down the road.

REFERENCES

[1] H.T. Faus, "Magnet gearing," U.S. Patent 2,243,555, May 27, 1941.

[2] K. Tsurumoto and S. Kikuchi, "A new magnetic gear using permanent magnet," *IEEE Tran. Magn.*, vol. 23, no. 5, pp. 3622-3624, Sept. 1987.

[3] K. Atallah and D. Howe, "A novel high-performance magnetic gear," *IEEE Trans. Magn.*, vol. 37, no. 4, pp. 2844-2846, July 2001.

[4] K. Atallah, S. Calverley, and D. Howe, "Design, analysis and realisation of a high-performance magnetic gear," *IEE Proc. Electr. Power Appl.*, vol. 151, no. 2, pp. 135-143, Mar. 2004.

[5] P. Rasmussen, T. Andersen, F. Jorgensen, and O. Nielsen, "Development of a high-performance magnetic gear," *IEEE Trans. Ind. Appl.*, vol. 41, no. 3, pp. 764-770, May/Jun. 2005.

[6] J. Wang and K. Atallah, "Modeling and control of 'pseudo' direct-drive brushless permanent magnet machines*,"* in *Proc. IEEE Int. Conf. IEMDC 2009*, Miami, FL, pp. 870-875.

[7] L. Shah, A. Cruden, and B. W. Williams, "A magnetic gear box for application with a contra-rotating tidal turbine," in *Proc. IEEE 7th Int. Conf. PEDS 2007*, Bangkok, Thailand, pp. 989-993.

[8] L. Jian, K.T. Chau, Y. Gong, J.Z. Jiang, C. Yu, and W. Li, "Comparison of coaxial magnetic gears with different topologies," *IEEE Trans. Magn.*, vol. 45, no. 10, pp. 4526-4529, Oct. 2009.

[9] L. Yong, X. Jingwei, P. Kerong, and L. Yongping, "Principle and simulation analysis of a novel structure magnetic gear," in *Proc. IEEE Int. Conf. ICEMS 2008*, Wuhan, China, pp. 3845-3849.

[10] C.C. Huang, M.C. Tsai, D.G. Dorrell, and B.J. Lin, "Development of a magnetic planetary gearbox," *IEEE Trans. Magn.*, vol. 44, no. 3, pp. 403-412, Mar. 2008.

[11] F.T. Jorgensen, T.O. Andersen, and P.O. Rasmussen, "The cycloid permanent magnetic gear," *IEEE Trans. Ind. Appl.*, vol. 44, no. 6, pp. 1659-1665, Nov./Dec. 2008.

[12] J. Rens, R. Clark, S. Calverley, K. Atallah, and D. Howe, "A novel magnetic harmonic gear," *IEEE Trans. Ind. Appl.*, vol. 46, no. 1, pp. 206-212, Jan./Feb. 2010.

[13] R.J. Drago, *Fundamentals of Gear Design*, Boston, MA: Butterworths, 1988.

[14] J.E. Shigley, *Mechanical Engineering Design*, First Metric Edition, New York, NY: McGraw-Hill, 1986.

[15] H.W. Müller, *Epicyclic Drive Trains: Analysis, Synthesis, and Applications*, Detroit, MI: Wayne State University Press, 1982.

[16] F.L. Litvin and A. Fuentes, *Gear Geometry and Applied Theory*, Cambridge, U.K.: Cambridge University Press, 2004.

[17] X. Luo, Y. Liao, H.A. Toliyat, A. El-Antably, and T. A. Lipo, "Multiple coupled circuit modeling of induction machines," *IEEE Trans. Ind. Appl.*, vol. 31, no. 2, pp. 311-318, Mar./Apr. 1995.

[18] H.A. Toliyat, S.P. Waikar, and T.A. Lipo, "Analysis and simulation of five-phase synchronous reluctance machines including third harmonic of airgap MMF," *IEEE Trans. Ind. Appl.*, vol. 34, no. 2, pp. 332-339, Mar./Apr. 1998.

[19] W. Wang, K. Nam, and S. Kim, "Concentric winding BLDC motor design," in *Proc. IEEE Int. Conf. IEMDC 2005*, San Antonio, TX, pp. 157-161.

[20] B. Nikbakhtian. S. Talebi, P. Niazi, and H.A. Toliyat, "An analytical model for an N-flux barrier per pole permanent magnet-assisted synchronous reluctance motor," in *Proc. IEEE Int. Conf. IEMDC 2009*, Miami, FL, pp. 129-136.

[21] R. Boyle, C. Greenwood, A. Hohler, M. Liebreich, V.S. O'Brien, et. al., *Global trends in sustainable energy investment 2008: analysis of trends and issues in the financing of renewable energy and energy efficiency*, United Nations Environment Programme and New Energy Finance Ltd., 2008 [Online]. Available: http:// www.unglobalcompact.org/docs/issues_doc/Environment/climate/Global_Trends _2008.pdf, February 11, 2011.

[22] A. McCrone, E. Usher, V.S. O'Brien, A. Hohler, R. Boyle, et. al., *Global trends in sustainable energy investment 2010: analysis of trends and issues in the financing*

of renewable energy and energy efficiency, United Nations Environment Programme and New Energy Finance Ltd., 2010 [Online]. Available: http://bnef.com/Download/UserFiles_File_WhitePapers/sefi_unep_global_trends_2010.pdf, February 11, 2011.

[23] E. Hau, *Wind Turbines: Fundamentals, Technologies, Application, Economics*, Berlin, Germany: Springer, 2006.

[24] R. Harrison , E. Hau, and H. Snel, *Large Wind Turbines: Design and Economics,* Chichester, U.K.: Wiley, 2000.

[25] E. Hau, J. Langenbrinck, *Wega: Large Wind Turbines,* Berlin, Germany: Springer, 1993.

[26] Capital Grant Scheme for Offshore Wind: Kentish Flats Offshore Wind Farm Annual Report January 2006-December 2006 [Online]. Available: http:// www.berr.gov.uk/files/file41600.pdf, August 26, 2008.

[27] Capital Grant Scheme for Offshore Wind: Annual Report January 2005 – December 2005 [Online]. Available: http://www.berr.gov.uk/files/file34791.pdf, August 26, 2008.

[28] Capital Grant Scheme for the North Hoyle Offshore Wind Farm: Annual Report July 2005 – June 2006 [Online]. Available: http://www.berr.gov.uk/files/ file41542.pdf, August 26, 2008.

[29] Capital Grant Scheme for Offshore Wind: Annual Report January 2006 – December 2006 [Online]. Available: http://www.berr.gov.uk/files/file41543.pdf, August 26, 2008.

[30] D. Robb, "Gearbox design for wind turbines improving but still face challenges," *Windstats Newsletter*, vol. 18, no. 3, pp. 6-8, Summer 2005.

[31] D. Robb and L. Harrison, "Who supplies to whom – wind industry gearboxes and bearings," *Windpower Monthly*, p. 56, Nov. 2005.

[32] L. Harrison, "Unacceptable wear found on gears," *Windpower Monthly*, p. 24, Dec. 1998.

[33] D. Robb, "The role of bearings in gearbox failure," *Windpower Monthly*, pp, 53-55, 57-58, Nov. 2005.

[34] G. Bohmeke, R. Boldt, and H. Beneke, "Direct drive, geared drive, intermediate solutions – comparison of design features and operating economics," *European Wind Energy Conference*, Dublin, Ireland, Oct. 1997. pp. 664-667.

[35] S. Siegfriedsen and G. Bohmeke, "Multibrid technology – a significant step to multi-megawatt wind turbines," *Wind Energy*, vol. 1, no. 2, pp. 89-100, 1998.

[36] M. Benatmane, T. McCoy, T. Dalton, and T.L. Cooper, "Electric propulsion full scale development on U.S. Navy surface ships," *Proc. Naval Symposium on Electric Machines*, 1998, pp. 125-134.

[37] P. Mongeau, "High torque density propulsion motors," *Naval Engineers Journal*, vol. 117, no. 4, pp. 53-57, Oct. 2005.

[38] B.W. Eckels and R.M. Calfo, "An evaluation of high torque density electric motor topologies and their application for ship propulsion," *Proc. Naval Symposium on Electric Machines*, 2004.

[39] S. Sodhi, "Electromagnetic gearing applications in hybrid-electric vehicles," M.S. Thesis, Dept. Electrical Eng., Texas A&M University, College Station, TX, 1994.

[40] M. Ehsani, Y. Gao, S.E. Gay, and A. Emadi, *Modern Electric, Hybrid Electric, and Fuel Cell Vehicles*, Boca Raton, FL: CRC Press, 2005.

[41] G.E. Weisenburger, "Electric motor," U.S. Patent 667, 275, Feb. 1900.

[42] S.W. Moore and M. Ehsani, "A charge sustaining parallel HEV application of the transmotor," *SAE International Congress and Exposition*, Detroit, MI, 1999.

[43] Y. Gao and M. Ehsani, "A mild hybrid vehicle drive train with a floating stator motor – configuration, control strategy, design and simulation verification," *SAE Future Car Congress*, Arlington, VA, 2002.

[44] K.T. Chau, D. Zhang, J.Z. Jiang, C. Liu, and Y. Zhang, "Design of a magnetic-geared outer-rotor permanent-magnet brushless motor for electric vehicles," *IEEE Trans. Magn.*, vol. 43, no. 6, pp. 2504-2506, Jun. 2007.

[45] L. Jian, K.T. Chau, and J.Z. Jiang, "An integrated magnetic-geared permanent-magnet in-wheel motor drive for electric vehicles," in *Proc. IEEE Conf. VPPC 2008*, Harbin, China, pp. 1-6.

[46] S. Du, Y. Zhang, and J. Jiang, "Research on a novel combined permanent magnet electrical machine," in *Proc. IEEE Int. Conf. ICEMS 2008*, Wuhan, China, pp. 3564-3567.

[47] P.O. Rasmussen, H.H. Mortensen, T.N. Matzen, T.M. Jahns, and H.A. Toliyat, "Motor integrated permanent magnet gear with a wide torque-speed range," in *Proc. IEEE Energy Convers. Cong. Exp. ECCE 2009*, San Jose, CA, pp. 1510-1518.

[48] Toyota Motor Sales "Toyota Camry Performance and Specs," [Online]. Available: http://www.toyota. com/camry/specs.html, March 15, 2010.

[49] L. Shah, A. Cruden, and B.W. Williams, "A variable speed magnetic gear box using contra-rotating input shafts," *IEEE Trans. Magn.*, vol. 47, no. 2, pp. 431-438, Feb. 2011.

[50] E. Gouda, S. Mezani, L. Baghli, and A. Rezzoug, "Comparative study between mechanical and magnetic planetary gears," *IEEE Trans. Magn.*, vol. 47, no. 2, pp. 439-450, Feb. 2011.

[51] E.P. Furlani, R. Wang, and H. Kusnadi, "A three-dimensional model of computing the torque of radial couplings," *IEEE Trans. Magn.*, vol. 31, no. 5, pp. 2522-2526, Sep. 1995.

[52] Y.D. Yao, D.R. Huang, S.M. Lin, and S.J. Wang, "Theoretical computations of the magnetic coupling between magnetic gears," *IEEE Trans. Magn.*, vol. 32, no. 3, pp. 710-713, May 1996.

[53] E.P. Furlani, "A two-dimensional analysis for the coupling of magnetic gears." *IEEE Trans. Magn.*, vol. 33, no. 3, pp. 2317-2321, May 1997.

[54] F.T. Jorgensen, T.O. Andersen, and P.O. Rasmussen, "Two dimensional model of a permanent magnet spur gear," *Proc. IEEE-IAS 2005*, pp. 261-265.

[55] L. Jian and K.T. Chau, "Analytical calculation of magnetic field distribution in coaxial magnetic gears," *Progress in Electromagnetics Research PIER 92*, pp. 1-16, 2009.

[56] T. Lubin, S. Mezani, and A. Rezzoug, "Exact analytical method for magnetic field computation in the air gap of cylindrical electrical machines considering slotting effects" *IEEE Trans. Magn.*, vol. 46, no. 4, pp. 1092-1099, Apr. 2010.

[57] T. Lubin, S. Mezani, and A. Rezzoug, "Analytical computation of the magnetic field distribution in a magnetic gear," *IEEE Trans. Magn.*, vol. 46, no. 7, pp. 2611-2621, Jul. 2010.

[58] H.A. Toliyat and T.A. Lipo, "Transient analysis of cage induction machines under stator, rotor bar and end ring faults," *IEEE Trans. Energy Convers.*, vol. 10, no. 2, pp. 241-247, Jun. 1995.

[59] J.P. Johnson, A.V. Rajarathnam, H.A. Toliyat, S. Gopalakrishnan, and B. Fahimi, "Torque optimization for a SRM using winding function theory with a gap-dividing surface," *Proc. IEEE-IAS 1996*, pp. 753-760.

[60] T.A. Lipo, *Analysis of Synchronous Machines*, Madison, WI: Wisconsin Power Electronics Research Center, 2008.

[61] H.A. Toliyat, ECEN 611: General Theory of Electromechanical Motion Devices, Class notes, Texas A&M University, College Station, TX, Spring 2005.

[62] N.A. Al-Nuaim and H.A. Toliyat, "A novel method for modeling dynamic air-gap eccentricity in synchronous machines based on modified winding function theory," *IEEE Trans. Energy Convers.*, vol. 13, no. 2, pp. 156-162, Jun. 1998.

[63] J. Faiz, M. Ojaghi, "Unified winding function approach for dynamic simulation of different kinds of eccentricity faults in cage induction machines," *IET Electr. Power Appl.*, vol. 3, no. 5, pp. 461-470, 2009.

[64] F.A. Fouad, T.W. Nehl, and N.A. Demerdash, "Magnetic field modeling of permanent magnet type electronically operated synchronous machines using finite elements," *IEEE Trans. Power App. Sys.*, vol. PAS-100, no. 9, pp. 4125-4135, Sep. 1981.

[65] F.A. Fouad, T.W. Nehl, and N.A. Demerdash, "Permanent magnet modeling for use in vector potential finite element analysis in electrical machinery," *IEEE Trans. Magn.*, vol. MAG-17, no. 6, pp. 3002-3004, Nov. 1981.

[66] R.G. Montague, C.M. Bingham, and K. Atallah, "Magnetic gear dynamics for servo control," in *Proc. IEEE Conf. MELECON 2010,* Valetta, Malta, pp. 1192-1197.

[67] S. Nandi, S. Ahmed, and H.A. Toliyat, "Detection of rotor slot and other eccentricity related harmonics in a three phase induction motor with different rotor cages," *IEEE Trans. Energy Convers.*, vol. 16, no. 3, pp.253-260, Sep. 2001.

[68] R. Krishnan, *Permanent Magnet Synchronous and Brushless DC Motor Drives*, Boca Raton, FL: CRC Press, Ch. 1, 2010.

[69] C.C. Shutt, "Some considerations in the design of damper windings for synchronous motors," *Trans. AIEE*, vol. 51, no. 2, pp. 424-430, Jan. 1932.

[70] J. Matsuki, T. Katagi, and T. Okada, "Damper windings phenomena of synchronous machines during system oscillations," *IEEE Trans. Energy Convers.*, vol. 9, no. 2, pp. 376-382, Jun. 1994.

[71] J. Matsuki, T. Katagi, and T. Okada, "Slot ripples in the damper windings of a salient-pole synchronous generator," *IEEE Trans. Energy Convers.*, vol. 9, no. 1, pp. 126-134, Mar. 1994.

[72] N.A. Demerdash, T.M. Hijazi, and A.A. Arkadan, "Computation of winding inductances of permanent magnet brushless DC motors with damper windings by energy perturbation," *IEEE Trans. Energy Convers.*, vol. 3, no. 3, pp. 705-713, Sep. 1988.

[73] T.M. Hijazi and N.A. Demerdash, "Impact of the addition of a rotor-mounted damper bar cage on the performance of samarium-cobalt permanent magnets brushless DC motor systems," *IEEE Trans. Energy Convers.*, vol. 3, no. 4, pp. 890-898, Dec. 1988.

[74] T.J.E. Miller, M. Popescu, C. Cossar, M. McGilp, G. Strappazzon, N. Trivillin, and R. Santarossa, "Line-start permanent-magnet motor single-phase steady-state

performance analysis," *IEEE Trans. Ind. Appl.*, vol. 40, no. 2, pp. 516-525, Mar./Apr. 2004.

[75] G. Yang, J. Ma, J.X. Shen, and Y. Wang, "Optimal design and experimental verification of a line-start permanent magnet synchronous motor," in *Proc. IEEE Int. Conf. ICEMS 2008*, Wuhan, China, pp. 3232-3236.

[76] P.W. Huang, S.H. Mao, M.C. Tsai, and C.T. Liu, "Investigation of line start permanent magnet synchronous motors with interior-magnet rotors and surface-magnet rotors," in *Proc. IEEE Int. Conf. ICEMS 2008*, Wuhan, China, pp. 2888-2893.

[77] B.L. Ahn, W.H. Kim, B.S. Kim, K.C. Ko, and J. Lee, "A study on the optimal barrier design for high efficiency of LSPM," in *Proc. IEEE Int. Conf. ICEMS 2008*, Wuhan, China, pp. 3427-3429.

[78] J. Kinnunen, J. Pyrhonen, O.Liukkonen, and P. Kurronen, "Analysis of directly network connected non-salient pole permanent magnet synchronous machines," in *Proc. IEEE Int. Symp. Ind. Electr.*, Montreal, Canada, 2006, pp. 2217-2222.

[79] K. Kamiev, J. Nerg, and J. Pyrhonen, "Design of damper windings for direct-on-line permanent magnet synchronous generators," in *Proc. IEEE Eurocon 2009*, Saint Petersburg, Russia, pp. 783-790.

[80] N.W. Frank and H.A. Toliyat, "Analysis of the concentric planetary magnetic gear with strengthened stator and interior permanent magnet (IPM) inner rotor," in *Proc. IEEE Energy Convers. Cong. Exp. ECCE 2010*, Atlanta, GA, pp. 2977-2984.

[81] G.F. Franklin, J.D. Powell, and A. Emami-Naeini, *Feedback Control of Dynamic Systems*, Upper Saddle River, NJ: Prentice Hall, 2002.

[82] C.G. Armstrong, "Power transmitting device," U.S. Patent 687,292, Nov. 26, 1901.

[83] A.H. Neuland, "Apparatus for transmitting power," U.S. Patent 1,171,351, Feb. 8, 1916.

[84] H.T. Faus, "Magnetic transmission," U.S. Patent 2,371,511, March 13, 1945.

[85] G.A. Reese, "Magnetic gearing arrangement," U.S. Patent 3,301,091, Jan. 31, 1967.

[86] T.B. Martin Jr., “Magnetic transmission,” U.S. Patent 3,378,710, April 16, 1968.

[87] H.P. Schlaeppi, “Magnetic gears,” U.S. Patent 3,382,386, May 7, 1968.

[88] N. Laing, “Centrifugal pump with magnetic drive,” U.S. Patent 3,762,839, Oct. 2, 1973.

[89] M. Hetzel, “Low friction miniature gear drive for transmitting small forces, and method of making same,” U.S. Patent 3,792,578, Feb. 19, 1974.

[90] W.J. Mabe Jr., “Magnetic transmission,” U.S. Patent 5,013,949, May 7, 1991.

[91] J.E. Rode, “Magnetic gear and gear train configuration,” U.S. Patent 5,569,967, Oct. 29, 1996.

[92] B. Ackermann and L. Honds, “Magnetic drive arrangement comprising a plurality of magnetically cooperating parts which are movable relative to one another,” U.S. Patent 5,633,555, May 27, 1997.

[93] B. Ackermann, “Magnetic drive arrangement,” U.S. Patent 5,994, 809, Nov. 30, 1999.

[94] E.W. Nissen, “Magnetic transmission,” U.S. Patent 7,105,968, Sep. 12, 2006.

[95] R.J. Wise, “Torque converter system and method of using the same,” U.S. Patent 7,145,276, Dec. 5, 2006.

[96] A.G. Razzell, and J.A. Cullen, “Compact electrical machine,” U.S. Patent 6,794,781

[97] W.J. McDonald, T.F. Price, and G.P. Hatch, “Wellbore motor having magnetic gear drive,” U.S. Patent 7,481,283, Jan. 27, 2009.

[98] W.J. McDonald, T.F. Price, and G.P. Hatch, “Wellbore motor having magnetic gear drive,” U.S. Patent 7,549,467, Jun. 23, 2009.

APPENDIX A

PATENTS RELATED TO MAGNETIC GEARING

A couple of patents precede Harold Faus' early patent on magnetic spur gears. They were the first patents to employ gearing arrangements with electromagnetic means. The first one, from 1901, is a spur gear arrangement with coils instead of permanent magnets [82]. A patent followed 15 years later, employing electromagnetic means for a planetary gearing arrangement very similar to the magnetic gear studied for this dissertation [83]. The first patent related to a device which employed magnetic gearing with only permanent magnets is found in [1]. Faus filed another patent shortly thereafter, for a magnetic transmission capable of changing the gear ratio by means of a spiral gear arrangement [84]. The next patent did not come until the latter half of the 1960's. This patent described a magnetic planetary gear in which only one of the rotors employed permanent magnets [85]. Two patents followed the next year relating to magnetic planetary gearing arrangements [86][87]. In [88], a pump was assisted by means of a planetary gearing arrangement similar to the gear studied in this dissertation. In [89], the magnetic spur gear was once again patented. The magnetic dual to the mechanical planetary gear was patented in 1991 [90]. The magnetic spur gear was once again patented in 1996 [91].

The patent most directly related to the gear in this study was patented in 1997 [92]. The primary drawback to this arrangement was the geometry of the stator flux modulator. The continuous nature allows for extensive flux leakage. An improvement to

the design followed later in [93], placing the stator flux modulator outside of the magnetic rings. In [94], another magnetic transmission was patented, employing a variable gear ratio by means of multiple spur gears. Yet another magnetic spur gear arrangement followed shortly thereafter in [95].

In [96], the concentric planetary magnetic gear with an integrated motor was patented and assigned to Rolls Royce. Two identical patents assigned to Dexter Magnetic Technologies are the most recent patents at this time, relating to a magnetic gear for wellbore drilling [97][98].

VITA

Nicolas Walter Frank received his B.S. degree (*magna cum laude*) in electrical engineering from Texas A&M University in 2004, where he specialized in power electronics. He also received his Ph.D. degree from Texas A&M University in 2011, where he specialized in power electronics and electric machine design. In 2004 he received a diversity fellowship from Texas A&M University to begin his graduate studies.

During his time as a graduate student, he completed internships for the Air Force Research Labs in Albuquerque, NM, United Technologies Research Center in East Hartford, CT, Schlumberger in Sugar Land, TX, and was a guest researcher at the Institute of Energy Technology at Aalborg University in Aalborg, Denmark. His time in Denmark was funded in part by a grant from the American Scandinavian Foundation. He is currently employed as an engineer at the ABB US Corporate Research Center in Raleigh, NC. He can be reached through:

Attn.: Nicolas Frank

Texas A&M University ECE Dept.

214 Zachry Engineering Center

TAMU 3128

College Station, TX 77843-3128